A high-magnification scanning electron micrograph (SEM) of a porous carbon material. The image shows a complex, interconnected network of fine, needle-like or fibrous structures, creating a highly textured and porous surface. The material appears as a bright, granular mass against a dark background. The texture is highly irregular, with many small voids and protrusions, characteristic of activated carbon or similar porous materials.

Calorimetry of Capacitive Porous Carbon Electrodes in Aqueous Media

J. E. VOS

Calorimetry of Capacitive Porous Carbon Electrodes in Aqueous Media

J.E. Vos

Doctoral Thesis

Calorimetry of Capacitive Porous Carbon Electrodes in Aqueous Media

Printed by proefschriftmaken.nl

Cover design by Ron Zijlmans

Calorimetry of Capacitive Porous Carbon Electrodes in Aqueous Media

Calorimetrie van Capacitieve Poreuze Koolstofelektroden In Waterige Oplossingen

(met een samenvatting in het Nederlands)

Proefschrift

ter verkrijging van de graad van doctor aan de Universiteit Utrecht op gezag
van de rector magnificus, prof. dr. H.R.B.M. Kummeling, ingevolge het
besluit van het college voor promoties in het openbaar te verdedigen op
maandag 3 april 2023 des middags te 4.15 uur

door

Joren Ezra Vos

geboren op 18 maart 1992 te Nijmegen

Promotor: Prof. dr. A. P. Philipse

Copromotor: Dr. B. H. Ern 

Beoordelingscommissie:

Prof. dr. ir. H. V. M. Hamelers

Prof. dr. W. K. Kegel

Prof. dr. R. H. H. G. van Roij

Prof. dr. D. A. M. Vanmaekelbergh

Dr. P. Ngene

This work is part of the project ‘Experimental Thermodynamics of Ion Confinement in Porous Electrodes’ with project number 712.018.001 of the Dutch Research Council (NWO).

Contents

1	General Introduction	7
1.1	Porous carbon electrode applications	8
1.2	Electrical double layers in porous electrodes	8
1.3	Experimental thermodynamics of the EDL	10
1.4	Electrochemical calorimetry setup	11
1.5	This Thesis	13
2	Three-Electrode Cell Calorimeter for Electrical Double Layer Capacitors	15
2.1	Introduction	16
2.2	Design and Operation	17
2.3	Test Measurements	22
2.4	Conclusion	27
2.5	Appendix 1: Alternative setup with lock-in detection of RTDs using a Wheatstone bridge	29
3	Electric Potential of Ions in Electrode Micropores Deduced from Calorimetry	33
3.1	Introduction	34
3.2	Experimental	35
3.3	Theory	36
3.4	Results	39
3.5	Discussion	41
3.6	Conclusion	45
3.7	Appendix 1: Purity and Provenance of the Chemicals	46
3.8	Appendix 2: Temperature-dependent measurements	46
3.9	Appendix 3: Nitrogen physisorption measurements and analysis	48
3.10	Appendix 4: Additional HFS Results	49

4 Capacitive Charging Rate Dependence of Heat from Porous Carbon in Aqueous Salt Solution	55
4.1 Introduction	56
4.2 Experimental	58
4.3 Theory	59
4.4 Results and discussion	63
4.5 Conclusions	72
4.6 Appendix 1: Formulas for period 1 (charging, $0 \leq t \leq \tau$)	73
4.7 Appendix 2: Formulas for period 2 (charging, $t \geq \tau$)	76
4.8 Appendix 3: Formulas for period 3 (discharging, $0 \leq t \leq \tau$) . .	79
4.9 Appendix 4: Formulas for period 4 (discharging, $t \geq \tau$)	82
4.10 Appendix 5: Additional figures for abrupt polarization, $\tau = 100$ s, and $\tau = 1000$ s at different potentials	85
5 Cathodic versus Anodic Charging Dynamics of Capacitive Porous Carbon Electrodes in Aqueous Salt Solutions	95
5.1 Introduction	96
5.2 Experimental	98
5.3 Data analysis	99
5.4 Results and Discussion	104
5.5 Conclusion	114
5.6 Appendix 1: Figures with current transients during charging and discharging	115
6 Summary / Samenvatting	117
6.1 Summary	118
6.2 Samenvatting	120
Bibliography	123
List of Publications	138
Acknowledgements	139
About the Author	141

Chapter 1

General Introduction

Abstract

Shortage of drinking water is a problem that affects billions of people worldwide. One of the possible remedies is to produce fresh water from brackish water via capacitive deionization, using porous carbon electrodes to adsorb the ions of the salt. Such electrodes have a high surface area, which allows for high ion uptake in the so-called Electrical Double Layer (EDL). Much of the information about this EDL comes from electrical measurements, which indicate how rapidly how much charge is accumulated in the system at a chosen electric potential of the electrode. In 2017, Janssen et al. [1] argued that the heat released during (dis)charging of the EDL also contains valuable information about the EDL, which can serve as an additional test of existing theoretical descriptions. In this thesis, we aim to build on the work by Janssen et al.[1] by measuring the heat with greater precision, and as a function of the electrode potential, with different types of ions, looking for new insight into the physical origin of the measured heat. This Chapter gives a simplified introduction to porous carbon electrodes, their EDL, the thermodynamics, and our experimental approach to electrochemical calorimetry.

1.1 Porous carbon electrode applications

Activated porous carbon is a conductive, relatively inert material with pore widths on different length scales and a specific surface area that typically exceeds $1000 \text{ m}^2/\text{g}$ [2], which is mostly made up of micropores ($<2 \text{ nm}$ in width). Consequently, electrodes from such material allow for high ion uptake.

One application of such electrodes is supercapacitors [3]. They are able to deliver high electric power on a short time scale [4]. Compared to Li-Ion batteries, they have longer cycle lives, but lower energy density and a smaller voltage window [5, 6]. Supercapacitors are used in the automotive [7], military, satellite, communications, and space industries [8].

Another application of porous carbon electrodes is capacitive deionization [9, 10, 11]. About four billion people in the world are effected by shortage of drinking water [12]. In capacitive deionization, the electrodes are used to extract ions out of brackish water, essentially desalting the water, creating drinking water. The uptake of ions is alternated with their release into a waste stream, to allow new uptake of ions.

1.2 Electrical double layers in porous electrodes

When electronic charge is added to a solid conductor (electrode) in an electrolyte solution, oppositely charged ions (counterions) are attracted toward the surface and ions of the same sign (co-ions) are repelled. Most of the net ionic charge consists of counterions adsorbed at the surface, in the ‘Stern layer’, but some of the net ionic charge is also present in the solution near the surface, in a diffuse ‘Gouy-Chapman layer’ [13]. Together, the layer of electronic charge at the solid surface and the layer(s) of opposite ionic charge constitute the ‘electrical double layer’ (EDL), which as a whole is electroneutral. Fig. 1.1 sketches the situation.

When the EDL is at the surface of pores that are a nanometer in width, the diffuse parts of the EDLs from opposite pore walls strongly overlap. This is the case especially at low electrolyte concentrations, since the Debye screening length of the EDL is then larger than the distance between the pore walls [10]. The situation of the EDL in porous confinement is shown in Fig. 1.2. The ionic solution inside the pores is at approximately constant potential,

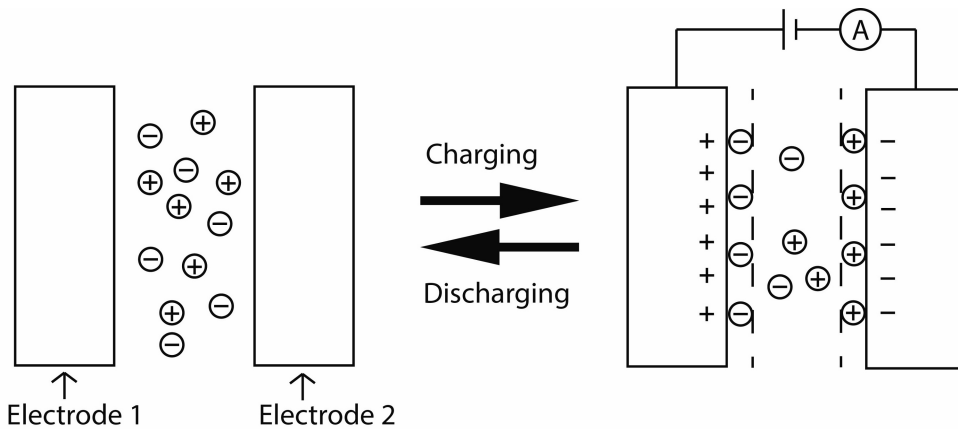


Figure 1.1: Schematic illustration of formation of an Electrical Double Layer at flat electrodes. Without an applied voltage, ions are randomly distributed between both electrodes. When a voltage is applied, counterions move toward the charged surface, forming a Stern layer, and also a diffuse layer of ionic solution near the surface carries a net charge.

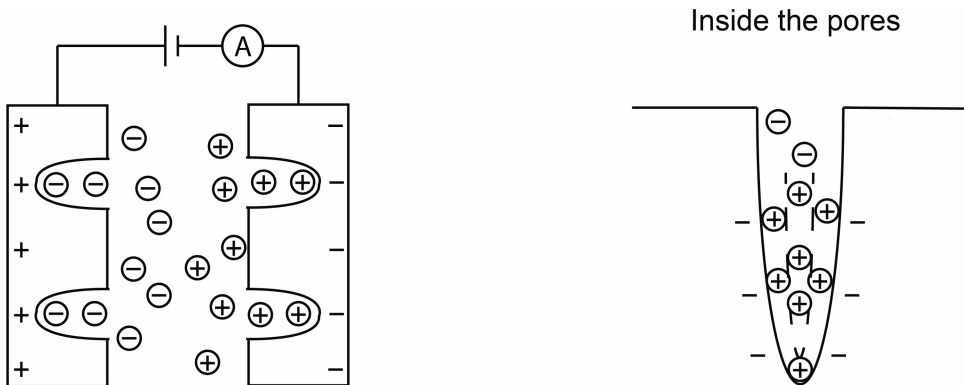


Figure 1.2: Schematic illustration of electrical double layer formation in porous carbon. Inside a micropore, the electric potential experienced by the ions depends on the presence of both nearby walls. This situation corresponds to the overlap of the EDLs of the two pore walls.

allowing the usage of the modified Donnan (mD) model [14, 15] to estimate the concentrations of ions inside the pores.

Another factor of importance is the width of the pores compared to the ion size. Microporous carbon consists of graphene-like sheets, with an average distance of about 1 nm between the sheets, corresponding to slit-like pores [16]. Water molecules adsorbed at the pore walls further limit the space of pores available for ions [17, 18]. Ions can lose their solvation shells, decreasing their effective radius and thus allowing them to enter pores that are smaller than the size of hydrated ions [19, 20, 21, 22].

Much of the information that we have about the EDL in porous electrodes has been acquired from electrical data, such as the time-dependent current flowing at different potentials. It has however been shown that the heat that is released during (dis)charging of porous carbon electrodes gives independent information about in the EDL.

1.3 Experimental thermodynamics of the EDL

The heat of the forming of the EDL in porous electrodes has been measured via calorimetry [1, 23, 24, 25, 26, 27, 28, 29]. The amount of heat that is released is little and spread out over time due to the slow ionic uptake in the pores [11, 30], requiring sensitive measuring methods. Earlier measurements were done using resistance temperature detectors [1, 28] or heat flux sensors [29].

The measured heat consists of two parts: the irreversible and reversible heats. The irreversible heat is the heat that is generated in the ohmic parts of the system, and it is also called the ‘Joule heat’. The reversible heat is the heat that corresponds to the heat of formation of the EDL and is by definition equal in magnitude but opposite in sign during charging and discharging. When it is assumed that the irreversible heat is equal during charging and discharging, the difference in heats between charging and discharging is twice the reversible heat of the system. In this thesis, the validity of this assumption is evaluated by slowing down the charging. Since the rate at which the irreversible heat is produced scales quadratically with the magnitude of the current, the irreversible heat is diminished upon slower charging, which practically leaves only

the reversible heat when charging is sufficiently slow.

Different explanations for the origin of the reversible heat have been given, such as an entropy change due to ion confinement in the pores [28], changes in the entropic part of the grand potential [31, 32], and changes in the entropy and enthalpy due to mixing and electrical and steric interactions of the ions [33, 34, 27]. Our own approach is to consider that the measured heat is the difference between the energy change of the system, for which we propose a new formula, and the electrical work performed on the system, which can be calculated from the time-dependent current and applied potential. The reversible heat is then effectively the difference between the energy change of the EDL, given by our formula, and the electrical work on the system if it would be performed reversibly. Our physical interpretation for the reversible heat is the change in potential energy of the ions as they enter or leave the pores. This change in potential energy is probably dominated by the adsorption energy of the ions to the carbon surface and the electrical energy of the ions at the nonzero electric potential inside the pores.

1.4 Electrochemical calorimetry setup

Earlier calorimetric measurements on porous carbon electrodes were done using a two-electrode electrochemical cell, measuring the heat of the complete cell [1, 28] or the heat of both electrodes separately [29]. In a two-electrode cell, a voltage is applied between the two electrodes and the resulting current is measured. A two-electrode cell does not allow one to distinguish between anodic and cathodic (dis)charging of an electrode, and measuring the heat from a complete cell does not allow one to distinguish between anodic and cathodic heat production either. To circumvent this limitation, all the measurements described in this thesis are performed using a three-electrode cell, which includes a reference electrode. The electrode whose electrical and thermal characteristics are studied is called the working electrode (WE). The potential of the WE is applied with respect to the reference electrode (RE), allowing precise control of the potential of the WE. The resulting current is measured between the WE and a counter electrode (CE). A schematic overview of a both types of cells is shown in Fig. 1.3. In our electrochemical calorimetry

cell, a heat flux sensor (HFS) is placed against the WE, to measure its heat production. This makes it possible to compare the effects of adsorbing positive counterions (cations) at negative potentials of the WE (cathodic range) and the effects of adsorbing negative counterions (anions) at positive potentials (anodic range).

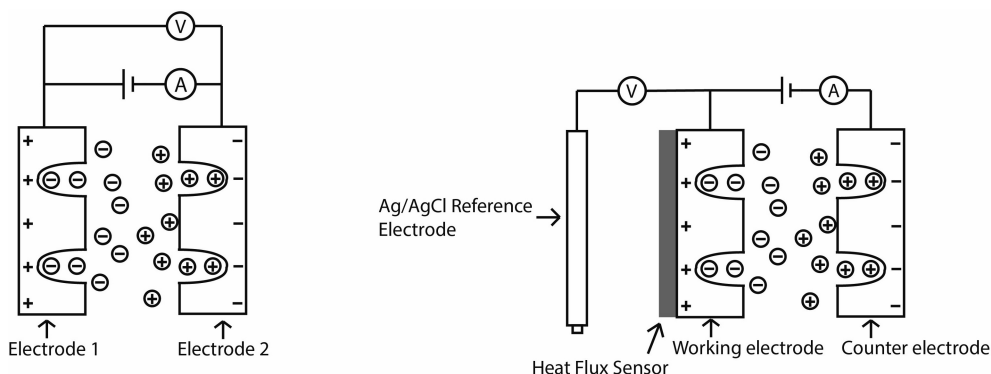


Figure 1.3: On the left, a schematic overview of a two-electrode cell. On the right, a schematic illustration of a three-electrode cell, with a WE, CE, and RE. The HFS is placed behind the WE, to measure the heat of only this electrode.

1.5 This Thesis

In Chapter 2, the electrochemical calorimetry setup is described in detail. Also shown is the method of calibration, used to calculate the entire heat produced by the working electrode from the signal of the heat flux sensor.

Chapter 3 gives our explanation for the origin of the reversible heat: a nonzero potential energy of the ions in the pores. In this way, experimental results are analyzed for different aqueous salt solutions.

Chapter 4 demonstrates that the model presented in Chapter 3 can also account for the heat generation in the EDL at different charging rates. For measurements far from equilibrium, the found reversible heat is the same as when the electrode is charged slowly. Agreement between experiment and theory is not quantitative, which we attribute to the time-dependence of the current, which is not simply mono-exponential at constant applied potential.

In Chapter 5, the time-dependence of the current is examined more closely, measured in different aqueous salt solutions and at different applied potentials in the cathodic and anodic ranges. The results are analyzed in detail, to examine whether the diffusion of the counterions becomes rate-limiting once the charging process is nearly complete.

The research presented in this thesis and the main conclusions are summarized in Chapter 6.

Chapter 2

Three-Electrode Cell Calorimeter for Electrical Double Layer Capacitors

Abstract

A calorimeter was built to measure the heat from a porous capacitive working electrode connected in a three-electrode configuration. This makes it possible to detect differences between cathodic and anodic heat production. The electrochemical cell contains a large electrolyte solution reservoir, ensuring a constant concentration of the salt solution probed by the reference electrode via a Luggin tube. A heat flux sensor is used to detect the heat, and its calibration as a gauge of the total amount of heat produced by the electrode is done on the basis of the net electrical work performed on the working electrode during a full charging-discharging cycle. In principle, from the measured heat and the electrical work, the change in internal energy of the working electrode can be determined as a function of applied potential. Such measurements inform about the potential energy and average electric potential of ions inside the pores, giving insight into the electrical double layer inside electrode micropores. Example measurements of the heat are shown for porous carbon electrodes in aqueous salt solution.

2.1 Introduction

Capacitive porous electrodes are of interest for instance as supercapacitors in power delivery systems [35] and as reversible salt absorbants in water desalination [9]. During charging of a porous electrode, electrical energy and ions are stored in the electrical double layer (EDL). Experimental characterization of the EDL helps to elucidate the energetic or ionic uptake capacity of the electrode. Changes in the amount of charge can be measured in the external electrical circuit [10, 36]. Additional information on the charging mechanism and the amounts of ions inside the pores can for instance be obtained from in situ NMR spectroscopy [37, 38, 39, 40], infrared spectroscopy [41, 42], and small-angle neutron scattering [43, 44]. Here, we will focus on a thermodynamic characterization approach that consists of measuring the heat exchanged while the electrode is being charged or discharged.

Electrodes in any electrochemical cell produce heat, although this is generally not the intended outcome. One example is heat generation during electrolysis reactions [45]. Another is Joule heat produced by supercapacitors [24], which can cause a strong temperature rise that can be damaging for their performance [46, 47, 48]. When it is possible to determine the reversible heat, this provides valuable information on the change in thermodynamic state of the system. The reversible heat can for example correspond to the enthalpy changes due to the electrochemical processes [49, 50] or to the entropic heat from batteries, in agreement with the temperature dependence of their open circuit voltage [51]. For supercapacitors, the reversible heat has been interpreted in different ways, as the entropic heat from the confinement of ions into the pores of the electrodes [28], or as changes in the entropic part of the grand potential energy [31, 32], or as due to several entropic and enthalpic contributions because of mixing as well as electrical and steric interactions of the ions [27, 33, 34], or as due to nonzero potential energy of the ions in the pore; see Chapter 3.

Measuring heat from porous electrodes requires a different measurement approach than measuring heat from submonolayer changes at a flat electrode [23], which result in very little heat, produced very briefly [52]. The latter requires highly sensitive and rapid detection, which can for instance be achieved using lithium tantalate-based sensors [53]. Porous electrodes have a much

higher surface area and slow ionic transport in an extensive porous network [11, 30]. resulting in much more heat production but spread out over a much longer time. Due to the long duration of heat production, the measurement requires a very stable background temperature to differentiate from heat exchange due to temperature changes in the environment.

Here, a setup is presented that measures the heat of charging and discharging from a capacitive porous carbon [54] electrode, connected in a 3-electrode configuration. Earlier experiments on capacitive porous electrodes were done on 2-electrode cells, by measuring the temperature of the complete cell using a resistance temperature detector [1, 28], or by measuring the separate heats of both electrodes, using heat flux sensors [29, 34]. When the heat of a complete cell is measured, differences between cathodic and anodic heat production cannot be distinguished. This limitation disappears when the heat of individual electrodes is measured. However, when the cell has only two electrodes, even though it is clear that the charge that exits one electrode enters the other electrode, it is more difficult to clarify differences between cathodic and anodic behavior, because the potentials applied to each electrode are not determined against a constant reference. In the setup presented here, a reference electrode is introduced as the third electrode. The current still flows from the working electrode to a counter electrode, but the potential on the working electrode is applied and measured with respect to an invariant reference electrode. A three-electrode cell is commonly used in electrochemistry [55], but not for measurements on commercial batteries or supercapacitors. In Section 2.2, the design and operation of the setup are presented, and typical measurements are shown in Section 2.3.

2.2 Design and Operation

2.2.1 Electrochemical setup

The electrochemical cell developed to measure heat effects of capacitive porous electrodes in a 3-electrode configuration is shown in Fig. 2.1. The cell has three glass parts. The central part consists of a horizontal cylinder (6.4 cm in length, 2.5 cm in external diameter) whose extremities are glued into the central hole (2.5 cm diameter) of square blocks (5 cm by 5 cm, 5 mm thick).

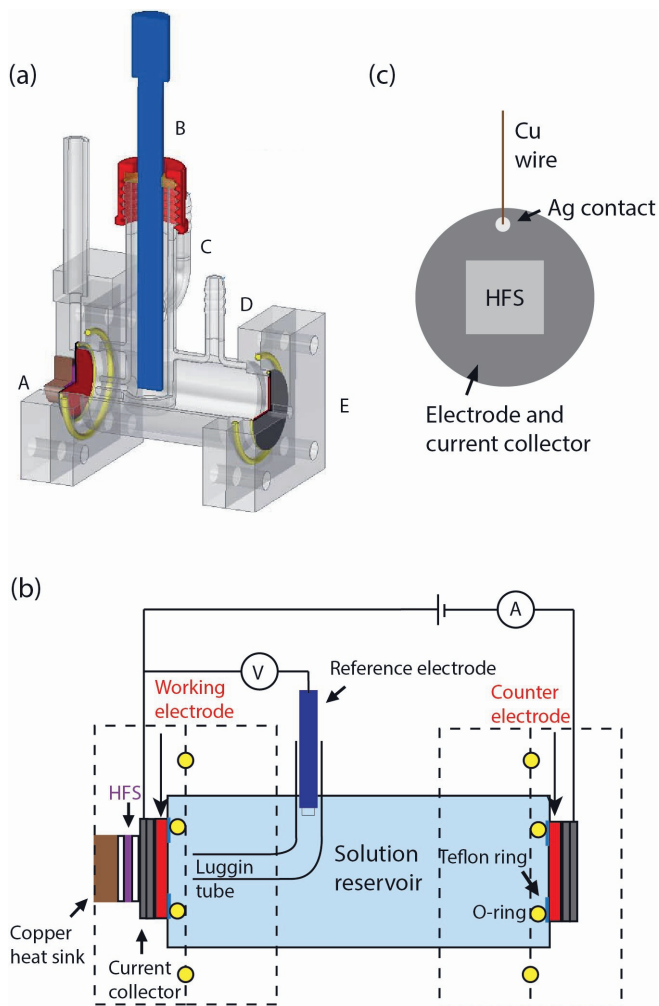


Figure 2.1: (a) Technical drawing of the electrochemical cell used for heat measurements on a porous electrode, connected in a 3-electrode configuration; A = outer square part containing the working electrode, with the HFS in purple behind it; the HFS is thermally stabilized by a copper block at the back; B = reference electrode; C & D = electrolyte solution in- and outlets; E = outer square part containing the counter electrode. (b) Schematic overview of the cell and its connections to the potentiostat. The yellow circles are cross-sections of the O-rings seen in part (a) of the figure. (c) Position of the HFS with respect to the electrode, the current collector, and the ohmic contact.

These glued square blocks of the central part are connected to two outer square parts of the cell via plastic screws inserted into four holes at the corners of the squares, see Fig. 2.1(a). One of the outer square parts contains the counter electrode (CE), and the other contains the working electrode (WE) and the heat flux sensor (HFS). The WE and CE are mounted vertically, allowing gas to escape from the electrode surface. The separation of 6.4 cm between the electrodes ensures that no measurable heat of the CE reaches the heat flux sensor mounted behind the WE (given the thermal diffusivity of water [56], the timescale for heat diffusion across 6.4 cm of water is more than an hour). The volume of the cylinder (30 mL) is sufficiently large that the salt concentration remains approximately constant. The reference electrode (RE) senses the potential of the solution near the WE via a Luggin tube. Typically, a Radiometer Analytical REF201 Red Rod Ag/AgCl/saturated KCl is used as RE.

The WE and the CE each consist of a disk of porous carbon with a diameter of 22 mm and a thickness of typically 0.4 mm. Compared to a Pt CE, a porous carbon CE has the advantage that it does not produce hydrogen or oxygen gas under our measurement conditions, gases which can be oxidized or reduced at the WE, leading to faradaic currents which complicate the interpretation. At the center, these electrodes are glued to a nonporous carbon disk of 25 mm in diameter using a minimal amount of nonconductive Bison Kombi Snel epoxy glue. Mechanical contact between the WE and the current collector (a nonporous carbon disk of the same dimensions) is realized by pushing them together at their outer rims with a flat 50 μm thick Teflon ring itself pushed by a 2 mm thick rubber O-ring with a diameter of 21 mm. The central part of the electrode exposed to the solution has a diameter of 18.5 mm. An electrically insulated copper wire is glued to the back side of the current collector using silver epoxy glue (Chemtronics[®] CW2400 conductive epoxy), ensuring electrical contact. This is topped off with nonconductive epoxy glue to insulate electrically the outer portion of the silver epoxy glue. The HFS (greenTEG gSKIN[®] XP 26 9C, earlier used to measure heat from supercapacitor electrodes by Munteshari et al. [29]), is placed behind the WE in a separate glass compartment with walls of 0.15 mm in thickness. This compartment is an additional protection of the sensor (which must remain dry)

against salt solution leaking around the outer rim of the current collector. The $1\text{ cm} \times 1\text{ cm}$ surface of the HFS faces the electrode and current collector and is centered with respect to them. In contrast, the ohmic contact between current collector and copper wire is more to the side, see Fig. 2.1(c).

The HFS voltage is sampled twice per second using a Keithley 2182A Nanovoltmeter, connected to a personal computer via a GPIB interface. The electric potential difference is applied between the WE and the CE using a channel of an AMETEK PARSTAT MC-1000 multichannel potentiostat, with a feedback loop to keep the electrical potential of the WE stable with respect to the RE. The same instrument measures the resulting current between the WE and the CE.

2.2.2 Temperature stabilization

The electrochemical cell is in a controlled thermostatic environment to ensure a stable background level of the heat flux signal. The HFS is in thermal contact with a copper heat sink of 5.5 mm in thickness and 15.3 mm in diameter, in contact with water that surrounds the electrochemical cell. The cell is submerged in a 2 L glass beaker, filled with tap water up to the breathing hole of the reference electrode. This beaker is positioned at the center of a copper cylinder (34 cm height by 24 cm width), itself at the center of a thermostated box of 50 cm by 50 cm by 45 cm in height. Copper tubing is welded to the copper cylinder for good heat contact, and connected to a Julabo F25-HE Refrigerated/heating circulator bath via polyvinyl chloride (PVC) tubes, pumping thermostated water through the copper cylinder. The box is closed with a lid measuring 50 cm in length and width and 24 cm in thickness and consisting of wood and styrofoam. The large heat capacity of the water in the glass beaker and an air gap of 5 cm between the beaker and the copper walls dampen temperature fluctuations of the thermostatic bath. To verify temperature stability and independence from environmental artifacts, the temperatures of the water in the glass beaker, of the water in the thermostatic bath, and of the air in the room are monitored using Pt100 sensors, whose signals are acquired via a Pico[®] Technology PT-104 Platinum Resistance Data Logger. The water bath has a temperature range of 5 °C to 70 °C. Due to the large heat capacity, it takes up to 48 hours before the thermostatic box reaches a stable temperature

after closing the lid. Typically, the temperature of water in the glass beaker is constant within a standard deviation of 0.0045°C on a short time scale (10^2 s) and 0.0058°C on a long time scale (10^5 s).

2.2.3 Operation and Calibration

The standard measurement protocol was as follows. The temperature is stabilized and the difference between the potential of the WE and that of the RE at open circuit—the open circuit potential (V_{OCP})—is measured for several hours, until this potential has also stabilized, at around 0.2 V vs. RE in the case of the studied carbon electrodes in aqueous NaCl solution. A cyclic voltammogram is measured to verify that the electrical behavior of the WE is largely capacitive, without oxidative or reductive peaks indicating faradaic processes. Then, the same potential as was measured at equilibrium at open circuit, $V_{\text{OCP}} = 0.2\text{ V}$ vs. RE, is applied actively to the WE for ≥ 1 hour until the current becomes minimal ($< 20\text{ }\mu\text{A}$). The applied potential is then changed by ΔV , resulting in peaks of electrical current and HFS voltage, V_{HFS} . After 1 to 2 hours, 0.2 V vs. RE is reapplied. The charging-discharging cycle is repeated for ΔV from $+0.5\text{ V}$ to $+0.1\text{ V}$ and from -0.5 V to -0.1 V , and this potential series is repeated at least once.

In principle, calibration can be done based on the specifications of the HFS ($12.7\text{ }\mu\text{V}$ per heat flux in W/m^2 for the sensor used here). In that case, it must be known which fraction of the heat produced by the electrode is measured by the HFS. This can be calculated by assuming that half of the electrode heat is produced in the direction of the HFS and by taking into account the different surface areas of the electrode and the HFS. However, differences in the distance between electrode and HFS in early prototypes of the cell, as well as differences in heat contact from one electrode to the other, can render the calibration unreliable by a factor of order 2. Therefore, we chose to calibrate on another basis: the Joule heat of a complete charging-discharging cycle; see Chapter 3.

When a known potential ΔV is applied vs. V_{OCP} , a charge ΔQ builds up in the electrode during charging. As explained in Chapter 3, for a full cycle of charging and discharging, the total reversible heat is zero and the net measured heat is the irreversible heat, equal to the net electrical work

performed on the electrode during the cycle:

$$q_{\text{ch}} + q_{\text{dis}} = -\Delta Q \Delta V, \quad (2.1)$$

where q_{ch} is the heat during charging and q_{dis} the heat during discharging. This equation stems from the knowledge that the internal energy of the electrode is the same before and after a full cycle of charging and discharging, since the electrode comes back to its initial state. The total integrated surface area of the two HFS voltage peaks in a charging-discharging cycle is proportional to $-\Delta Q \Delta V$ and the ratio of the two gives the calibration constant K , the total amount of heat produced by the electrode per integrated HFS signal:

$$-\Delta Q \Delta V = K \int V_{\text{HFS}} dt \quad (2.2)$$

Separate heats of charging and discharging in energy units can now be calculated from integrated HFS signals in units of Vs, using the calibration constant in units of J/(Vs). This assumes that the HFS has the same sensitivity for the reversible heat and for the Joule heat, an assumption which will be discussed in Section 2.3.2.

2.3 Test Measurements

2.3.1 Experimental Results

Test measurements were done on porous carbon electrodes cut from sheets of electrode material produced by Voltea B.V. (Amstelveen, The Netherlands). The material had a density of 0.58 g mL^{-1} , a porosity of 65%, and a Brunauer-Emmett-Teller surface area of 88 m^2 per electrode; see Chapter 3. This material was comparable to that prepared in Ref. [36], with activated carbon (YP-50F, Kuraray, Japan), carbon black (Vulcan XC72R, Cabot Corp., Boston, MA) and a binder (85:5:10 in weight ratio). The electrolyte solution consisted of 1 M NaCl (for molecular biology, $\geq 98\%$, Sigma), degassed using a Branson 8800 Series Ultrasonic Cleaner.

In Fig. 2.2, results of a typical measurement series are shown. Within minutes of changing the potential applied to the working electrode, current and heat flux were close to zero, but to ensure that equilibrium was attained

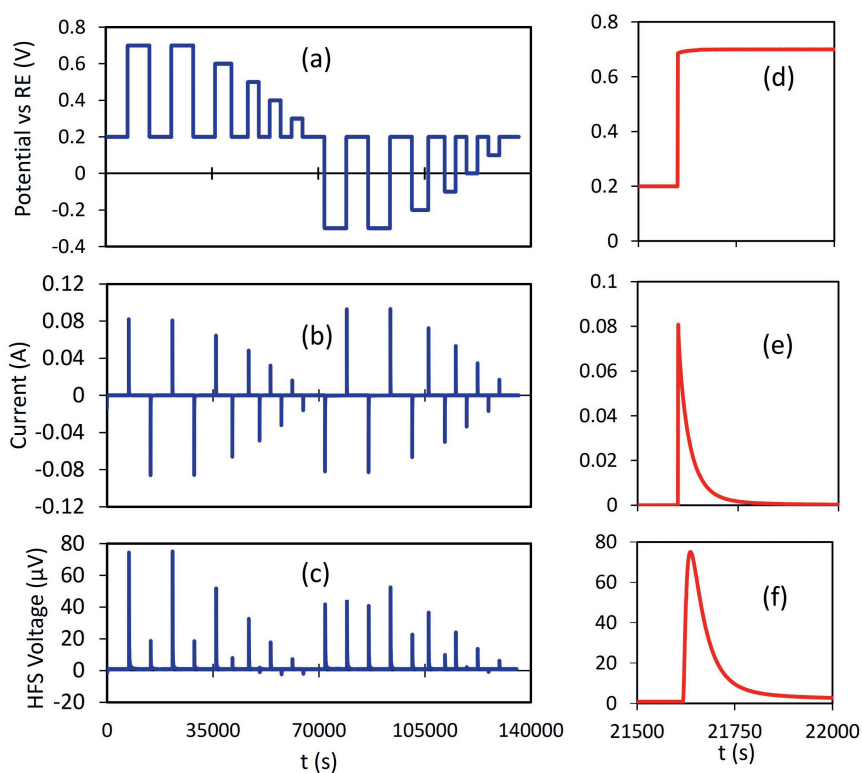


Figure 2.2: Typical measurements on a porous carbon electrode in 1 M aqueous NaCl with (a) the measured applied potential, (b) the resulting current, and (c) the HFS voltage. (d)-(f) Shape of the signals in (a)-(c), respectively, during charging from 0.2 V to 0.7 V (potentials versus RE; 0.2 V is the open circuit potential).

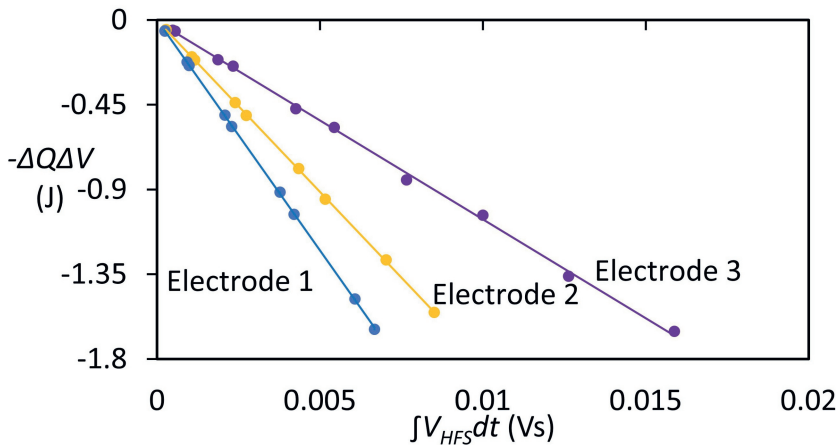


Figure 2.3: Typical calibration results for 1 M NaCl using different electrodes, with $K_1 = (-245.2 \pm 0.8) \text{ J V}^{-1} \text{ s}^{-1}$, $K_2 = (-182.1 \pm 0.6) \text{ J V}^{-1} \text{ s}^{-1}$, and $K_3 = (-104.9 \pm 1.3) \text{ J V}^{-1} \text{ s}^{-1}$, the calibration constants for electrodes 1, 2, and 3, respectively.

and to have a reliable baseline, measurements were continued for at least one hour after each change of applied potential. The signal-to-noise ratio of the highest HFS voltage peak ($75 \mu\text{V}$) was 2850:1 in Fig. 2.2. In general, the signal-to-noise ratio was about two orders of magnitude higher than in the 2-electrode thermometer setup of Ref. [1].

Figure 2.3 shows the effect of different electrodes on the calibration according to Eq. 2.2. The main difference between the electrodes is how they were mounted in the cell, affecting their heat contact with the HFS. As noted in Chapter 3, the calibration assumes that the HFS was equally sensitive to Joule heat and to reversible heat produced in the porous network, which was not necessarily the case.

Figure 2.4 shows the data analysis of HFS voltage peaks of the type in Fig. 2.2(c), with heats of charging on the left and heats of discharging on the right. Time-integrated HFS voltages are in Fig. 2.4(a-b). When these units are scaled using the calibration factors determined in Fig. 2.3, the results are much closer to each other (Fig. 2.4(c-d)).

In Chapter 3, formulas for the heat of charging, q_{ch} , and the heat of discharging, q_{dis} , will be derived in terms of the electrode capacitance, the applied potential ΔV , an average electric potential $f\Delta V$ of ions inside the pores, and a

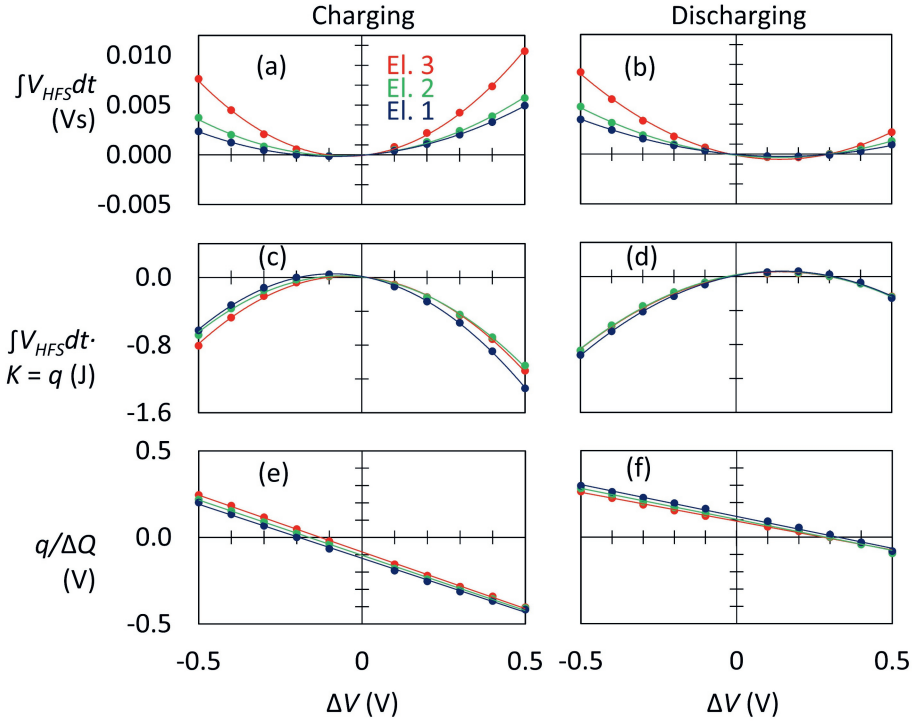


Figure 2.4: Typical HFS measurement results during charging and discharging for different electrodes, (a-b) integrated heat flux, (c-d) calibrated heat, (e) calibrated charging heats divided by ΔQ . A least squares fit to Eq. 2.3 gives $\Delta V_{\text{att}} = (-0.102 \pm 0.007) \text{ V}$ and $[-\frac{1}{2} - \frac{3}{2}f] = -0.640 \pm 0.002$. (f) Calibrated discharging heats divided by ΔQ . A least squares fit to Eq. 2.4 gives $\Delta V_{\text{att}} = (-0.105 \pm 0.007) \text{ V}$ and $[\frac{1}{2} - \frac{3}{2}f] = -0.354 \pm 0.002$.

potential-independent ΔV_{att} , which corresponds to an energy per unit charge due to attraction of the ions to the electrode surface. From those equations, dividing q_{ch} and q_{dis} by the measured charge $C\Delta V$ yields the following expressions:

$$\frac{q_{\text{ch}}}{C\Delta V} = \left[-\frac{1}{2} - \frac{3}{2}f \right] \Delta V + \Delta V_{\text{att}} \quad (2.3)$$

$$\frac{q_{\text{dis}}}{C\Delta V} = \left[-\frac{1}{2} + \frac{3}{2}f \right] \Delta V - \Delta V_{\text{att}}. \quad (2.4)$$

On the basis of these two formulas, parameters f and ΔV_{att} can be obtained from linear fits of $q/(C\Delta V)$ vs. ΔV , much like the linear fit of $\Delta U/(C\Delta V)$ that will be discussed in Chapter 3. In Figs. 2.4(e) and 2.4(f), plots of the heat of charging and discharging, divided by $\Delta Q = C\Delta V$ indicate the same values of ΔV_{att} . When the same measurements were performed using resistance temperature detectors instead of a heat flux sensor, similar results were obtained (but with lower signal-to-noise ratio), supporting the validity of the presented calibration approach, see Section 2.5.

2.3.2 HFS sensitivity for reversible heat

Our calibration approach assumes that the HFS has the same sensitivity for reversible heat and Joule heat, even though in practice, these two contributions to the total heat are not produced at the same location with respect to the HFS. In our test measurements, the reversible heat was fully produced in the porous network. The Joule heat, however, was generated in different resistive parts of the system. Part of the heat was generated by the silver epoxy glue contact at the side of the electrode, see Fig. 2.1(c), whose resistance was $<0.5\,\Omega$. Another part of the Joule heat was generated by electrical current through the bulk solution between the Luggin tube and WE, farther away from the HFS than the porous network. This can be concluded from the concentration dependence of the total cell resistance, equal to $3.3\,\Omega$ at 5 M NaCl, $5.7\,\Omega$ at 1 M NaCl, and $20.8\,\Omega$ at 0.1 M NaCl, for measurements on a typical electrode. These resistances correspond to a concentration-independent contribution of about $2.5\,\Omega$ plus the resistance of the liquid solution between Luggin tube and WE, given by $R = d/(\kappa A)$, where $1/\kappa$ is the concentration-dependent resistivity of aqueous NaCl solution obtained from Ref. [57], $d \approx 0.6\text{ cm}$ is the distance

between Luggin tube and WE, and $A \approx \pi(0.925 \text{ cm})^2$ is the external area of the WE exposed to bulk electrolyte solution. The thus calculated R is equal to 0.7Ω at 5 M, 2.2Ω at 1 M, and 17.5Ω at 0.1 M. Therefore, the resistance in the bulk electrolyte solution is dominant at 0.1 M NaCl, and it is about 40 % of the total resistance at 1 M NaCl and about 20% at 5 M NaCl.

The calibration constant was also concentration-dependent, indicating a sensitivity of $(-5.23 \pm 0.04) \times 10^{-3} \text{ Vs/J}$ at 5 M, $(-5.88 \pm 0.06) \times 10^{-3} \text{ Vs/J}$ at 1 M, and $(-6.72 \pm 0.02) \times 10^{-3} \text{ Vs/J}$ at 0.1 M NaCl. This can be understood in terms of where most of the Joule heat was produced. The lower the concentration, the more Joule heat was produced in bulk electrolyte solution, and the higher the sensitivity of the HFS to the Joule heat. The bulk solution is better centered with respect to the HFS than the resistive elements that give concentration-independent contributions to the total resistance, which are more to the side of the electrode, possibly not facing the HFS.

Reversible heat produced in the porous network will flow partly toward bulk solution and partly toward the HFS. However, toward the HFS, the thermal conductivity of the glassy carbon current collector is higher ($0.7\text{--}4 \text{ W/m/K}$) [58] than toward bulk solution, mostly consisting of water (0.6 W/m/K) [56]. This favors the flow of reversible heat in direction of the HFS. For 1 M NaCl, in the extreme case that all the reversible heat and all the Joule heat produced in the concentration-independent 2.5Ω resistive elements would flow in the direction of the HFS, and only half of the Joule heat produced in the bulk electrolyte solution would flow in the direction of the HFS, the HFS would detect 75 % of the Joule heat and 100 % of the reversible heat. This would lead to an overestimation of the reversible heat by 33 %, since our calibration is only on the Joule heat. In reality, the flow of reversible heat and Joule heat is likely to be more evenly distributed between the directions toward and away from the HFS, resulting in a lower overestimation of the reversible heat via our calibration method.

2.4 Conclusion

With the presented setup, the heat of charging and discharging of a capacitive electrode can be determined as a function of electrode potential with respect

to a reference electrode. In this way, differences between heat production in the anodic and cathodic ranges can be investigated. The heat flux sensor is calibrated using the Joule heat produced in a full cycle of charging and discharging. This partly solves the problem of not knowing which fraction of electrode heat flows in the direction of the sensor.

2.5 Appendix 1: Alternative setup with lock-in detection of RTDs using a Wheatstone bridge

In addition to the setup described, we also developed a setup in which electrode heat is detected using a Pt100 resistance thermometer detector (RTD). Results obtained with this alternative setup support the reliability of the calibration approach applied to the HFS data. For greater sensitivity than in Ref. [1], the RTD is connected in a Wheatstone bridge, a sinusoidal voltage is applied at high frequency, and the resulting bridge voltage is measured using a lock-in amplifier. With an ultra-thin Pt100 thermometer (TC Direct 515-113, 0.5 mm in diameter) with its tip centered behind the working electrode, only temperature effects coming from the WE are measured.

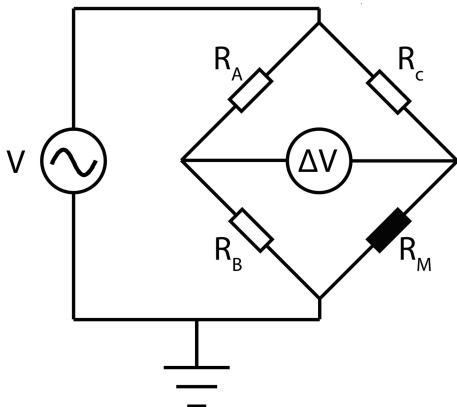


Figure 2.5: Four resistors connected in a Wheatstone bridge configuration, with R_M the Pt100 thermometer sensing the temperature of the WE and the three other Pt100 thermometers used as reference (R_A , R_B , R_C). A sinusoidal voltage of 500 mV in amplitude is applied at 100 kHz, and the resulting voltage ΔV is measured with a lock-in amplifier.

The ultra-thin Pt100 thermometer (R_M) is connected in a Wheatstone bridge configuration [59], shown in Fig. 2.5, together with three bulkier Pt100 (TC Direct 514-100) reference thermometers (R_A , R_B , R_C). These three references respond more slowly to temperature fluctuations than the ultra-thin Pt100, thus contributing less noise to the measured signal.

In principle, at homogeneous temperature, the bridge is balanced. When the temperature of thermometer R_M changes, its resistance changes, and thus

the voltage over the bridge changes. Using a Zürich Instruments HF2LI Lock-In Amplifier, a voltage of 500 mV is applied to the Wheatstone bridge at 100 kHz. The resulting voltage between the connection of R_A with R_B and the connection between R_C and R_M is measured.

The temperature difference is calculated as follows. When the bridge is not balanced, the ratio of measured voltage ΔV to applied voltage V is given by $R_A \approx R_B \approx R_C$:

$$\frac{\Delta V}{V} = \left[\frac{R_M}{R_C + R_M} - \frac{R_B}{R_A + R_B} \right] \approx \left[\frac{R_M}{R_A + R_M} - \frac{1}{2} \right] \quad (2.5)$$

The voltage difference informs on the difference in resistance between the Pt100 that senses the WE temperature and that of each reference Pt100.

$$R_M - R_A = \frac{4\Delta V R_A}{V - 2\Delta V} = \Delta R \quad (2.6)$$

The electrical resistance of the thermometers depends on the temperature: $R = 100 \, \Omega + KT$, where $K = 0.385005 \, \Omega/\text{K}$ (IEC 60751 standard), thus the difference in resistance between R_M and R_A is:

$$\Delta R = K(T_M - T_A) = K\Delta T. \quad (2.7)$$

The temperature difference is calculated by rearranging and combining Eq. 2.7 with Eq. 2.6:

$$\Delta T = \frac{1}{K} \Delta R = \frac{1}{K} \frac{4\Delta V R_A}{V - 2\Delta V}. \quad (2.8)$$

This formula is an approximation of the temperature difference, in which the resistance of the leads of the RTDs is neglected, even though they are nonzero and different for the two types of RTD used (R_A and R_M). This leads to an elevated baseline of ΔT versus time which can, however, be subtracted during analysis of the data.

The calibration of the setup is comparable to the calibration of the HFS, except that HFS voltage is replaced by ΔT . In Fig. 2.6, which is comparable to Fig. 2.2, results of a typical measurement are shown. The signal-to-noise ratio of the highest peak is 130:1 in Fig. 2.6, thus, more than one order of magnitude smaller than the HFS setup. The setup is more vulnerable to outside temperature fluctuations than the HFS setup and the current through

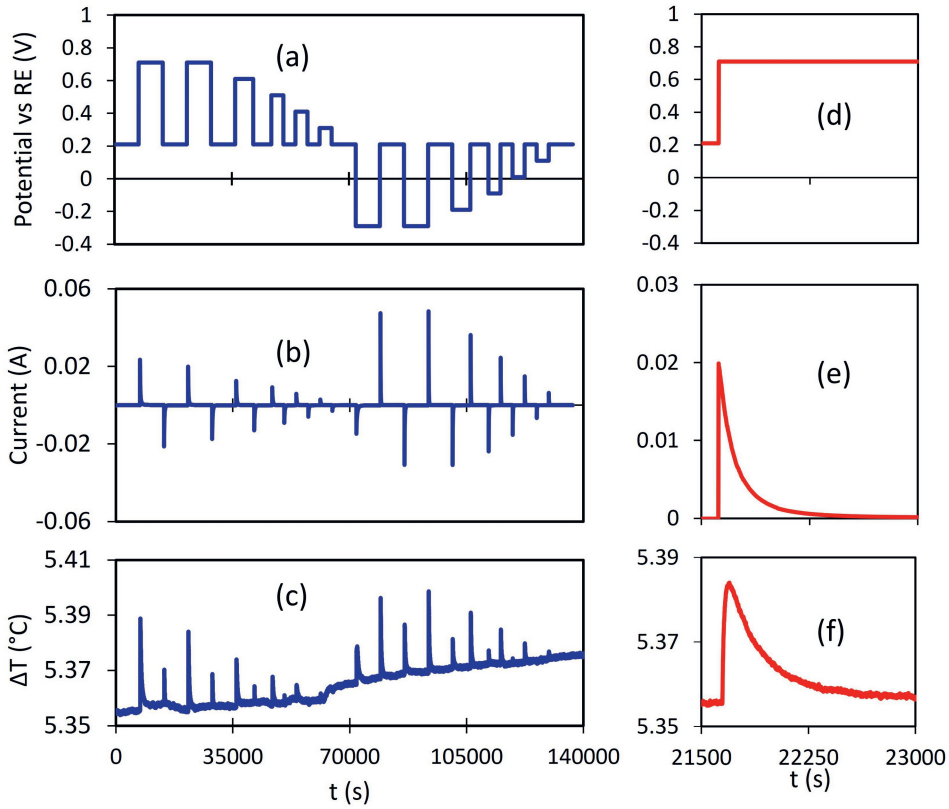


Figure 2.6: Typical electrical and temperature difference measurements on a porous carbon electrode in 1 M aqueous NaCl with (a) the applied potential vs RE; (b) the resulting current, and (c) the temperature difference calculated via Eq. 2.8. (d)-(f) Shape of the signals in (a)-(c), respectively, during charging from 0.21 V to 0.71 V (potentials versus RE; 0.21 V is the open circuit potential).

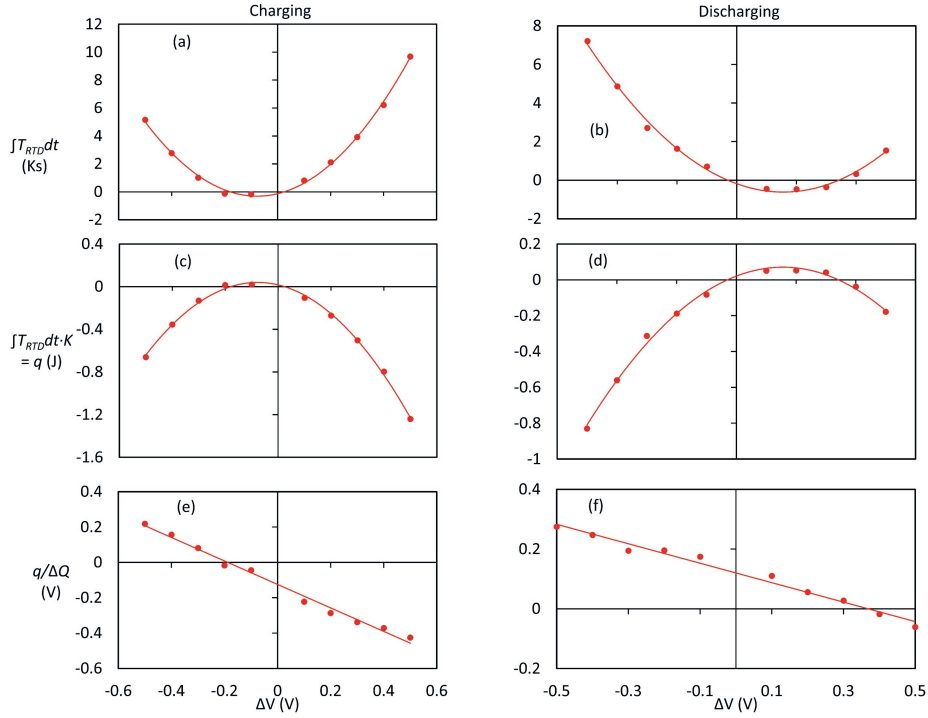


Figure 2.7: Typical RTD measurement results during charging and discharging, (a-b) integrated temperature differences, (c-d) calibrated heats, (e) calibrated charging heats divided by $C\Delta V$. A least squares fit to Eq. (2.3) gives $\Delta V_{\text{att}} = (-0.109 \pm 0.024) \text{ V}$ and $[-\frac{1}{2} - \frac{3}{2}f] = -0.660 \pm 0.008$. (f) Calibrated discharging heats divided by $C\Delta V$. A least squares fit to Eq. (2.4) gives $\Delta V_{\text{att}} = (-0.120 \pm 0.016) \text{ V}$ and $[\frac{1}{2} - \frac{3}{2}f] = -0.326 \pm 0.005$.

the RTDs causes their heating, effects revealed by the baseline.

Fig. 2.7 shows the results of the RTD setup in the same way as Fig. 2.4. The results are comparable to those with the HFS setup presented. Nevertheless, the higher signal-to-noise ratio and the better thermostatzation make the HFS a better option for the measurements.

Chapter 3

Electric Potential of Ions in Electrode Micropores Deduced from Calorimetry

Abstract

The internal energy of capacitive porous carbon electrodes was determined experimentally as a function of applied potential in aqueous salt solutions. Both the electrical work and produced heat were measured. The potential dependence of the internal energy is explained in terms of two contributions, namely the field energy of a dielectric layer of water molecules at the surface and the potential energy of ions in the pores. The average electric potential of the ions is deduced, and its dependence on the type of salt suggests that the hydration strength limits how closely ions can approach the surface.

3.1 Introduction

In porous electrodes, the interface between solid conductor and liquid-phase ions is at the pore walls. Charge separation between solid and liquid occurs within less than a nanometer, and consequently, electrodes that largely consist of micropores (1–2 nm in width) have a huge electrified surface area. With carbon material, it can exceed 1000 m² per gram of solid, which allows for energy storage at high density. Moreover, since the charging process is rapid and reversible, “electrical double layer capacitors” are suitable for automotive and consumer applications [35, 60]. Microporous electrodes are also applied in “capacitive deionization”, to produce drinking water by removing salt from brackish water [9, 13, 61]. Conversely, electrical energy can be harvested from the mixing of dilute and concentrated salt solutions using capacitive electrodes [62, 63].

The capacitance of a porous electrode provides experimental information about the electrical double layer inside the pores. From measurements at different ion-to-pore size ratios, it is clear that pores too narrow to accommodate ions do not store charge [37, 64]. Nevertheless, solvated ions can lose their solvation shells when they enter into micropores [19, 20, 21, 22]. In the field of capacitive deionization, theoretical models typically interpret the measured capacitance in terms of a dielectric layer of water molecules adsorbed at the pore walls (the “Stern layer”) and an adjacent diffuse ionic layer [17, 18]. The uptake of salt by microporous electrodes has been explained on the basis of a modified Donnan equilibrium, assuming that all in-pore ions are at the same electric potential [11, 14]. More detailed insights can be obtained from numerical simulations, for instance using density functional theory or molecular dynamics [65, 66, 67]. Calculations as a function of distance from a pore wall show different profiles of the electric field and concentrations of ions, depending on the distance between opposing walls [68, 69, 70, 71].

In this chapter, we propose an experimental thermodynamic approach to characterize the average electric potential of ions inside a microporous electrode. The electrode is alternately charged or discharged, and the associated changes in internal energy are calculated from the amount of electrical work performed on the electrode [70] and from the exchanged heat, measured via calorimetry [23, 24, 25, 26, 27, 28, 29, 50]. The changes in internal energy are

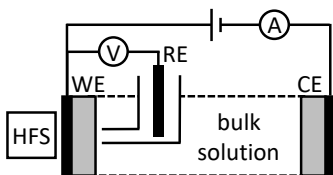


Figure 3.1: Schematic of the experimental setup.

dominated by the field energy of the electrical double layer, whose contribution scales quadratically with applied potential. However, this contribution is smaller than expected from the capacitance. Our explanation is that changes in applied potential do not fall fully across the capacitive part of the electrical double layer. The average electric potential of the ions in the pores is changed as well. Moreover, the internal energy is also affected by the attraction of ions to the carbon surface.

3.2 Experimental

Experiments were conducted on microporous carbon electrodes in aqueous salt solutions. Both WE and CE were porous carbon disks of the same material, with a diameter of 21 mm, a thickness of ~ 0.25 mm, a mass of 63 mg, a specific surface area of $1400 \text{ m}^2/\text{g}$, a porosity of 60%, and an average distance between opposing pore walls of ~ 0.9 nm, see Section 3.9. The porous working electrode (WE) was connected to an Ag/AgCl reference electrode (RE) and a porous carbon counter electrode (CE), see Fig. 3.1. Heat from the WE was measured with a heat flux sensor (HFS). Our experimental approach was inspired by Janssen et al.[1], with important differences. Rather than being measured from a complete electrochemical cell, heat was now detected from a single electrode; see Fig. 3.1. Heat from the WE was measured with a heat flux sensor, the ‘HFS’. More details about the setup can be found in Chapter 2.

The open circuit potential obtained after prolonged equilibration was chosen as the null point of applied potentials ΔV . Initially, at $\Delta V = 0 \text{ V}$, the electrical current I and HFS voltage V_{HFS} were close to zero. Then abruptly, a nonzero ΔV was applied, resulting in peaks of I and V_{HFS} ; see Fig. 3.2. After 1 to 2 hours, $\Delta V = 0 \text{ V}$ was applied again. This charging-discharging

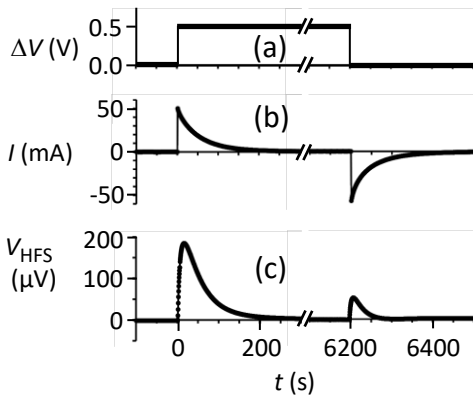


Figure 3.2: Measurement of a charging-discharging cycle (1 M NaCl, 22° C): time dependence of (a) applied potential referenced to open circuit potential after prolonged equilibration, (b) electrical current, and (c) voltage of the heat flux sensor.

cycle was repeated for $\Delta V = -0.5 \text{ V}$ to $+0.5 \text{ V}$. The results were interpreted using the following model.

3.3 Theory

The studied thermodynamic system consists essentially of four elements: (1) conductive carbon that is at the externally applied potential, (2) a dielectric layer of water molecules adsorbed at the pore walls, (3) ionic solution inside the pores, and (4) a nearby part of the bulk electrolyte solution reservoir, at constant electric potential V_{bulk} . Experiments start with prolonged equilibration at open circuit, until the carbon reaches an electric potential $V_{\text{OCP,eq}}$. We neglect the presence of surface charge at open circuit, as was done in the interpretation of potential-dependent salt adsorption experiments on the same electrode material [14]. This implies that $V_{\text{OCP,eq}} = V_{\text{bulk}}$.

During charging, an electronic charge $+\Delta Q$ is added to carbon from the external circuit at potential $V_{\text{OCP,eq}} + \Delta V$ and an ionic charge $-\Delta Q$ is added from bulk solution at potential $V_{\text{OCP,eq}}$. The total electrical work on the system is therefore

$$w_{\text{ch}} = \Delta Q \Delta V. \quad (3.1)$$

The measurements are essentially isothermal [1], and pressure-volume work is neglected. The energy change during charging is the sum of electrical work performed on the system and heat q_{ch} added to the system:

$$\Delta U_{\text{ch}} = \Delta Q \Delta V + q_{\text{ch}}. \quad (3.2)$$

During discharging, the electrical work on the system is

$$w_{\text{dis}} = 0 \quad (3.3)$$

since ΔQ is removed from carbon at $\Delta V = 0$ V and ionic charge $-\Delta Q$ exits the system at $V_{\text{OCP,eq}}$. The energy change now equals the discharging heat q_{dis} :

$$\Delta U_{\text{dis}} = q_{\text{dis}}. \quad (3.4)$$

For a full charging-discharging cycle, the total change in internal energy ΔU is zero, since the system begins and ends in the same state. Combining Eqs. (3.2) and (3.4) gives

$$q_{\text{ch}} + q_{\text{dis}} = -\Delta Q \Delta V. \quad (3.5)$$

This is the irreversible heat produced in resistive parts of the system. The HFS can be calibrated on this basis; see the Results, Section 3.4.

In order to interpret the experimental values of $\Delta U_{\text{ch}} = -\Delta U_{\text{dis}}$, it is assumed that the system's energy change consists of two contributions: the change ΔU_{w} in field energy of the dielectric water layer and the change ΔU_{ions} in potential energy of the ions in the pores:

$$\Delta U_{\text{ch}} = \Delta U_{\text{w}} + \Delta U_{\text{ions}}. \quad (3.6)$$

Similarly, the change ΔV in applied potential consists of a change ΔV_{w} in voltage across the dielectric water layer and a change ΔV_{ions} in the average electric potential of the ionic solution inside the pores:

$$\Delta V = \Delta V_{\text{w}} + \Delta V_{\text{ions}}. \quad (3.7)$$

It is assumed that ΔV_{ions} is a fraction f of the change in applied potential:

$$\Delta V_{\text{ions}} = f\Delta V. \quad (3.8)$$

The associated change in voltage across the dielectric water layer is given by

$$\Delta V_{\text{w}} = (1 - f)\Delta V. \quad (3.9)$$

In our experiments, the measured capacitance C of the electrode is approximately constant:

$$\Delta Q = C\Delta V. \quad (3.10)$$

The combination of Eqs. (3.9) and (3.10) indicates that the capacitance of the dielectric water layer is given by

$$C_{\text{w}} = C/(1 - f). \quad (3.11)$$

Consequently, the change in field energy during charging is given by:

$$\Delta U_{\text{water}} = \int_0^{(1-f)\Delta V} VC_{\text{water}} dV = \frac{1}{2}(1 - f)C(\Delta V)^2. \quad (3.12)$$

The energy change of the ionic solution is assumed to consist of two contributions: the electrical work to bring the countercharge $-C\Delta V$ to the in-pore potential $f\Delta V$, and an energy change $C\Delta V\Delta V_{\text{att}}$ resulting from an attraction between the ions and carbon surface:

$$\Delta U_{\text{ions}} = -fC(\Delta V)^2 + C\Delta V\Delta V_{\text{att}}. \quad (3.13)$$

ΔV_{att} has units of V and represents a change in potential energy per elementary charge. The total energy change follows from Eqs. (3.6), (3.12), and (3.13):

$$\Delta U_{\text{ch}} = \left[\frac{1}{2} - \frac{3}{2}f \right] C(\Delta V)^2 + C\Delta V\Delta V_{\text{att}}. \quad (3.14)$$

Using Eqs. (3.2), (3.5), and (3.14), expressions for the heats of charging and

discharging are found:

$$q_{\text{ch}} = \left[-\frac{1}{2} - \frac{3}{2}f \right] C(\Delta V)^2 + C\Delta V\Delta V_{\text{att}} \quad (3.15)$$

$$q_{\text{dis}} = \left[-\frac{1}{2} + \frac{3}{2}f \right] C(\Delta V)^2 - C\Delta V\Delta V_{\text{att}}. \quad (3.16)$$

When it is assumed that the irreversible heat q_{irr} is approximately the same upon charging and discharging [1], it is given by

$$q_{\text{irr}} \cong \frac{q_{\text{ch}} + q_{\text{dis}}}{2} = -\frac{1}{2}C(\Delta V)^2 \quad (3.17)$$

and the reversible heat q_{rev} is given by

$$q_{\text{rev}} \cong \frac{q_{\text{ch}} - q_{\text{dis}}}{2} = -\frac{3}{2}fC(\Delta V)^2 + C\Delta V\Delta V_{\text{att}}. \quad (3.18)$$

3.4 Results

Analysis of the experimental data started by integrating the current peaks, to obtain the change in equilibrium charge ΔQ ; see Fig. 3.3(a). The measured charge was linear with applied potential and opposite during charging (ΔQ_{ch}) and discharging (ΔQ_{dis}). Capacitance was slightly higher in the cathodic range ($\Delta V < 0$) than in the anodic range ($\Delta V > 0$); see Table 3.1.

Integration of a peak of the HFS voltage yielded the heat in HFS units (Vs), different upon charging (q_{ch}) or discharging (q_{dis}); see Fig. 3.3(b). As expected from Eq. (3.5), the integral of the two HFS voltage peaks was proportional to $-\Delta Q\Delta V$; see Fig. 3.3(d). The same proportionality constant in units of J/(Vs) was used to convert the separate heats of charging and discharging into energy units; see Fig. 3.3(b). This assumed that the HFS had the same sensitivity to reversible heat produced by the porous network and to Joule heat, used for the calibration. This assumption was not necessarily correct, for instance since part of the Joule heat was produced farther away from the HFS than the reversible heat. Some Joule heat came from a silver epoxy glue contact near the edge of the current collector. Some Joule heat was also generated by electrical current through the electrolyte solution between the reference electrode and the WE; this heat was concentration- and salt-

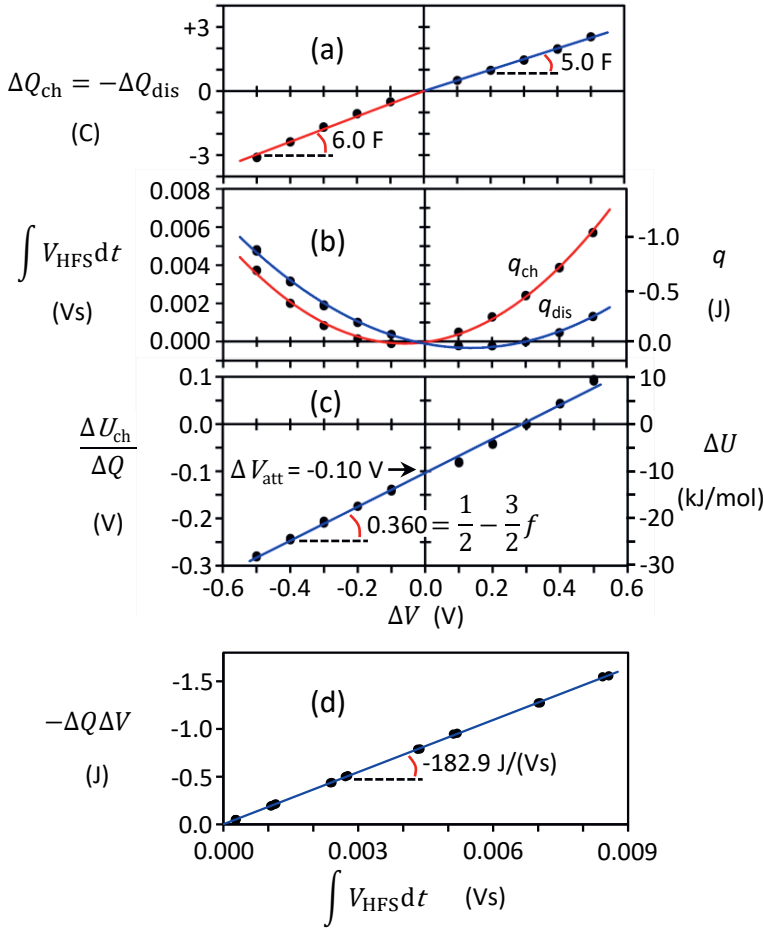


Figure 3.3: Data analysis approach, illustrated for 1 M NaCl at 22 °C: (a) Potential dependence of equilibrium charge. (b) Potential dependence of the heats of charging and discharging, in sensor units (left y axis) and energy units (right y axis). (c) Potential dependence of the charging energy [see Eq. (3.19)]; the right y axis gives charging energy in kJ/mol. (d) Irreversible heat $-\Delta Q \Delta V$ versus integrated HFS signal for a full charging-discharging cycle; see Eq. (3.5).

dependent, due to differences in electrical conductivity (see Section 2.3.2). The HFS was probably the most sensitive to heat generated in the porous network, close to and centered with respect to the HFS. Since reversible heat scales linearly with f and ΔV_{att} [see Eq. (3.18)], an overestimation of the reversible heat by 33% (in an extreme scenario, see Section 2.3.2) would also overestimate f and ΔV_{att} by 33%.

The same absolute ΔU was obtained via Eqs. (3.2) and (3.4). In kJ/mol, the results were comparable for different salt solutions. In all cases, a plot of $\Delta U/\Delta Q$ versus ΔV as in Fig. 3.3(c) gave a straight line with a negative y intercept, see Section 3.10. Table 3.1 shows the values of constants f and ΔV_{att} from the fitting of results obtained at 22 °C to the following equation, obtained by dividing the terms in Eq. (3.14) by $\Delta Q = C\Delta V$:

$$\frac{\Delta U_{\text{ch}}}{\Delta Q} = \left[\frac{1}{2} - \frac{3}{2}f \right] \Delta V + \Delta V_{\text{att}}. \quad (3.19)$$

Temperature-dependent measurements with 1 M NaCl indicated that the absolute values of f and ΔV_{att} increased with temperature; see Section 3.8. For all salts, the largest ΔU was measured at $\Delta V = -0.5$ V, ranging from -25 kJ/mol (CsCl) to -40 kJ/mol (LaCl_3). This is much less than the full hydration enthalpies of the ions [72], which range from -280 kJ/mol for Cs^+ to -3310 kJ/mol for La^{3+} ; see Table 3.1. This suggests that dehydration of ions as they entered into micropores was not a strong effect in our experiments.

3.5 Discussion

To compare the experimental results to theoretical models of the electrical double layer, one approach is to focus on the reversible heat. In Ref. [1], it was identified as the entropic contribution to the grand potential, in agreement with Overbeek [74]. Glatzel et al. [32] supported this identification using density functional theory and calculated the negative ratio of reversible heat q_{rev} and electrical work w_{el} . For our experiments, Eq. (3.18) and $w_{\text{el}} = \frac{1}{2}C\Delta V^2$ indicate that this ratio is given by

$$-q_{\text{rev}}/w_{\text{el}} = +3f - 2\Delta V_{\text{att}}/\Delta V. \quad (3.20)$$

Table 3.1: Measured cathodic and anodic capacitances, and internal energy parameters f and ΔV_{att} from Eq. (3.14), for different aqueous salt solutions at 22 °C. Results at 1 M are given in order of increasing cationic hydration strength, as indicated by hydration enthalpy ΔH_{hyd} and hydration numbers from electrostatic modeling (N_{mod}) and electrochemical quartz crystal microbalance measurements (N_{EQCM}). For chloride, $-\Delta H_{\text{hyd}} = 365 \text{ kJ/mol}$ [72], $N_{\text{mod}} = 2.0$ [72], and $N_{\text{EQCM}} = 0.6$ [73].

Salt solution	C_{cathodic} (F) ± 0.2	C_{anodic} (F) ± 0.2	f ± 0.010	ΔV_{att} (V) ± 0.020	Cation	$-\Delta H_{\text{hyd}}$ [72] (kJ/mol)	N_{mod} [72]	N_{EQCM} [73]
1 M CsCl	6.1	5.1	0.109	-0.092	Cs ⁺	280	2.1	0.5
1 M RbCl	5.9	5.1	0.099	-0.095	Rb ⁺	305	2.4	-
1 M KCl	5.9	5.0	0.101	-0.107	K ⁺	330	2.6	1.3
1 M NaCl	6.0	5.0	0.093	-0.103	Na ⁺	415	3.5	2.2
1 M LiCl	6.1	5.0	0.079	-0.125	Li ⁺	530	5.2	2.6
1 M CaCl ₂	6.9	6.1	0.064	-0.155	Ca ²⁺	1600	7.2	3.7
1 M MgCl ₂	7.1	5.3	0.059	-0.122	Mg ²⁺	1945	10.0	5.8
1 M LaCl ₃	7.0	6.1	0.029	-0.148	La ³⁺	3310	10.3	-
0.1 M NaCl	5.3	4.8	0.119	-0.078				
5 M NaCl	6.7	5.7	0.081	-0.125				

One of the conclusions in Ref. [32] is that steric ion interactions play a key role in determining the $-q_{\text{rev}}/w_{\text{el}}$ ratio. Ion-wall interactions were not taken into account in Ref. [32], corresponding to the case where $\Delta V_{\text{att}} = 0$ V. Larger hydrated ions lead to a smaller $-q_{\text{rev}}/w_{\text{el}}$ ratio, in line with the small values of f that we find for solutions with Mg^{2+} , Ca^{2+} , and La^{3+} , our most strongly hydrated ions. Theory predicts that the $-q_{\text{rev}}/w_{\text{el}}$ ratio becomes smaller at increasing ionic strength [32], in line with the relatively small values of f that we find in 5 M NaCl and 1 M LaCl_3 , although theory overestimates the measured effects. One source of discrepancy is uncertainty about the dielectric constant of water inside micropores, expected to be much closer to that of ice than to that of liquid water [14, 75]. Calculation (see Section 3.9) shows that our electrodes have the capacitance of a parallel plate capacitor with the thickness of a water molecule and a dielectric constant of 2.1, the experimental value for water between capacitor plates 1 nm apart [75]. Another source of discrepancy is the possibly higher sensitivity of the HFS to reversible heat than to Joule heat, an effect for which no corrections were made in our data analysis.

Our alternative approach to interpret the data focuses on the change in internal energy. The parameter f describes which part of a change in applied potential is felt on average by ions in the pores. One theory that gives a constant value of the electric potential in micropores is the modified Donnan theory [14], but it is not applicable here, since most of our experiments were at high ionic strength (≥ 1 M), where diffuse layer overlap is negligible. At high ionic strengths, theoretical calculations predict that much of the net ionic charge is close to the surface [68, 69, 76, 77]. In our measurements, the weakness of the measured heat effects and the similar capacitances found with different salts suggest that steric hindrance is not a strong limiting factor for the entry of ions into the micropores. The ionic core diameters range from 0.14 nm (Li^+) to 0.36 nm (Cl^-) [72], the Stokes diameters from 0.24 nm (Cs^+) to 0.48 nm (Li^+) [78, 79, 80], and the hydrated ion diameters from electrostatic modeling from 0.42 nm (K^+) to 0.62 nm (La^{3+}) [72]. This remains smaller than the wall-to-wall distance of 0.9 nm, an average of local values [37, 81]. Nevertheless, there is a trend between the value of f and the strength with which the ions are hydrated. Our least hydrated ions are Cl^- , Cs^+ , Rb^+ , K^+ , and

Na^+ , whereas Li^+ , Ca^{2+} , Mg^{2+} , and La^{3+} are more strongly hydrated, in that order, as indicated by hydration enthalpies and hydration numbers from electrostatic modeling [72] and electrochemical quartz microbalance measurements [73], see Table 3.1. Our results agree with the view that weakly hydrated ions come relatively close to the pore walls, where the electric potential changes strongly with applied potential—resulting in relatively high values of f —and that strongly hydrated ions remain farther away from the pore walls due to steric hindrance, resulting in lower values of f . This does raise the question of why this trend is not only observed in the cathodic range, where the cations are the counterions, but also in the anodic range, where the counterions are chloride. Our explanation is that at 1 M salt concentration, the ionic strength is sufficiently high that “ion swapping” occurs [37]. Both types of ions are present in the pores across the entire potential range, and a positive shift in applied potential causes an exchange of positive ions by negative ions.

The origin of the ion attraction parameter ΔV_{att} remains speculative. The typical value of -0.1 V corresponds to $-4k_{\text{B}}T$ per elementary charge. Direct evidence for the attraction of ions to the electrode surface was given by the detection of excess salt inside micropores in the absence of an externally applied potential [14, 36], and this was ascribed to image charge attraction [14, 82, 83, 84]. However, the resulting contribution to the potential energy would then probably depend on the applied potential [14], whereas in the fitting of our data, ΔV_{att} is a constant. An alternative is a more chemical explanation, for instance involving Van der Waals attraction [66, 85]. In the present work, the ΔV_{att} parameter can be viewed as an empirical way to account for the asymmetry of measured heat versus applied potential. In most of our experiments, the reversible charging heat is clearly exothermic in the anodic range and endothermic in the cathodic range, an example of electrostatic cooling [86]. Although we ascribed the origin of the ΔV_{att} parameter to ion-carbon attraction, it cannot be ruled out that ΔV_{att} partly originates from the presence of net surface charge at open circuit. It is noted that the ΔV_{att} parameter could not be detected in earlier measurements of the total heat from the cathode and anode [1], since the $\pm\Delta Q\Delta V_{\text{att}}$ contribution to the (dis)charging heat of the cathode canceled with the $\mp\Delta Q\Delta V_{\text{att}}$ contribution to the (dis)charging heat of the anode; see Eqs. (3.15) and (3.16).

3.6 Conclusion

The potential-dependent internal energy of porous carbon electrodes was determined experimentally. The precise scaling of the internal energy with applied potential was interpreted in terms of the average electric potential felt by ions inside the pores, which depends on the hydration strength of the ions. Moreover, a nonzero potential energy of the ions at open circuit was ascribed to a potential-independent attraction of the ions to the carbon surface. In the future, calorimetric measurements could be valuable to characterize the electrical double layer inside other types of porous electrodes, for instance supercapacitors. Also, numerical simulations using molecular dynamics or density functional theory could be performed to account for our experimental results. Moreover, further experimental information could be obtained about our experimental system, for instance by detecting in-pore ionic concentrations via *in situ* NMR spectroscopy.

3.7 Appendix 1: Purity and Provenance of the Chemicals

The purity and provenance of the salts are indicated in Table 3.2.

Table 3.2: The salts.

Salt	Purity	Provenance
NaCl	for analysis	Merck Emsure [®]
KCl	for analysis	Merck Emsure [®]
RbCl	99+%	Acros Organics
LiCl	for molecular biology, $\geq 99\%$	Sigma
CsCl	for molecular biology, $\geq 98\%$	Sigma
MgCl ₂	$\geq 99\%$, p.a., ACS	Roth
CaCl ₂	99+%, for analysis	Acros Organics
LaCl ₃	ACS reagent	Sigma-Aldrich

Milli-Q water has the electrical conductivity of pure water and is obtained by filtration of regular deionized water using a Milli-Q water purification system from Merck Millipore. Solutions were purged by ultrasonication, to remove dissolved gases.

As indicated in Ref. [14], “The carbon electrodes are based on a commercial material provided by Voltea B.V. (Sassenheim, The Netherlands) which contained activated carbon, polymer binder, and carbon black.” This material was used in Refs.[14, 10, 87, 88, 89, 90, 91]. Its composition is presumably comparable to that prepared in Kim et al. [36].

3.8 Appendix 2: Temperature-dependent measurements

Preliminary temperature-dependent measurements were performed at ten applied potentials as in Fig. 3.3, in triplicate at different temperatures, taking several weeks. Qualitative behavior was the same as at 22° C, with plots of $\Delta U/\Delta Q$ versus ΔV giving a straight line as in Fig.3.3(c), with a similar slope and y -intercept. However, during this lengthy measurement series, changes occurred to the system (in particular, leakage of KCl from the reference electrode), and final measurements at 22° C were no longer the same as initially,

within measurement error. To shorten the measurement time and thus to obtain more reliable results, measurements were subsequently performed only at $\Delta V = -0.5 \text{ V}$ and $\Delta V = +0.5 \text{ V}$ in 1 M NaCl, five times at each potential, at five temperatures from 5 to 39° C.

Data analysis was performed much like described in Section 3.2, but now on individual measurements at different potentials and temperatures. On the basis of Eqs. (3.2), (3.4), and (3.5), the internal energy changes upon charging and discharging could be calculated as follows:

$$\Delta U_{\text{ch}} = \Delta Q \Delta V \left(1 - \frac{q_{\text{ch}}}{q_{\text{ch}} + q_{\text{dis}}} \right) \quad (3.21)$$

$$\Delta U_{\text{dis}} = \Delta Q \Delta V \left(-\frac{q_{\text{ch}}}{q_{\text{ch}} + q_{\text{dis}}} \right), \quad (3.22)$$

using the heats of charging (q_{ch}) and discharging (q_{dis}) in units of the HFS sensor (Vs). The thus obtained internal energy changes were divided by the change in charge, for analysis on the basis of Eq. (19):

$$\frac{\Delta U_{-0.5V}}{\Delta Q_{-0.5V}} = (-0.5V) \left[\frac{1}{2} - \frac{3}{2}f \right] + \Delta V_{\text{att}} \quad (3.23)$$

$$\frac{\Delta U_{+0.5V}}{\Delta Q_{+0.5V}} = (+0.5V) \left[\frac{1}{2} - \frac{3}{2}f \right] + \Delta V_{\text{att}}, \quad (3.24)$$

where the subscripts of ΔU and ΔQ indicate the potential ΔV . The values of f and ΔV_{att} were solved from Eqs. (3.3) and (3.4):

$$f = \frac{2}{3} \left[\frac{1}{+1V} \left(\frac{\Delta U_{-0.5V}}{\Delta Q_{-0.5V}} - \frac{\Delta U_{+0.5V}}{\Delta Q_{+0.5V}} \right) + \frac{1}{2} \right] \quad (3.25)$$

$$\Delta V_{\text{att}} = \frac{1}{2} \left[\frac{\Delta U_{-0.5V}}{\Delta Q_{-0.5V}} + \frac{\Delta U_{+0.5V}}{\Delta Q_{+0.5V}} \right]. \quad (3.26)$$

Fig. 3.4 shows the temperature dependences of (a) the cathodic and anodic capacitances, (b) the value of f from Eq. (3.25), and (c) the value of ΔV_{att} from Eq. (3.26). The absolute values of f and ΔV_{att} become larger with increasing temperature, within sizeable experimental error. Temperature dependence probably results from several contributions, including the temperature dependences of the dielectric constants and the double layer structure.

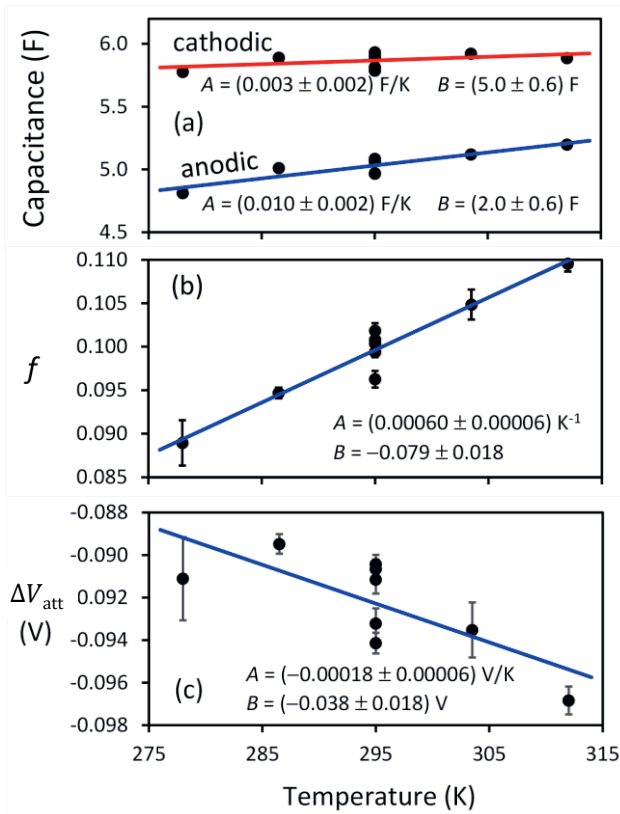


Figure 3.4: Temperature dependence of results for porous carbon electrodes in 1 M NaCl: (a) electrical capacitance at $\Delta V = -0.5 \text{ V}$ (cathodic) and $\Delta V = +0.5 \text{ V}$ (anodic), (b) fit parameter f from Eq. (3.25), and (c) fit parameter ΔV_{att} from Eq. (3.26). The slope A and y -intercept B from a least squares fit to $y = Ax + B$ is indicated next to each fit line.

3.9 Appendix 3: Nitrogen physisorption measurements and analysis

To determine the size and volume of the pores, and the total surface area, nitrogen physisorption was performed using a TriStar Plus II (Micromeritics) apparatus, at 77 K on samples of 18 mg. Samples consisted of porous electrode material that was either unused ('dry') or pretreated for several days at room

temperature in Milli-Q water ('water') or in 1 M aqueous NaCl ('NaCl'). All samples were dried under vacuum at 90 °C before measurement. Table 3.3 reports the BET surface area [92], the BJH desorption volume and several values from t-plot analysis [93]: total surface area, volume of micropores (<2 nm), volume of mesopores (2-50 nm). The results after pretreatment in water—see Fig. 3.5—are presumably the most representative for the situation during the capacitive charging experiments, since untreated porous material is likely to swell in water and dried salt solution will fill part of the pores with salt. A 63 mg porous electrode thus has a micropore volume on the order of 0.032 cm³.

Assuming flat parallel pores with a total surface area of A and a pore width of D , the total pore volume is $AD/2$ (since a pore has two parallel walls of equal area), so that experimental values of $A = 1400 \text{ m}^2/\text{g}$ and $AD/2 = 0.6 \text{ cm}^3/\text{g}$ imply an average distance of $2 \times (6 \times 10^{-7} \text{ m}^3/\text{g}) / (1400 \text{ m}^2/\text{g}) = 0.86 \text{ nm}$ between opposing walls of a pore.

The capacitance C of our electrodes is about 5 F ($\sim 6 \mu\text{F}/\text{cm}^2$), in agreement with the expression $C = (1-f)A(2.1)\varepsilon_0/d$ for a parallel plate capacitor. The factor $(1-f) \sim 0.9$ for NaCl originates from Eq. (9), $A = 88 \text{ m}^2$ is the surface area of the electrode, 2.1 is the dielectric constant of water determined experimentally between two flat plates 1 nm apart [75], ε_0 is the dielectric permittivity in free space, and $d = 0.3 \text{ nm}$ is on the order of the diameter of a water molecule.

In the context of theoretical predictions of the capacitance [76], we note that our measurements are near the limit of low charge density, at most about $0.04 \text{ C}/\text{m}^2$ at $\Delta V = +0.5 \text{ V}$ ($0.25 e/\text{nm}^2$).

3.10 Appendix 4: Additional HFS Results

Table 3.4 is an extended version of Table 3.4. The columns give (1) the salt solution, (2) the calibration constant from a plot of $-\Delta Q \Delta V$ versus the integrated HFS voltage for a charging-discharging cycle as in Fig. 3.3(d), (3) the slope of a plot of $\Delta U/\Delta Q$ versus ΔV as in Fig. 3.3(c), (4) the y -intercept ΔV_{att} of the plot of $\Delta U/\Delta Q$ versus integrated HFS voltage, (5) the value of f from the slope in column (3) via Eq. (3.19), (6) the capacitance in the cathodic range, and (7) the capacitance in the anodic range. Figure 3.6 shows

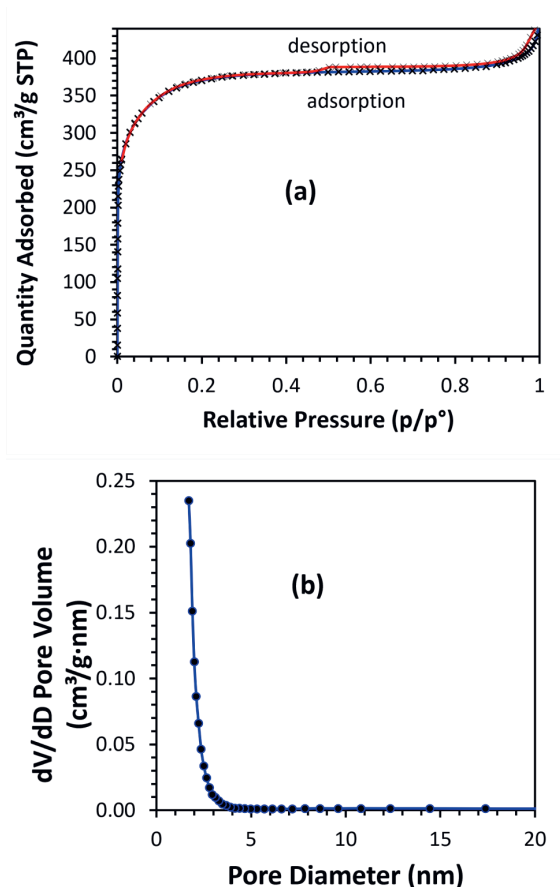


Figure 3.5: N₂ adsorption and desorption analysis of porous carbon pretreated in water: (a) adsorption and desorption isotherms at 77 K and (b) BJH pore size distribution [94].

plots of $\Delta U/\Delta Q$ versus ΔV for the studied systems, where data points for ΔU have been calculated from Eqs. (3.2) and (3.4).

The errors in Table 3.4 are from least squares fitting to the relevant linear equations. Larger errors are given in Table 3.1, for legibility and to take into account the reproducibility of the results upon measuring on different electrodes or versions of the electrochemical cell. The fraction of electrode heat that flows in direction of the sensor is a poorly known function of the thermal properties of materials on both sides of the electrode and of the quality of the heat contact between electrode and sensor. The (a) series was measured

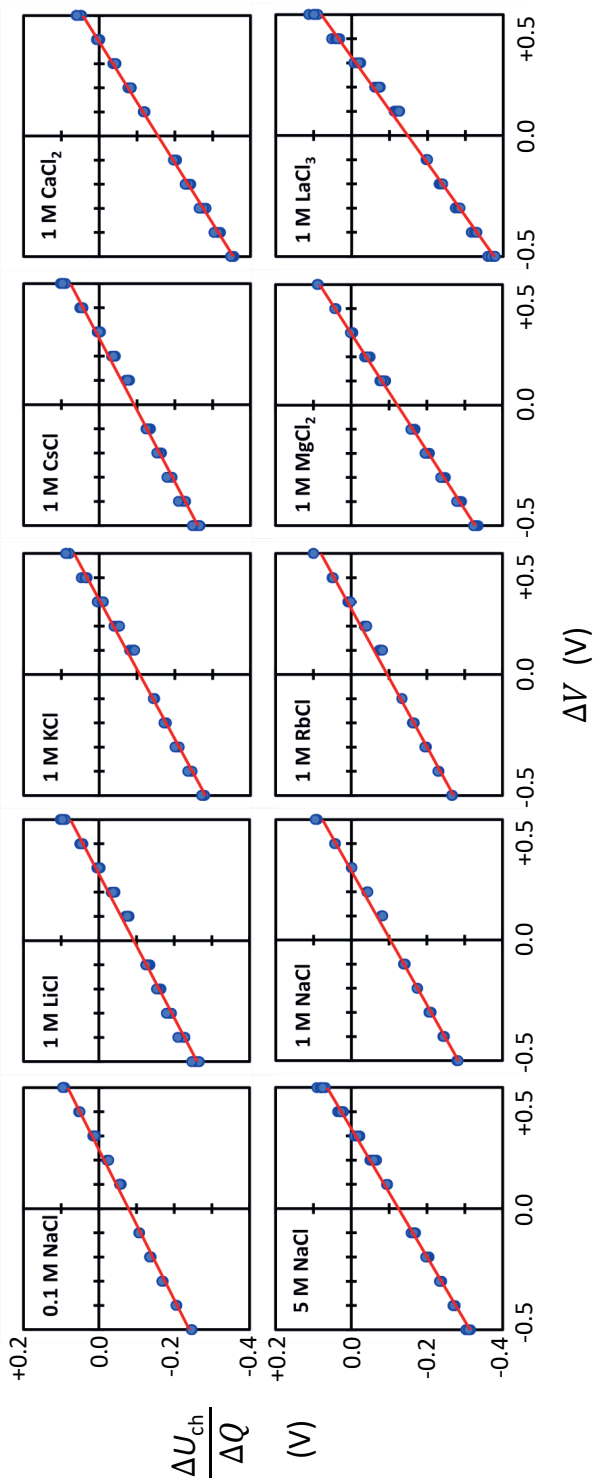


Figure 3.6: Plots of $\Delta U/\Delta Q$ versus ΔV for the studied systems. As mentioned in Section 3.4, in all cases, the points fall on a straight line with similar y -intercepts and similar slopes.

Table 3.3: Nitrogen adsorption analysis results. The surface area was determined using the BET equation (fitting range $p/p_0 = 0.02-0.1$) and the micropore volume was determined via the t-plot method ($0.4 < p/p_0 < 0.5$). The total pore volume was derived from the amount of nitrogen adsorbed at $p/p_0 = 0.995$. As the samples had a small amount of larger mesopores, the t-plot was fitted in a second range, $0.5 < p/p_0 < 0.9$.

Pretreatment	Dry	Water	NaCl
BET surface area (m^2/g)	1235	1409	1045
t-plot surface area (m^2/g)	1126	1380	1306
Micropore volume (cm^3/g) ¹	0.45	0.48	0.37
Mesopore volume (cm^3/g) ¹	0.07	0.09	0.06
Total pore volume (cm^3/g)	0.53	0.59	0.50

on a cell with better heat contact between electrode and heat flux sensor than in the (b) and (c) series, resulting in better sensitivity but similar values of f and ΔV_{att} . The (b) and (c) series were measured on two different electrodes.

Similar results found at concentrations below 0.1 M are not presented, because they are less reliable, for practical reasons. A typical set of measurements lasts about one week, including temperature equilibration, if no practical issues arise. In this time, saturated KCl solution leaks from the reference electrode at a few $\mu\text{L}/\text{hour}$, increasing the salt concentration in the cell by ≤ 0.1 M in two weeks. The saturated KCl salt bridge of the reference electrode is necessary for good stability of the electrode potential and to minimize the liquid junction potential, which is negligible only if the salt solution in the electrochemical cell is dilute compared to the saturated KCl solution in the salt bridge of the RE, as can be calculated via the Henderson equation for diffusion potentials [95]. The open circuit potential was in most cases +0.2 V versus the RE. It was higher in 1 M LaCl_3 , +0.3 V versus the RE, in part because of a higher liquid junction potential.

Table 3.4: Extended version of Table 3.1.

Salt	K [J/(Vs)]	Slope of ($\Delta U/\Delta Q$ vs. ΔV)	ΔV_{att} (V)	f	C_{cathodic} (F)	C_{anodic} (F)
0.1 M NaCl (a)	-71.1 ± 0.1	0.322 ± 0.003	-0.0784 ± 0.0010	0.119 ± 0.002	5.33 ± 0.05	4.81 ± 0.04
5 M NaCl (a)	-90.4 ± 0.3	0.378 ± 0.003	-0.1250 ± 0.0010	0.081 ± 0.002	6.69 ± 0.04	5.69 ± 0.03
1 M LiCl (b)	-177.6 ± 0.8	0.381 ± 0.003	-0.1248 ± 0.0010	0.079 ± 0.002	6.10 ± 0.05	5.02 ± 0.02
1 M NaCl (a)	-105.1 ± 0.8	0.340 ± 0.004	-0.0873 ± 0.0015	0.107 ± 0.003	6.47 ± 0.21	5.34 ± 0.02
1 M NaCl (b)	-182.9 ± 0.4	0.360 ± 0.004	-0.1034 ± 0.0013	0.093 ± 0.003	5.95 ± 0.07	4.99 ± 0.02
1 M NaCl (c)	-266.2 ± 0.9	0.376 ± 0.008	-0.1206 ± 0.0028	0.083 ± 0.005	6.15 ± 0.03	5.95 ± 0.06
1 M KCl (b)	-189.8 ± 0.6	0.348 ± 0.004	-0.1071 ± 0.0013	0.101 ± 0.003	5.92 ± 0.05	5.00 ± 0.02
1 M RbCl (b)	-191.2 ± 0.2	0.351 ± 0.005	-0.0950 ± 0.0016	0.099 ± 0.003	5.93 ± 0.05	5.08 ± 0.03
1 M CsCl (b)	-189.5 ± 0.8	0.337 ± 0.004	-0.0923 ± 0.0015	0.109 ± 0.003	6.08 ± 0.05	5.08 ± 0.02
1 M MgCl ₂ (b)	-379.0 ± 0.8	0.411 ± 0.002	-0.1219 ± 0.0006	0.059 ± 0.002	7.11 ± 0.04	5.27 ± 0.02
1 M CaCl ₂ (c)	-263.5 ± 0.8	0.398 ± 0.003	-0.1554 ± 0.0008	0.068 ± 0.002	6.95 ± 0.03	6.10 ± 0.03
1 M LaCl ₃ (b)	-371.9 ± 1.6	0.456 ± 0.004	-0.1479 ± 0.0014	0.029 ± 0.003	7.00 ± 0.05	6.08 ± 0.03
1 M LaCl ₃ (c)	-276.2 ± 0.8	0.456 ± 0.006	-0.1710 ± 0.0021	0.029 ± 0.004	7.44 ± 0.04	6.42 ± 0.04

Chapter 4

Capacitive Charging Rate Dependence of Heat from Porous Carbon in Aqueous Salt Solution

Abstract

Porous capacitive electrodes are applied in supercapacitors and capacitive deionization of aqueous salt solutions. In both cases, electric charge and ions are stored in the electrical double layer at the surface of the pores. In Chapter 3, we revealed that the equilibrium potential energy of the ions in the pores can be obtained from isothermal calorimetric measurements. On that basis, we now introduce a model for the time-dependent heat production at any charging or discharging rate. The model centers on a mathematical expression for the instantaneous internal energy of the double layer, which depends only on constant system parameters and the instantaneous electric potential drop across the double layer. Semiquantitative agreement is found with experiments on a porous carbon electrode in aqueous salt solution. The theory applies both in the case of abrupt application of a potential to the electrode, generating a maximum amount of Joule heat, and in cases where the potential is applied more slowly, even when charging becomes so slow that heat production is essentially reversible. These results not only provide fundamental insight into the electrical double layer of porous capacitive electrodes, but they are also a new way to describe and to predict the time-dependent generation of heat from such electrodes.

4.1 Introduction

Whereas the main function of electrodes is to enable electrochemical conversions or to store electric charge or ions, electrodes also produce heat. In batteries and supercapacitors, most of the heat is Joule heat, generated by the flow of current through resistive parts of the system. This type of heat is always exothermic, and it becomes larger as the device is (dis)charged at higher rate [25, 28, 96, 97]. Excessive heat can be damaging to batteries [98, 99] and supercapacitors [47, 48], and it may even cause safety hazards [100, 101]. In academic research, the (dis)charging rate of electrical energy storage devices can be decreased drastically, so that Joule heat production is suppressed and reversible heat becomes dominating [24, 51]. A key characteristic of reversible heat is that it has a different sign depending on the direction of the electric current. Moreover, measurements of the reversible heat give specific information on electrode processes. In the case of batteries, the reversible heat corresponds to $T\Delta S$, where T is the absolute temperature and ΔS is the entropy change, which can also be obtained from the temperature-dependence of the open circuit potential [51, 50, 102, 103, 104, 105]. In the case of porous capacitive electrodes, the reversible heat of (dis)charging the capacitor informs on changes in the state of the electrical double layer inside the pores. In this chapter, we focus on heat production by capacitive porous electrodes and its dependence on the (dis)charging rate.

Capacitive electrodes are usually based on microporous carbon and they have a great specific surface area, typically more than 1000 m^2 per gram of dry material. Such electrodes are used in the desalination of water via capacitive deionization [9, 13, 61] and the storage of electrical energy in supercapacitors [35, 37, 60]. Compared to nonporous electrodes, the (dis)charging of porous electrodes is relatively slow, limited by ionic transport through the porous network. Most transport occurs via mesopores (2-50 nm in width), whereas most storage of charge and ions occurs at the surface of micropores ($<2\text{ nm}$ in width) [10, 11, 30]. The electrical double layer extends throughout the porous network, rendering interfacial heat effects sufficiently strong that they can be measured using sensors that detect temperature [1, 28] or heat flux [24, 29].

The origin of the reversible heat produced by porous capacitive electrodes has been explained in different ways. Schiffer et al. [28] equated it to $T\Delta S$,

where ΔS is the entropy change due to changes in ionic concentrations when the dilute initial salt solution becomes confined inside the pores. Janssen et al. [1] demonstrated via experiments and classical thermodynamics how the reversible heat produced at constant temperature is related to the temperature-dependence of the equilibrium charge of the electrode. Janssen and Van Roij [31] ascribed the reversible heat to the entropic part of the change in grand potential energy of the system. D'Entremont and Pilon [33, 34] developed a physical model for the time-dependent production of irreversible and reversible heat from supercapacitor electrodes, on the basis of coupled electrical and thermal gradients, distinguishing different contributions to the reversible heat, from ionic diffusion, steric repulsion, and changes in the mixing entropy and activity coefficients of the ions. Glatzel et al. [32] used density functional theory and molecular dynamics calculations to predict the reversible heat production depending on several system parameters, including the sizes and concentrations of the ions.

General trends predicted by Glatzel et al. [32] were supported by our calorimetric experiments in Chapter 3. We used microporous carbon electrodes to measure the heat of double layer formation in aqueous solutions of different types of ions under isothermal conditions. However, electrode potentials were applied abruptly, and the reversible heat was calculated from the difference between the heats of charging and discharging, processes that were carried out far from equilibrium. It was assumed that the Joule heat was precisely the same during charging and discharging, but earlier evidence in support of this assumption was not necessarily conclusive [1]. Moreover, no attempt was made to slow down the rate of (dis)charging, to cancel the Joule heat, so that the reversible heat might be determined directly as the sole contribution to the measured heat.

Our own interpretation of the heat from porous capacitive electrodes is to equate it to the difference between the change in the internal energy of the electrode and the electrical work performed on the electrode (Chapter 3). In that framework, reversible heat is produced when the internal energy not only consists of the electrical energy of the double layer capacitor but also includes other contributions, such as the attraction of ions to the electrode surface and the electrical energy of the ionic solution inside the pores. In chapter, the

model from Chapter 3 which described the total heat generated after abrupt application of an external potential to the electrode is extended to describe the time-dependent heat generation at any (dis)charging rate. To compare the theory to the measurements, no fitting is required, except for an initial determination of constant system parameters from experiments in which the applied potential is set abruptly. In the Experimental section, our method to measure the heat of electrical double layer formation of porous capacitive electrodes is summarized. The assumptions of the model are discussed in the Theory section, and full analytical expressions are derived in appendices 4.6-4.9. In the Results and Discussion section, results of the measurements are presented and compared one-to-one to predictions of the model.

4.2 Experimental

Experiments were conducted using the glass electrochemical cell described in Chapter 2. The setup consisted of three electrodes: a microporous carbon working electrode (WE), an Ag/AgCl/saturated KCl reference electrode (RE, Radiometer REF201), and a counter electrode (CE). A PARSTAT PMC-1000 potentiostat was used to control the potential of the WE with respect to the RE and to measure the resulting current that flowed between WE and CE. The WE and CE were made of porous carbon disks, of the same material as used in Refs. [1, 14]. As in Chapter 3, the disks had a diameter of 21 mm, a thickness of ~ 0.25 mm, a mass of 63 mg, a specific surface area of $1400 \text{ m}^2/\text{g}$, a porosity of 60 %, and an average pore width of ~ 0.9 nm.

The heat generated at the WE was measured using a heat flux sensor (HFS, gSKIN[®] XP 26 9C, greenTEG AG, Switzerland). The resulting voltage was measured using a Keithley 2182A Nanovoltmeter. The glass cell was submerged in water in a box that was thermostated at 22°C by a Julabo F25 refrigerated/heating circulator. The cell was filled with a degassed solution of 1 M NaCl (Merck Emsure[®], for analysis), in water (Milli-Q, neutral pH).

Before polarization was started, the temperature of the system was left to stabilize for two days. During this time, the open circuit potential (V_{OCP}) was measured, stabilizing at a potential $V_{\text{OCP}} = 0.2 \text{ V}$ vs RE. Then, a potential of $\Delta V = 0 \text{ V}$ vs V_{OCP} was applied for an hour. Charging was initiated by

changing the potential linearly in time until a final potential ΔV in the range from -0.5 to $+0.5$ V vs V_{OCP} was reached in a time τ , which was varied between 0 and 2000 s. After 2 hours, the applied potential was changed back to $\Delta V = 0$ V (0.2 V vs RE), also linearly in a time τ , to discharge the system. Then, the applied potential of $\Delta V = 0$ V was kept stable for 2 hours to allow the absolute current to become minimal (≤ 20 μA). For each polarization rate, the charge-discharge cycle was measured at least twice, leading to practically the same results.

The HFS was calibrated via the method described in Chapter 2 and Chapter 3. In essence, the integral signal of the sensor for a full charge-discharge cycle was scaled to the net electrical work that had been performed on the system during the cycle. The same calibration constant that was determined to convert integral HFS signal in Vs into energy in J was also used to convert instantaneous heat signal in μV into heat production rate in mW.

4.3 Theory

In this section, theory is presented to describe how the gradual buildup of the applied potential affects the time-dependent electric current and heat production. The studied system consists of an electrical double layer capacitor in an isothermal environment. The system is approximated by a resistor of resistance R connected in series to a capacitor of capacitance C . Although electrically, the capacitance describes the amount of stored charge as it would for any capacitor, its internal energy is different from that of a simple capacitor. The energy is also affected by interaction of the ions with the electrode surface and with the electric potential inside the pores, both of which affect the heat production. The general foundations of the model are presented in this section, whereas full expressions for the time-dependent current and heat production rate are derived in Sections 4.6-4.9 (appendices 1-4).

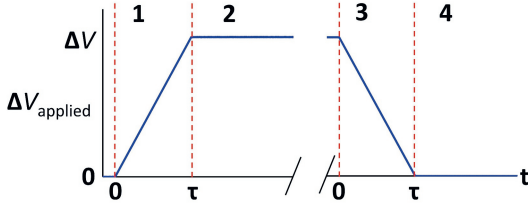


Figure 4.1: Time dependence of the applied potential in the theory and the experiments. Charging starts with changing the potential from 0 V to ΔV in a time τ . Discharging starts by bringing the potential back to zero in a time τ . Periods 1-4 are indicated.

4.3.1 Time-dependent current

The electric current $I(t)$ at time t is calculated from the resistance R and the voltage $\Delta V_R(t)$ across the resistor, according to Ohm's law:

$$I(t) = \Delta V_R(t)/R. \quad (4.1)$$

The voltage drop across the resistor is time-dependent for two reasons: due to time-dependence of the applied potential and time-dependence of the distribution of the applied potential over resistor and capacitor. Concerning the time-dependence of the applied potential, four time periods are distinguished in our theory and experiments, see Fig. 4.1. In period 1, the applied potential $\Delta V_{\text{applied}}$ is zero at an initial time $t=0$ s, and a time τ is taken to vary the potential linearly until its final value ΔV is reached:

$$\text{Period 1: } \Delta V_{\text{applied}}(t) = \frac{t}{\tau} \Delta V, \quad 0 \leq t \leq \tau. \quad (4.2)$$

In period 2, the applied potential is kept constant, and charging continues until current and heat production have become negligible:

$$\text{Period 2: } \Delta V_{\text{applied}}(t) = \Delta V, \quad t \geq \tau. \quad (4.3)$$

In period 3, discharging begins by resetting the time to $t=0$ s. The applied potential now starts at a value ΔV , and this is linearly brought back to zero

in a time τ :

$$\text{Period 3: } \Delta V_{\text{applied}}(t) = \Delta V \left(1 - \frac{t}{\tau}\right), \quad 0 \leq t \leq \tau. \quad (4.4)$$

Finally, in period 4, the applied potential remains zero until current and heat production have become negligible:

$$\text{Period 4: } \Delta V_{\text{applied}}(t) = 0 \text{ V}, \quad t \geq \tau. \quad (4.5)$$

The change in applied potential falls only partly across the resistor. The remaining part falls across the capacitor and is determined by the capacitance and the total charge $\Delta Q(t)$ on the capacitor, compared to the situation at the initially applied potential of $\Delta V = 0 \text{ V}$:

$$\Delta V_C(t) = \Delta Q(t)/C. \quad (4.6)$$

For the charging process, the initial charge is zero, and $\Delta Q(t)$ is given by

$$\Delta Q_{\text{ch}}(t) = \int_0^t I(t') dt'. \quad (4.7)$$

For the discharging process, an initial charge $C\Delta V$ is present and it is gradually removed (the current is now negative):

$$\Delta Q_{\text{dis}}(t) = C\Delta V + \int_0^t I(t') dt'. \quad (4.8)$$

An infinitesimal change dV_{applied} in the applied potential is distributed over the resistor and the capacitor:

$$dV_{\text{applied}}(t) = dV_R(t) + dV_C(t). \quad (4.9)$$

In line with Eqs. (4.5) and (4.6), $dV_R(t)$ and $dV_C(t)$ are given by the following:

$$dV_R(t) = R dI(t), \quad (4.10)$$

$$dV_C(t) = I(t) dt / C. \quad (4.11)$$

Equations (4.1)-(4.11) are sufficient to calculate the time-dependent current,

knowing that it is zero at $t = 0$ s in the case of gradual change of the applied potential, see Sections 4.6-4.9 (appendices 1-4).

4.3.2 Time-dependent heat production

The integral heat having been produced at time t due to (dis)charging is calculated from the electrical work w performed on the system and the change in internal energy in the case of gradual change of the applied potential, ΔU , using the first law of thermodynamics:

$$q(t) = \Delta U(t) - w(t). \quad (4.12)$$

Pressure-volume work is neglected. Moreover, the heat effects are so small that temperature changes remain less than 0.1 °C (see Chapter 2), so that the system is assumed to have a constant temperature. Since the studied capacitor includes an electrical double layer, its internal energy differs from that of a simpler capacitor with a dielectric material between two parallel plates. In an electrical double layer capacitor, the ions have an electrical potential energy that depends on the local electric potential inside the pores. Moreover, the ions interact with the electrode surface. Consequently, upon charging or discharging of the capacitor, the change in internal energy can be greater or smaller than the amount of electrical work performed on the system. The difference between the energy change and the work is the reversible heat that must be exchanged to keep the system at constant temperature. In addition, not only reversible but also irreversible heat is produced, by electric current flowing through the resistor. To produce this ‘Joule heat’, more electrical work must be performed on the system than when it is (dis)charged reversibly. This part of the heat decreases to zero in the limit of infinitely slow change of the applied potential, when the capacitor is in equilibrium at each moment of the (dis)charging process.

To describe the time-dependent internal energy $\Delta U(t)$ of the capacitor, we extend the theoretical approach that we introduced in Chapter 3:

$$\Delta U(t) = \left(\frac{1}{2} - \frac{3}{2}f \right) C(\Delta V_C(t))^2 + C\Delta V_C(t)\Delta V_{\text{att}}. \quad (4.13)$$

Here, $fV_C(t)$ is the average electric potential of the ions in the pores, and the term with constant ΔV_{att} represents the potential energy of the ions due to their attraction to the surface of the electrode. A key difference with Chapter 3 is that Eq. (4.13) gives the instantaneous internal energy depending on the instantaneous potential drop across the capacitor, $\Delta V_C(t)$, whereas in Chapter 3, only the equilibrium situation was considered, when $\Delta V_C(t) = \Delta V$ and $\Delta V_R(t) = 0$. The amount of heat produced at time t can now be calculated from Eqs. (4.12) and (4.13) and from the electrical work w that has been performed on the system at time t , which is given by:

$$w(t) = \int_0^t V_{\text{applied}}(t')I(t')dt'. \quad (4.14)$$

An expression for the heat production rate is found by differentiation of the expressions for $\Delta U(t)$ and $w(t)$:

$$\frac{dq(t)}{dt} = \frac{d\Delta U(t)}{dt} - \frac{dw(t)}{dt}. \quad (4.15)$$

The analytical expressions for the time-dependent current, energy, work, integral heat, and heat production rate are different in periods 1-4, see Sections 4.6-4.9 (appendices 1-4).

4.4 Results and discussion

4.4.1 Determination of system constants

To predict the time-dependent current and heat production via the model presented in the Theory section, four system constants need to be known: the resistance R , the capacitance C , and the parameters f and ΔV_{att} that feature in Eq. (4.13) for the internal energy.

A resistance R of $11.0 \pm 0.6 \Omega$ was calculated from the initial current upon abrupt application of a potential ΔV to the electrode, using Ohm's law (Eq. 4.1). Capacitances of $C = 5.35 \pm 0.03 \text{ F}$ in the anodic region and $6.29 \pm 0.11 \text{ F}$ in the cathodic region were calculated from the integral charge after prolonged polarization at an applied potential ΔV (Eq. 4.6). The values of R and C together indicate that the RC time was 59 s during anodic (dis)charging and 70 s during

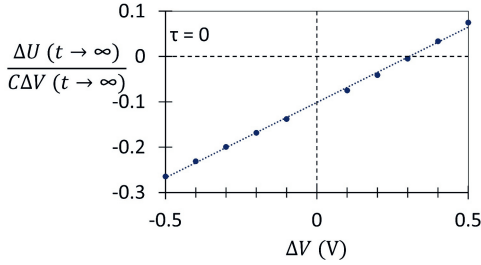


Figure 4.2: Internal energy change per electrode charge measured upon abrupt polarization, plotted versus the applied potential. As introduced in Chapter 3, such a plot gives the system parameters that describe the potential energy of the ions in the pores. Using Eq. (4.13) with $\Delta V_C(t) = \Delta V$, $\Delta V_{\text{att}} = (-0.101 \pm 0.005) \text{ V}$ and $[-\frac{1}{2} - \frac{3}{2}f] = 0.333 \pm 0.002$ were obtained, leading to an f of 0.112.

cathodic (dis)charging.

The parameters f and ΔV_{att} were determined by measuring changes in the internal energy ΔU after prolonged charging at applied potential ΔV , see Fig. 4.2. As in Chapter 3, the changes in internal energy were determined using the first law of thermodynamics [Eq. (4.12)], from the integral measured heat and the integral electrical work performed on the system, calculated via Eq. (4.14) from the time-dependent current at constant applied potential.

4.4.2 Abrupt polarization ($\tau = 0 \text{ s}$)

Figure 4.3 shows theoretical predictions and experimental results for the case of $\tau = 0 \text{ s}$. A potential of $\Delta V = 0.5 \text{ V}$ was applied abruptly to the electrode, leading to a sudden current peak, which then exponentially decayed to zero. Except for the sign of the current, the current transients were practically the same during charging and discharging. The theoretical current curves largely match the experiments, although in the measured curves, the time constant of exponential decay appears to increase gradually. This indicates that our theoretical description of the system in terms of a single RC time is oversimplified. The current transients would be better described by a distribution of relaxation times, consequence of the polydispersity of the pore dimensions and inhomogeneity of the porous network [106, 107, 108, 109]. In theory, it has been found by Lian et al. [30] that monodisperse micropores that are

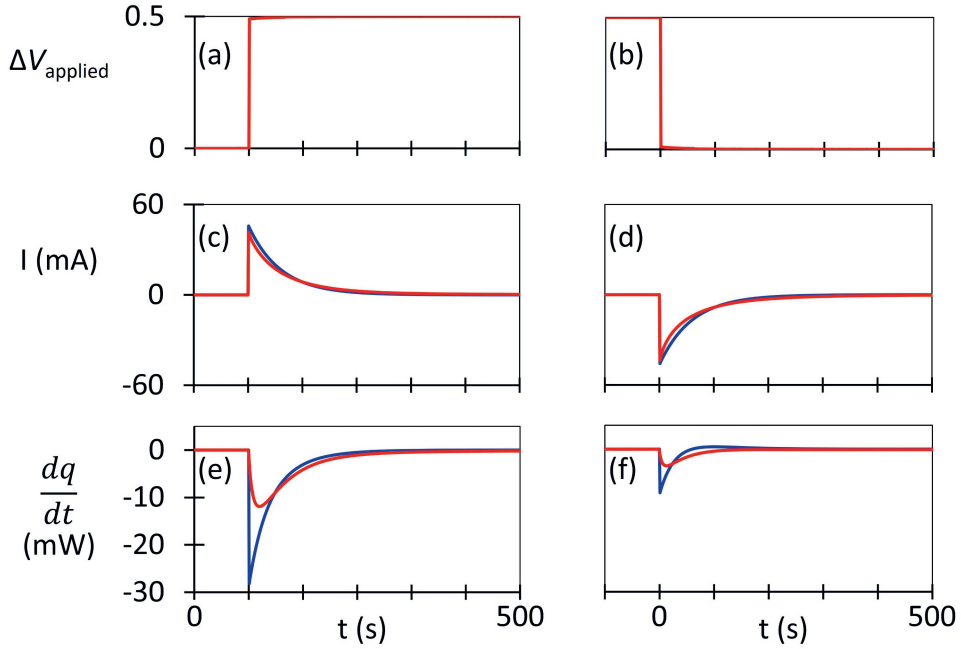


Figure 4.3: Theoretical (blue) and experimental (red) time-dependence of electric current and heat production rate in the case of abrupt changes of the potential applied to a capacitive porous carbon electrode in 1 M NaCl ($\tau = 0$ s, charging potential $\Delta V = 0.5$ V). Time dependence of (a,b) the applied potential, (c,d) the electric current, and (e,f) the heat production rate (an instrumental offset of 0.86 mW was subtracted). The theoretical time-dependent curves for charging were calculated using (c) Eq. (4.32) for the current and (e) Eq. (4.45) for the heat production rate, while the theoretical curves for discharging were calculated using (d) Eq. (4.61) and (f) Eq. (4.70). The values for f and ΔV_{att} were those found in Fig. 4.2.

equally accessible to the ions via mesopores lead initially to mono-exponential decay due to ionic migration, followed by slower mono-exponential decay due to ionic diffusion.

Heat production was exothermic (negative) both during charging and discharging. However, the heat of discharging was much smaller than the heat of charging. This was because the reversible heat was negative during charging and positive during discharging. The theoretical heat curves largely reproduce the measurements, although the experimental heat curves were not as sharply peaked. Heat produced by the electrode had to flow through a glass barrier before reaching the heat flux sensor (Chapter 2), resulting in a slight delay between heat production and detection.

Results as in Fig. 4.3 but for other applied potentials ΔV are provided in Section 4.10.

4.4.3 Intermediate charging rate ($\tau = 100$ s)

Figure 4.4 shows measurements and theory for the case that a time $\tau = 100$ s is taken to apply $\Delta V = 0.5$ V. Note that 100 s has the same order of magnitude as the RC time. In theory and experiment, the current became larger while the applied potential changed, both during charging and discharging. At $t = 100$ s, the applied potential stopped changing, and the current started to decay exponentially toward zero, with a characteristic time constant equal to RC . The current did not increase as rapidly in experiment as in theory, which probably is again because the description in terms of a single RC time is oversimplified.

The time-dependent heat production was now even more different between charging and discharging than in the case of abrupt polarization. During charging, the heat production rate mirrored the current, first increasing more or less linearly and then decaying exponentially. The measured heat production was lower than in theory, probably because the lower than theoretical electric currents led to lower than theoretical production of Joule heat. During discharging, theory predicted that the produced heat would first be positive (endothermic), indicating that the reversible heat was larger than the Joule heat, but that before $t = 100$ s, heat production would become negative, indicating that Joule heat had become dominating. After $t = 100$ s, heat pro-

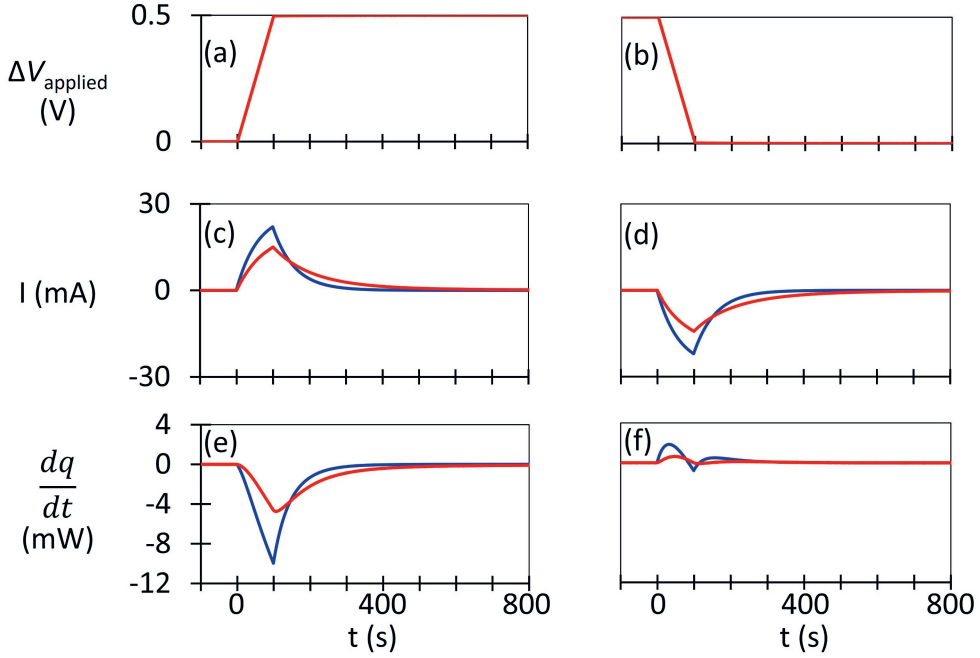


Figure 4.4: As in Fig. 4.3, but now for gradual change of the applied potential, with $\tau = 100$ s ($\Delta V = 0.5$ V, same f and ΔV_{att} as in Fig. 4.2). In (e) and (f), an instrumental offset of 0.74 mW was subtracted. The theoretical time-dependent curves for charging were calculated using (c) Eqs. (4.17) and (4.31) for the current and (e) Eqs. (4.29) and (4.44) for the heat production rate, while the theoretical curves for discharging were calculated using (d) Eqs. (4.47) and (4.60) and (f) Eqs. (4.59) and (4.69).

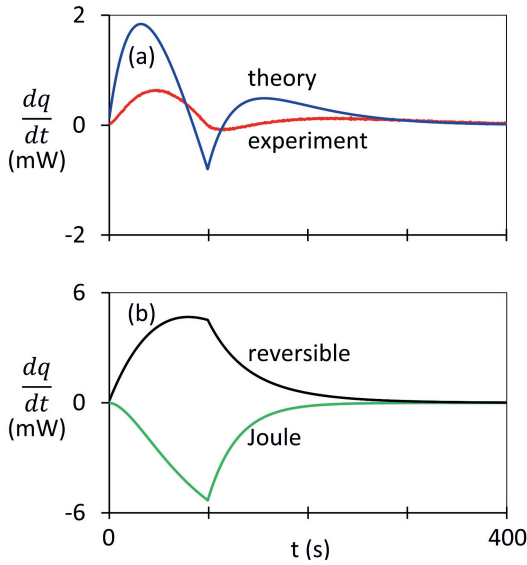


Figure 4.5: (a) Experimental (red) and theoretical (blue) total heat production rate for $\tau = 100$ s and $\Delta V = 0.5$ V, as in Fig. 4.4(f). (b) Separate contributions of reversible heat (black) and irreversible heat (green). The curve for the irreversible heat production rate was calculated by filling in $f = 0$ and $\Delta V_{\text{att}} = 0$ V into Eqs. (4.59) and (4.69). The curve for the reversible heat production rate was found by subtracting the irreversible contribution from the total heat production rate, calculated using the same equations but with the values of f and ΔV_{att} found in Fig. 4.2.

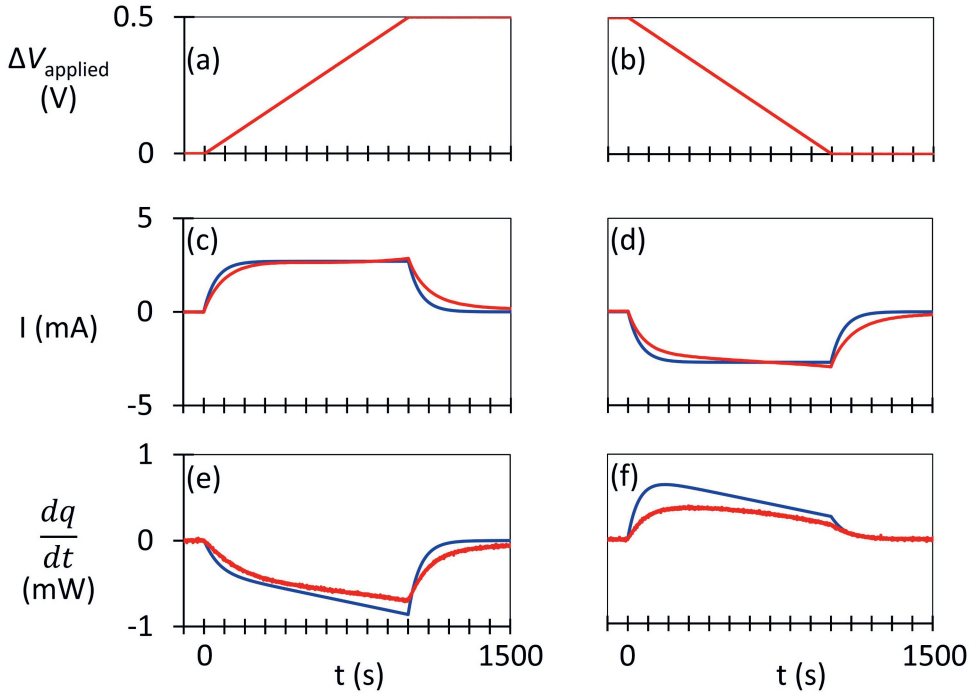


Figure 4.6: As in Fig. 4.3, but now for gradual change of the applied potential, with $\tau = 1000$ s ($\Delta V = 0.5$ V, same f and ΔV_{att} as in Fig. 4.2). In (e) and (f), an instrumental offset of 0.73 mW was subtracted. The theoretical time-dependent curves for charging were calculated using (c) Eqs. (4.17) and (4.31) for the current and (e) Eqs. (4.29) and (4.44) for the heat production rate, while the theoretical curves for discharging were calculated using (d) Eqs. (4.47) and (4.60) and (f) Eqs. (4.59) and (4.69).

duction would again decay to zero. Figure 4.5 shows a close-up of Fig. 4.4(f) as well as the predicted time-dependent contributions of reversible and irreversible heat. These two contributions are relatively large, but they partly cancel each other out. In experiment, the predicted effects are smoothed out by the delay between heat production and detection.

Results as in Fig. 4.4 for $\tau = 100$ s, but for other applied potentials ΔV , are provided in Section 4.10.

4.4.4 Nearly reversible charging ($\tau=1000$ s)

Figure 4.6 shows measurements and theory for the case that a time $\tau=1000$ s is taken to apply $\Delta V=0.5$ V ($\tau \sim 15RC$). After a time of about $2RC$, the current stayed approximately constant until $t=1000$ s, after which it exponentially decayed toward zero. The theoretical current transients match the measurements fairly well. From Eq. (4.17), it can be deduced that in the plateau, the current is approximately equal to $C\Delta V/\tau$.

The heat production transients for $\tau=1000$ s started to approach a fully reversible situation. Irreversible heat production was so small that during discharging, the heat production remained positive from beginning to end. Moreover the total heat production during charging was now of similar magnitude but opposite in sign to that during discharging. After $t=1000$ s, the heat production again exponentially decayed toward zero.

Results as in Fig. 4.6 for $\tau=1000$ s, but for other applied potentials, are provided in Section 4.10.

4.4.5 Total heat of (dis)charging as a function of polarization rate

In Fig. 4.7, the total heat of charging (q_{ch}) and the total heat of discharging (q_{dis}) are plotted against the applied potential buildup time τ at four different charging potentials. At all potentials, both the charging and discharging heats became more positive with increasing polarization time τ , and the total heat $q_{\text{ch}} + q_{\text{dis}}$ of a full charge-discharge cycle evolved toward zero. This indicates that q_{ch} and q_{dis} progressed toward the same absolute value, but with opposite sign. In other words, the reversible heat became dominating. However, even at the slowest charging rate ($\tau=2000$ s), the heat was not yet fully reversible.

The charging and discharging heats depended on the charging potential. At $\Delta V=0.5$ V and $\Delta V=0.3$ V, the charging heat was more negative than the discharging heat, but at $\Delta V=-0.3$ V, it was the other way around. This indicates that the reversible heat of charging was negative at $\Delta V=0.5$ V and $\Delta V=0.3$ V but positive at $\Delta V=-0.3$ V. At $\Delta V=-0.5$ V, the heats of charging and discharging were almost the same, indicating that the reversible heat was close to zero. Although the theoretical curves do not describe the measurements quantitatively, the sign reversal of the reversible heat is reproduced,

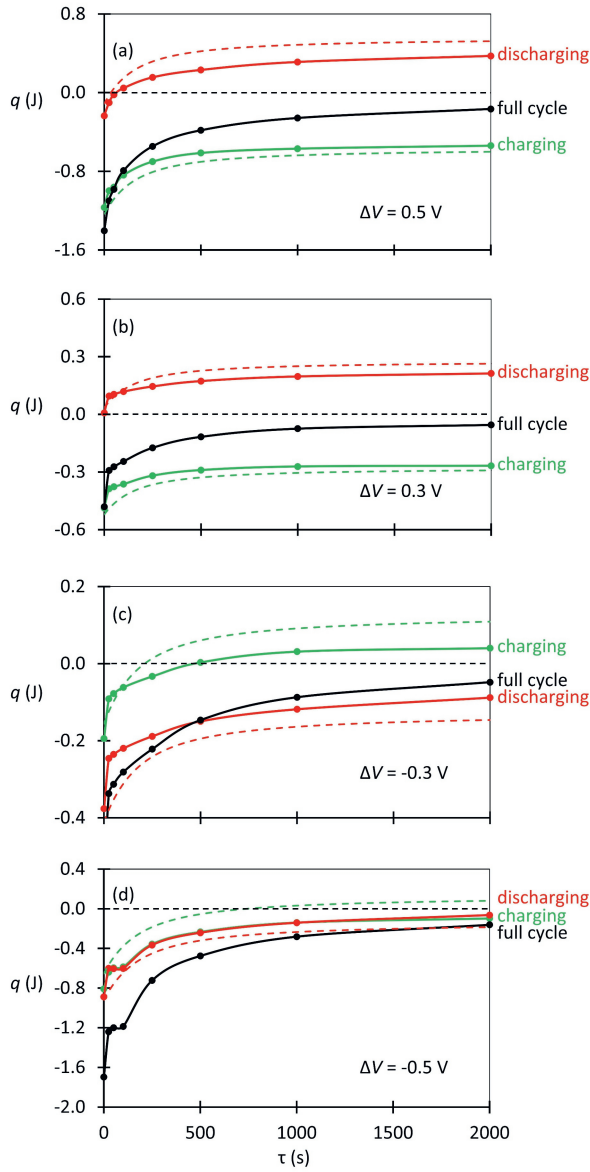


Figure 4.7: Heats of charging and discharging versus time τ taken to apply or to remove potentials ΔV of (a) $+0.5$ V, (b) $+0.3$ V, (c) -0.3 V, and (d) -0.5 V. The total heats measured for full charge-discharge cycles are indicated as well. The dashed curves were calculated by filling in the values of f and ΔV_{att} found in Fig. 4.2 into Eqs. (4.42) and (4.71).

as well as the trends in the magnitude of the reversible and Joule heats.

In the measured and calculated curves in Fig. 4.7, the difference between the heats of charging and discharging is independent of the charging rate. In Chapter 3 and Ref. [1], the difference between q_{ch} and q_{dis} upon abrupt polarization was equated to twice the reversible heat, assuming that the Joule heat was identical upon charging and discharging. This assumption is supported by the model in this chapter. The same expression for the absolute reversible heat $|q_{\text{rev}}|$ is found in the limit of infinitely slow charging [Eq. (4.28)] and infinitely slow discharging [Eq. (4.58)]. Moreover, the total Joule heat $q_{\text{irr,ch}}$ upon charging [Eq. (4.43)] is found to be equal to the total Joule heat $q_{\text{irr,dis}}$ upon discharging [Eq. (4.73)], irrespective of the time τ that is taken to apply the final potential ΔV to the electrode. The combination of these theoretical results confirms that the difference between the heat of charging, $q_{\text{ch}} = q_{\text{irr,ch}} + q_{\text{rev}}$, and the heat of discharging, $q_{\text{dis}} = q_{\text{irr,dis}} - q_{\text{rev}}$, is indeed equal to $2q_{\text{rev}}$. This supports the validity of the analysis in Chapter 3 of heats of double layer formation from measurements where the electric potential was applied abruptly. This also has an important practical implication, since measurements in which the potential is applied abruptly are shorter and lead to stronger signals than if the charging would have to be extremely slow to obtain valid thermodynamic information about the electrical double layer.

4.5 Conclusions

Time-dependent and integral heat production were measured for a capacitive porous carbon electrode in 1 M aqueous NaCl. Different charging rates were realized by changing the time taken to build up the applied potential linearly to its final value ΔV . The reversible and irreversible heat effects were accounted for by a model that assumes that the instantaneous internal energy of the electrode depends on the instantaneous potential drop across the electrical double layer. The system-dependent parameters of the model are four constants: the resistance, the capacitance, and f and ΔV_{att} , which describe the potential energy of the ions in the pores. When the electrode is being (dis)charged, the instantaneous heat production corresponds to the difference between the rate at which the internal energy changes and the rate at which

electrical work is performed on the electrode. The analytical formulas derived on this basis are in semiquantitative agreement with the measured heat signals, which supports our theoretical approach. In the future, the model might be expanded to take into account a distribution of RC time constants or a gradual increase in temperature of the system, as occurs during the relatively rapid current or voltage cycling of a supercapacitor. In that case, it will be necessary to consider that the electrode is not fully charged or discharged during each half cycle. In this way, the thermodynamic approach presented here not only gives insight into the electrical double layer of porous capacitive electrodes, but it may also help to understand and to predict heat production by supercapacitors.

4.6 Appendix 1: Formulas for period 1 (charging, $0 \leq t \leq \tau$)

Combination of Eqs. (4.9-4.11) with Eq. (4.2) for the time-dependent applied potential in period 1 gives:

$$\frac{\Delta V}{\tau} dt = \frac{I(t)}{C} dt + R dI(t). \quad (4.16)$$

Integration of Eq. (4.16) gives the following charging current in period 1:

$$I_{\text{ch},1}(t) = \frac{C\Delta V}{\tau} \left[1 - \exp\left(-\frac{t}{RC}\right) \right], \quad 0 < t \leq \tau. \quad (4.17)$$

The current is zero at $t=0$ s and increases until $t = \tau$, where it is

$$I_{\text{ch},1}(\tau) = \frac{C\Delta V}{\tau} \left[1 - \exp\left(-\frac{\tau}{RC}\right) \right]. \quad (4.18)$$

In the limit of abrupt polarization, this coincides with Eq. (4.1), when ΔV is applied abruptly:

$$\lim_{\tau \rightarrow 0} I_{\text{ch},1}(\tau) = \frac{\Delta V}{R}. \quad (4.19)$$

By integration of the current [Eq. (4.17)], charge $\Delta Q_{\text{ch},1}$ at time t is found:

$$\Delta Q_{\text{ch},1}(t) = \frac{C\Delta V}{\tau} \left[t + RC \left\{ \exp\left(-\frac{t}{RC}\right) - 1 \right\} \right]. \quad (4.20)$$

At time τ , this becomes

$$\Delta Q_{\text{ch},1}(\tau) = C\Delta V \left[1 + \frac{RC}{\tau} \left\{ \exp\left(-\frac{\tau}{RC}\right) - 1 \right\} \right]. \quad (4.21)$$

As expected, the value is zero in the limit of very short polarization.

Via Eq. (4.14), using Eqs. (4.2) and (4.17), the integral work that has been performed on the system at time t is

$$\begin{aligned} w_{\text{ch},1}(t) = & \frac{C(\Delta V)^2}{\tau^2} \left[\frac{t^2}{2} + tRC \exp\left(-\frac{t}{RC}\right) \right. \\ & \left. + (RC)^2 \exp\left(-\frac{t}{RC}\right) - (RC)^2 \right]. \end{aligned} \quad (4.22)$$

At time τ , Eq. (4.22) becomes

$$w_{\text{ch},1}(\tau) = C(\Delta V)^2 \left[\frac{1}{2} + \frac{RC}{\tau} \exp\left(-\frac{\tau}{RC}\right) + \frac{(RC)^2}{\tau^2} \exp\left(-\frac{\tau}{RC}\right) - 1 \right]. \quad (4.23)$$

In the limit of slow change of the applied potential, corresponding to high τ/RC (full charging in period 1), the total work performed on the system is

$$\lim_{\tau \rightarrow \infty} w_{\text{ch},1}(\tau) = \frac{1}{2} C(\Delta V)^2. \quad (4.24)$$

This is the reversible work. In the limit of $\tau \rightarrow 0$, $w_{\text{ch},1}$ goes to zero, since there is no time to deliver work on the system.

To find the time-dependent heat, according to Eq. (4.12), the time-dependent work [Eq. (4.22)] needs to be subtracted from the time-dependent energy of the system. An expression for the time-dependent energy is found by filling in $\Delta V_C(t)$ from Eq. (4.6) and $\Delta Q(t)$ from Eq. (4.20) into Eq. (4.13):

$$\begin{aligned} \Delta U_{\text{ch},1}(t) = & \frac{C(\Delta V)^2}{\tau^2} \left[\frac{1}{2} - \frac{3}{2}f \right] \left(t + RC \left\{ \exp\left(-\frac{t}{RC}\right) - 1 \right\} \right)^2 \\ & + C\Delta V_{\text{att}} \frac{\Delta V}{\tau} \left[t + RC \left\{ \exp\left(-\frac{t}{RC}\right) - 1 \right\} \right]. \end{aligned} \quad (4.25)$$

At time τ this is equal to

$$\begin{aligned} \Delta U_{\text{ch},1}(\tau) = C(\Delta V)^2 \left[\frac{1}{2} - \frac{3}{2}f \right] \left(1 + \frac{RC}{\tau} \left\{ \exp\left(-\frac{\tau}{RC}\right) - 1 \right\} \right)^2 \\ + C\Delta V_{\text{att}}\Delta V \left[1 + \frac{RC}{\tau} \left\{ \exp\left(-\frac{\tau}{RC}\right) - 1 \right\} \right]. \end{aligned} \quad (4.26)$$

In the limit of abrupt polarization ($\tau \rightarrow 0$), $\Delta U(\tau)$ goes to zero, whereas in the limit of slow polarization ($\tau \rightarrow \infty$), the change in internal energy is given by Eq. (4.13) with $\Delta V_C(t) = \Delta V$.

Using Eqs. (4.12), (4.23), and (4.26), an expression is found for the integral heat at time τ :

$$\begin{aligned} q_{\text{ch},1}(\tau) = \frac{C(\Delta V)^2}{2} \left[-3f - 6f\frac{RC}{\tau} \exp\left(-\frac{\tau}{RC}\right) - [2 - 6f]\frac{RC}{\tau} \right. \\ + [1 - 3f]\frac{R^2C^2}{\tau^2} \exp\left(-\frac{2\tau}{RC}\right) - (4 - 6f)\frac{R^2C^2}{\tau^2} \exp\left(-\frac{\tau}{RC}\right) \\ \left. + (3 - 3f)\frac{R^2C^2}{\tau^2} \right] + C\Delta V_{\text{att}}\Delta V \left[1 + \frac{RC}{\tau} \exp\left(-\frac{\tau}{RC}\right) - \frac{RC}{\tau} \right]. \end{aligned} \quad (4.27)$$

This is zero in the limit of abrupt polarization, whereas in the limit of slow polarization, an expression for the reversible heat is found:

$$\lim_{\tau \rightarrow \infty} q_{\text{ch}}(\tau) = -\frac{3}{2}fC(\Delta V)^2 + C\Delta V\Delta V_{\text{att}} = q_{\text{rev}}. \quad (4.28)$$

This result agrees with the expression for the reversible heat found in Chapter 3, where in contrast to here, it was assumed that the Joule heat is precisely the same upon charging and discharging. Note that $q_{\text{rev}} = 0$ J when f and ΔV_{att} are zero, e.g., in the case that the system consists of a simple capacitor.

Finally, by differentiating the expressions for the time-dependent work (Eq. 4.22) and energy (Eq. 4.25) with respect to time, an expression for the

heat production rate in period 1 is found:

$$\begin{aligned} \frac{dq_{\text{ch},1}(t)}{dt} = & \frac{C(\Delta V)^2}{\tau^2} \left[-3ft + (2 - 6f)RC \exp\left(-\frac{t}{RC}\right) - [1 - 3f]RC \right. \\ & \left. + 3ft \exp\left(-\frac{t}{RC}\right) - [1 - 3f]RC \exp\left(-\frac{2t}{RC}\right) \right] \\ & + C\Delta V_{\text{att}} \frac{\Delta V}{\tau} \left[1 - \exp\left(-\frac{t}{RC}\right) \right]. \end{aligned} \quad (4.29)$$

4.7 Appendix 2: Formulas for period 2 (charging, $t \geq \tau$)

Period 2 starts at time τ , when the charging potential ΔV is held constant [Eq. (4.3)]. Equations (4.9-4.11) indicate that the time-dependent changes in the current are given by

$$dI(t) = \frac{dV_C(t)}{R} = -\frac{dV_C(t)}{R} = -\frac{I(t)dt}{RC}. \quad (4.30)$$

This leads to exponential decay of the current:

$$I_{\text{ch},2}(t) = I_{\text{ch},1}(\tau) \exp\left[-\frac{t - \tau}{RC}\right]. \quad (4.31)$$

where $I_{\text{ch},1}(\tau)$ is given by Eq. (4.18). In the limit of $\tau=0$, this becomes

$$\lim_{\tau \rightarrow 0} I_{\text{ch},2}(t) = \frac{\Delta V}{R} \exp\left[-\frac{t}{RC}\right]. \quad (4.32)$$

Integration of $I_{\text{ch},2}(t)$ from Eq. (4.31) gives the amount of charge in period 2 after infinitely long charging:

$$\Delta Q_{\text{ch},2}(t \rightarrow \infty) = C\Delta V \frac{RC}{\tau} \left[1 - \exp\left(-\frac{\tau}{RC}\right) \right]. \quad (4.33)$$

In the limit of abrupt polarization, this becomes

$$\lim_{\tau \rightarrow 0} \Delta Q_{\text{ch},2}(t) = C\Delta V \left[1 - \exp\left(-\frac{t}{RC}\right) \right]. \quad (4.34)$$

After infinitely long charging, the sum of the charges in period 1 [Eq. (4.21)] and period 2 [Eq. (4.33)] is as expected from the capacitance of the electrode:

$$\Delta Q_{\text{ch}}(t \rightarrow \infty) = \Delta Q_{\text{ch},1}(\tau) + \Delta Q_{\text{ch},2}(t \rightarrow \infty) = C\Delta V. \quad (4.35)$$

The time-dependent work (Eq. 4.14) in period 2 is found by filling in Eqs. (4.3) and (4.31) into Eq. (4.14):

$$w_{\text{ch},2}(t) = C(\Delta V)^2 \frac{RC}{\tau} \left[1 - \exp\left(-\frac{\tau}{RC}\right) \right] \left\{ 1 - \exp\left[-\frac{t-\tau}{RC}\right] \right\}. \quad (4.36)$$

In the limit of abrupt polarization, this becomes

$$\lim_{\tau \rightarrow 0} w_{\text{ch},2}(t) = C(\Delta V)^2 \left[1 - \exp\left(-\frac{t}{RC}\right) \right]. \quad (4.37)$$

The total work in period 2 in the limit of long polarization is given by

$$w_{\text{ch},2}(t \rightarrow \infty) = C(\Delta V)^2 \frac{RC}{\tau} \left[1 - \exp\left(-\frac{\tau}{RC}\right) \right]. \quad (4.38)$$

This is $C\Delta V^2$ in the limit of abrupt polarization. The total energy change in period 2 is the difference between the eventual energy change [Eq. (4.13) with $\Delta V_C(t) = \Delta V$] and the energy change in period 1 [Eq. (4.26)]:

$$\begin{aligned} \Delta U_{\text{ch},2}(t \rightarrow \infty) = C(\Delta V)^2 [1 - 3] & \left[-\frac{RC}{\tau} \exp\left(-\frac{\tau}{RC}\right) \right. \\ & - \frac{R^2 C^2}{2\tau^2} \exp\left(-\frac{2\tau}{RC}\right) + \frac{R^2 C^2}{\tau^2} \exp\left(-\frac{\tau}{RC}\right) + \frac{RC}{\tau} \\ & \left. - \frac{R^2 C^2}{2\tau^2} \right] + C\Delta V \Delta V_{\text{att}} \left[-\frac{RC}{\tau} \left\{ \exp\left(-\frac{\tau}{RC}\right) - 1 \right\} \right]. \end{aligned} \quad (4.39)$$

In the limit of abrupt polarization, this becomes Eq. (4.13), with $\Delta V_C(t) = \Delta V$.

The heat contributed after prolonged polarization in period 2, according

to Eqs. (4.12), (4.38), and (4.39) becomes

$$\begin{aligned}
 q_{\text{ch},2}(t \rightarrow \infty) = & \frac{C(\Delta V)^2}{2} \left(6f \frac{RC}{\tau} \exp\left(-\frac{\tau}{RC}\right) - [1 - 3f] \frac{R^2 C^2}{\tau^2} \exp\left(-\frac{2\tau}{RC}\right) \right. \\
 & + [2 - 6f] \frac{R^2 C^2}{\tau^2} \exp\left(-\frac{\tau}{RC}\right) - 6f \frac{RC}{\tau} - [1 - 3f] \frac{R^2 C^2}{\tau^2} \Big) \\
 & - C\Delta V \Delta V_{\text{att}} \left[\frac{RC}{\tau} \left\{ \exp\left(-\frac{\tau}{RC}\right) - 1 \right\} \right].
 \end{aligned} \tag{4.40}$$

In the limit of slow polarization, this formula leads to a value of zero, since charging completely takes place during period 1. In the limit of abrupt polarization, the equilibrium result found in Chapter 3 is retrieved:

$$\lim_{\tau \rightarrow 0} q_{\text{ch},2}(t \rightarrow \infty) = -\frac{C(\Delta V)^2}{2} [1 + 3f] + C\Delta V \Delta V_{\text{att}}. \tag{4.41}$$

The total heat of charging is the sum of the heats in periods 1 [Eq. (4.27)] and 2 [Eq. (4.40)]:

$$\begin{aligned}
 q_{\text{ch}} = q_{\text{ch},1} + q_{\text{ch},2} = \\
 -C(\Delta V)^2 \left[\frac{3}{2}f + \frac{RC}{\tau} + \frac{R^2 C^2}{\tau^2} \left(\exp\left(-\frac{\tau}{RC}\right) - 1 \right) \right] + C\Delta V \Delta V_{\text{att}}.
 \end{aligned} \tag{4.42}$$

The difference between the total heat production and the reversible heat production (Eq. 4.28) gives an expression for the irreversible heat:

$$q_{\text{irr, ch}} = q_{\text{ch}} - q_{\text{rev}} = -C(\Delta V)^2 \left[\frac{RC}{\tau} + \frac{R^2 C^2}{\tau^2} \left(\exp\left(-\frac{\tau}{RC}\right) - 1 \right) \right]. \tag{4.43}$$

In the limit of abrupt polarization, $q_{\text{irr, ch}}$ becomes $-C(\Delta V)^2$.

Finally, the heat production rate in period 2 follows from Eqs. (4.15), (4.18),

(4.22), (4.31), and (4.36):

$$\begin{aligned}
 \frac{dq_{\text{ch},2}(t)}{dt} = & \frac{C(\Delta V)^2}{\tau} \left\{ -3f \exp \left[-\frac{t-\tau}{RC} \right] - [1-3f] \frac{RC}{\tau} \exp \left[-2\frac{t-\tau}{RC} \right] \right. \\
 & + 2[1-3f] \frac{RC}{\tau} \exp \left[\frac{-2t-\tau}{RC} \right] + 3f \exp \left(-\frac{t}{RC} \right) \\
 & \left. - [1-3f] \frac{RC}{\tau} \exp \left[\frac{-2t}{RC} \right] \right\} \\
 & + \frac{C\Delta V\Delta V_{\text{att}}}{\tau} \left\{ \exp \left[-\frac{t-\tau}{RC} \right] - \exp \left(-\frac{t}{RC} \right) \right\}.
 \end{aligned} \tag{4.44}$$

Note that, when τ goes to infinity, charging already took place in period 1 and nothing happens in period 2. The work, heat, and energy change in period 2 then all go to zero. In the limit of abrupt polarization, Eq. (4.44) becomes

$$\begin{aligned}
 \lim_{\tau \rightarrow 0} \frac{dq_{\text{ch},2}(t)}{dt} = & \frac{(\Delta V)^2}{R} \left[-3f \exp \left(-\frac{t}{RC} \right) - [1-3f] \exp \left(\frac{-2t}{RC} \right) \right] \\
 & + \frac{\Delta V\Delta V_{\text{att}}}{R} \exp \left(-\frac{t}{RC} \right).
 \end{aligned} \tag{4.45}$$

4.8 Appendix 3: Formulas for period 3 (discharging, $0 \leq t \leq \tau$)

Period 3 starts with a charge $C\Delta V$ on the capacitor. Combination of Eqs. (4.6), and (4.8) gives the time-dependent voltage drop across the capacitor:

$$\Delta V_C(t) = \frac{C\Delta V + \int I(t)dt}{C}. \tag{4.46}$$

For $\tau > 0$, the current is zero at $t=0$ s and later given by:

$$I_{\text{dis},3}(t) = -\frac{C\Delta V}{\tau} \left[1 - \exp \left(-\frac{t}{RC} \right) \right], \quad 0 \leq t \leq \tau. \tag{4.47}$$

At time τ , the current is

$$I_{\text{dis},3}(\tau) = -\frac{C\Delta V}{\tau} \left[1 - \exp \left(-\frac{\tau}{RC} \right) \right]. \tag{4.48}$$

In the limit of abrupt application of the discharging potential, Eq. (4.48) becomes

$$\lim_{\tau \rightarrow 0} I_{\text{dis},3}(\tau) = -\frac{\Delta V}{R}. \quad (4.49)$$

The time-dependent charge and charge at time τ are also comparable to those during charging [Eqs. (4.20) and (4.21)], but with a minus sign and a charge at time $t=0$ s:

$$\Delta Q_{\text{dis},3}(t) = C\Delta V - \frac{C\Delta V}{\tau} \left[t + RC \left\{ \exp\left(-\frac{t}{RC}\right) - 1 \right\} \right], \quad (4.50)$$

$$\Delta Q_{\text{dis},3}(\tau) = C\Delta V - C\Delta V \left[1 + \frac{RC}{\tau} \left\{ \exp\left(-\frac{\tau}{RC}\right) - 1 \right\} \right]. \quad (4.51)$$

The charge is $C\Delta V$ at time $t=0$ s and it goes to zero as τ goes to infinity.

The work [via Eqs. (4.4), (4.14), and (4.47)] does not only change sign compared to period 1, but the form of the formula changes as well:

$$\begin{aligned} w_{\text{dis},3}(t) = & -\frac{C(\Delta V)^2}{\tau^2} \left[\tau t + \tau RC \exp\left(-\frac{t}{RC}\right) - \tau RC - \frac{t^2}{2} \right. \\ & \left. - tRC \exp\left(-\frac{t}{RC}\right) - (RC)^2 \exp\left(-\frac{t}{RC}\right) + (RC)^2 \right]. \end{aligned} \quad (4.52)$$

The work that has been performed on the system at time τ is slightly different compared to the situation in period 1 [Eq. (4.23)]:

$$w_{\text{dis},3}(\tau) = -C(\Delta V)^2 \left[\frac{1}{2} - \frac{RC}{\tau} - \frac{(RC)^2}{\tau^2} \exp\left(-\frac{\tau}{RC}\right) + \frac{(RC)^2}{\tau^2} \right]. \quad (4.53)$$

However, in the limit of slow polarization, the work is precisely opposite to that during charging [Eq. (4.24)]:

$$\lim_{\tau \rightarrow \infty} w_{\text{dis}}(\tau) = -\frac{1}{2}C(\Delta V)^2. \quad (4.54)$$

This leads to net zero work during a reversible charge-discharge cycle.

Just like during charging, the work is zero in the limit of abrupt polarization. The time-dependent internal energy change, calculated from the start of discharging, is given by the energy at time t [Eq. (4.13)], minus the internal

energy at the start of discharging, Eq. (4.39):

$$\begin{aligned} \Delta U_{\text{dis},3}(t) = & \frac{C(\Delta V)^2}{2}[1-3f] \left[-2\frac{t}{\tau} + \left(\frac{t}{\tau}\right)^2 + 2\frac{tRC}{\tau^2} \exp\left(-\frac{t}{RC}\right) \right. \\ & - 2\frac{tRC}{\tau^2} - 2\frac{RC}{\tau} \exp\left(-\frac{t}{RC}\right) + \left(\frac{RC}{\tau}\right)^2 \exp\left(-\frac{2t}{RC}\right) \\ & \left. - 2\left(\frac{RC}{\tau}\right)^2 \exp\left(-\frac{t}{RC}\right) + 2\frac{RC}{\tau} + \left(\frac{RC}{\tau}\right)^2 \right] \\ & + C\Delta V\Delta V_{\text{att}} \left[-\frac{t}{\tau} - \frac{RC}{\tau} \exp\left(-\frac{t}{RC}\right) + \frac{RC}{\tau} \right]. \end{aligned} \quad (4.55)$$

The internal energy at $t=0$ s is given by Eq. (4.39). At time τ , the internal energy is

$$\begin{aligned} \Delta U_{\text{dis},3}(\tau) = & -\frac{C(\Delta V)^2}{2}[1-3f] \left[1 - \left(\frac{RC}{\tau}\right)^2 \exp\left(-\frac{2\tau}{RC}\right) \right. \\ & \left. + 2\left(\frac{RC}{\tau}\right)^2 \exp\left(-\frac{\tau}{RC}\right) - \left(\frac{RC}{\tau}\right)^2 \right] \\ & - C\Delta V\Delta V_{\text{att}} \left[1 + \frac{RC}{\tau} \exp\left(-\frac{\tau}{RC}\right) - \frac{RC}{\tau} \right]. \end{aligned} \quad (4.56)$$

This is zero in the limit of $\tau \rightarrow 0$. An expression for the heat at time τ is found using Eqs. (4.12), (4.53), and (4.56):

$$\begin{aligned} q_{\text{dis},3}(\tau) = & -\frac{C(\Delta V)^2}{2} \left[-3f - [1-3f] \left(\frac{RC}{\tau}\right)^2 \exp\left(-\frac{2\tau}{RC}\right) \right. \\ & \left. + [4-6f] \left(\frac{RC}{\tau}\right)^2 \exp\left(-\frac{\tau}{RC}\right) + \frac{2RC}{\tau} + [-3+3f] \frac{(RC)^2}{\tau^2} \right] \\ & - C\Delta V\Delta V_{\text{att}} \left[1 + \frac{RC}{\tau} \exp\left(-\frac{\tau}{RC}\right) - \frac{RC}{\tau} \right]. \end{aligned} \quad (4.57)$$

This is zero in the limit of abrupt polarization. In the limit of slow polarization, the negative reversible heat is retrieved:

$$\lim_{\tau \rightarrow \infty} q_{\text{dis},3}(\tau) = \frac{3}{2}fC(\Delta V)^2 - C\Delta V\Delta V_{\text{att}} = -q_{\text{rev}}. \quad (4.58)$$

An expression for the heat production rate is found via Eqs. (4.15), (4.52), (4.55):

$$\begin{aligned} \frac{dq_{\text{dis},3}(t)}{dt} = & \frac{C(\Delta V)^2}{\tau^2} \left[3f\tau - 3ft + [1 - 3f]2RC \exp\left(-\frac{t}{RC}\right) \right. \\ & + 3ft \exp\left(-\frac{t}{RC}\right) - [1 - 3f]RC - 3f\tau \exp\left(-\frac{t}{RC}\right) \\ & \left. - [1 - 3f]RC \exp\left(-\frac{2t}{RC}\right) \right] + \frac{C\Delta V\Delta V_{\text{att}}}{\tau} \left[\exp\left(-\frac{t}{RC}\right) - 1 \right]. \end{aligned} \quad (4.59)$$

4.9 Appendix 4: Formulas for period 4 (discharging, $t \geq \tau$)

In period 4, according to Eqs. (4.30) and (4.48), the discharging current is given by

$$I_{\text{dis},4}(t) = -\frac{C\Delta V}{\tau} \left[1 - \exp\left(-\frac{\tau}{RC}\right) \right] \exp\left(-\frac{t-\tau}{RC}\right). \quad (4.60)$$

In the limit of abrupt polarization, this becomes

$$I_{\text{dis},4}(t) = -\frac{\Delta V}{R} \exp\left(-\frac{t}{RC}\right). \quad (4.61)$$

Integration of $I_{\text{dis},4}(t)$ gives the total charge in period 4:

$$\Delta Q_{\text{dis},4}(\infty) = -C\Delta V \frac{RC}{\tau} \left[1 - \exp\left(-\frac{\tau}{RC}\right) \right]. \quad (4.62)$$

During period 4, the applied potential ΔV is 0 V (Eq. 4.5), so that according to Eq. (4.14) no work is performed on the system:

$$w_{\text{dis},4}(t) = 0. \quad (4.63)$$

The energy that remains to be lost is the energy of the system at time τ . According to Eqs. (4.13) and (4.6), this is the energy at a charge $-\Delta Q_{\text{dis},4}(\infty)$:

$$\begin{aligned} \Delta U_{\text{dis},4}(\infty) = & -C(\Delta V)^2 \left[\frac{1}{2} - \frac{3}{2}f \right] \left(\frac{RC}{\tau} \left[1 - \exp\left(-\frac{\tau}{RC}\right) \right] \right)^2 \\ & - C\Delta V\Delta V_{\text{att}} \frac{RC}{\tau} \left[1 - \exp\left(-\frac{\tau}{RC}\right) \right]. \end{aligned} \quad (4.64)$$

In the limit of abrupt polarization, the result found in Chapter 3 is retrieved:

$$\lim_{\tau \rightarrow 0} \Delta U_{\text{dis},4}(\infty) = -C(\Delta V)^2 \left[\frac{1}{2} - \frac{3}{2}f \right] - C\Delta V\Delta V_{\text{att}}. \quad (4.65)$$

Before the system is fully discharged, the time-dependent energy is found via $\Delta U_4(t) = \Delta U(t) - \Delta U(\tau)$, where $\Delta U(t)$ and $\Delta U(\tau)$ are found using Eq. (4.13) and determining $\Delta V_C(t)$ from the amounts of charge present at times t and τ :

$$\begin{aligned} \Delta U_{\text{dis},4}(t) = & C(\Delta V)^2 \left[\frac{1}{2} - \frac{3}{2}f \right] \left(\frac{RC}{\tau} \right)^2 \left[1 - \exp\left(-\frac{\tau}{RC}\right) \right]^2 \left[\exp\left(-2\frac{t-\tau}{RC}\right) - 1 \right] \\ & + C\Delta V\Delta V_{\text{att}} \frac{RC}{\tau} \left[1 - \exp\left(-\frac{\tau}{RC}\right) \right] \left[\exp\left(-\frac{t-\tau}{RC}\right) - 1 \right]. \end{aligned} \quad (4.66)$$

In the limit of abrupt polarization, the time-dependent energy in period 4 is

$$\begin{aligned} \lim_{\tau \rightarrow 0} \Delta U_{\text{dis},4}(t) = & C(\Delta V)^2 \left[\frac{1}{2} - \frac{3}{2}f \right] \left[\exp\left(-\frac{2t}{RC}\right) - 1 \right] \\ & + C\Delta V\Delta V_{\text{att}} \left[\exp\left(-\frac{t}{RC}\right) - 1 \right]. \end{aligned} \quad (4.67)$$

Since the work is zero [Eq. (4.63)], the time-dependent heat produced in period 4 is equal to the energy change:

$$q_{\text{dis},4}(t) = \Delta U_4(t) \quad (4.68)$$

The heat production rate in period 4 is found using Eqs. (4.15), (4.63), and (4.66):

$$\begin{aligned} \frac{dq_{\text{dis},4}(t)}{dt} = & -C(\Delta V)^2 \frac{RC}{\tau^2} [1 - 3f] \left[1 - \exp\left(-\frac{\tau}{RC}\right) \right]^2 \left[\exp\left(-2\frac{t-\tau}{RC}\right) \right] \\ & - \frac{C\Delta V\Delta V_{\text{att}}}{\tau} \left[1 - \exp\left(-\frac{\tau}{RC}\right) \right] \left[\exp\left(-\frac{t-\tau}{RC}\right) \right]. \end{aligned} \quad (4.69)$$

In the limit of abrupt polarization, the heat production in period 4 is

$$\begin{aligned} \lim_{\tau \rightarrow 0} \frac{dq_{\text{dis},4}(t)}{dt} = & -\frac{(\Delta V)^2}{R} [1 - 3f] \exp\left(-\frac{2t}{RC}\right) \\ & - \frac{\Delta V\Delta V_{\text{att}}}{R} \exp\left(-\frac{t}{RC}\right). \end{aligned} \quad (4.70)$$

The total discharging heat produced in periods 3 and 4 follows from Eqs. (4.57), (4.64), and (4.68):

$$\begin{aligned} q_{\text{dis}} = & -C(\Delta V)^2 \left[-\frac{3}{2}f + \left(\frac{RC}{\tau}\right)^2 \exp\left(-\frac{\tau}{RC}\right) + \frac{RC}{\tau} - \frac{(RC)^2}{\tau^2} \right] \\ & - C\Delta V\Delta V_{\text{att}}. \end{aligned} \quad (4.71)$$

In the limit of abrupt polarization, this becomes

$$\lim_{\tau \rightarrow 0} q_{\text{dis}} = -\frac{C(\Delta V)^2}{2} [1 - 3f] - C\Delta V\Delta V_{\text{att}}. \quad (4.72)$$

The integral Joule heat during discharging is found by addition of q_{dis} (Eq. 4.71) and q_{rev} (Eq. 4.28), yielding the same formula as for the Joule heat during charging (Eq. 4.43):

$$q_{\text{irr},\text{dis}} = q_{\text{dis}} + q_{\text{rev}} = -C(\Delta V)^2 \left[\frac{RC}{\tau} + \frac{R^2 C^2}{\tau^2} \left(\exp\left(-\frac{\tau}{RC}\right) - 1 \right) \right]. \quad (4.73)$$

4.10 Appendix 5: Additional figures for abrupt polarization, $\tau = 100$ s, and $\tau = 1000$ s at different potentials

The following graphs are figures comparable to Figs. 4.3, 4.4, and 4.6, with applied potentials of 0.3 V (Figs. 4.8-4.10), -0.3 V (Figs. 4.11-4.13), and -0.5 V (Figs. 4.14-4.16). The values for f and ΔV_{att} were those found in Fig. 4.2.

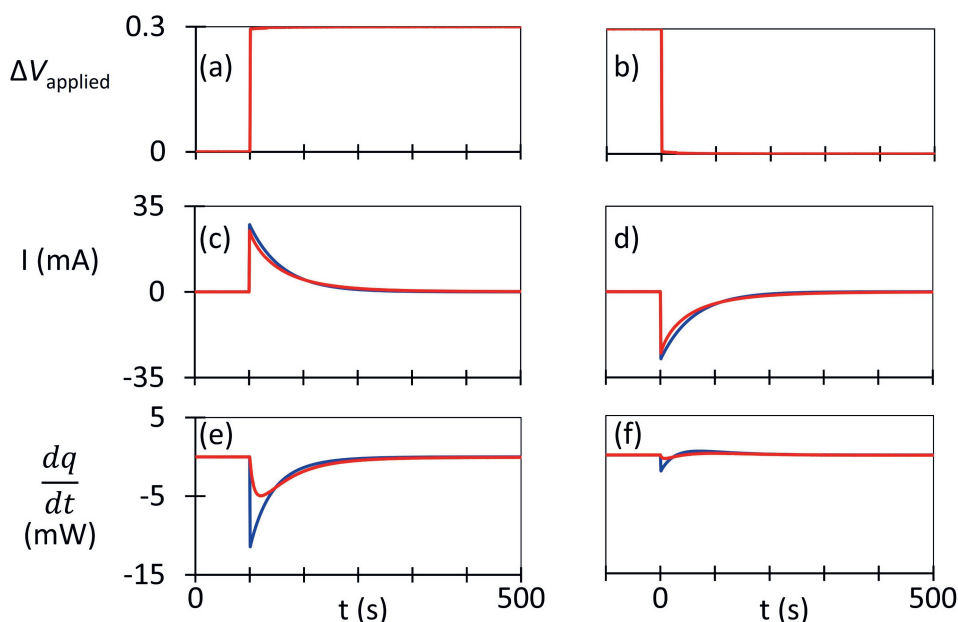


Figure 4.8: Theoretical (blue) and experimental (red) time-dependence of electrical current and heat production rate in the case of abrupt changes of the potential applied to a capacitive porous carbon electrode in 1 M NaCl ($\tau = 0$ s, charging potential $\Delta V = 0.3$ V). Time dependence of (a,b) the applied potential, (c,d) the electrical current, and (e,f) the heat production rate (an instrumental offset of 0.85 mW was subtracted).

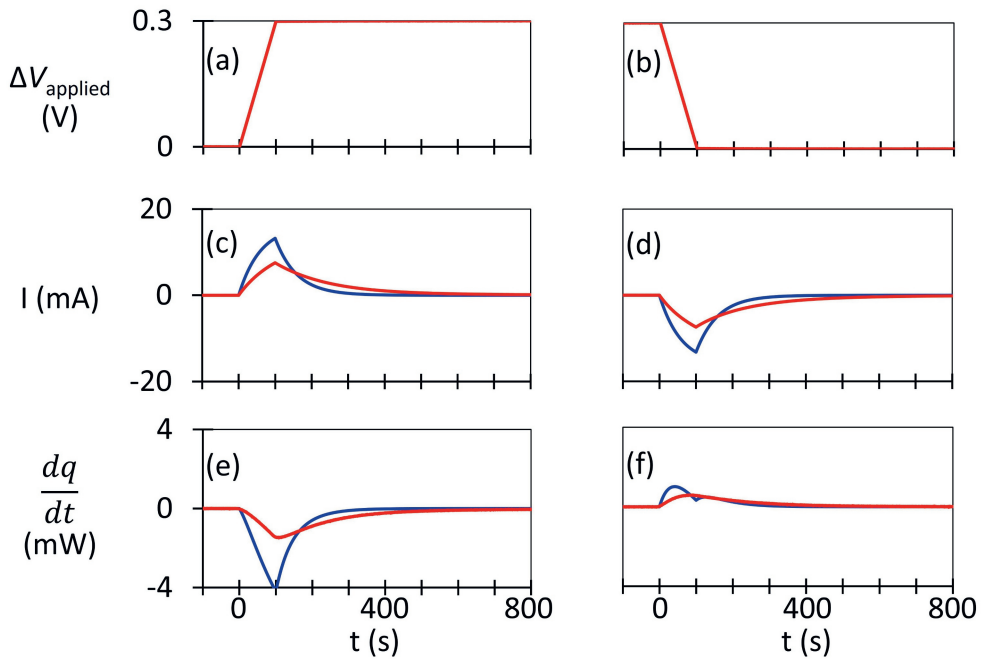


Figure 4.9: As in Fig. 4.8, but now for gradual change of the applied potential, with $\tau = 100$ s. In (e) and (f), an instrumental offset of 0.71 mW was subtracted.

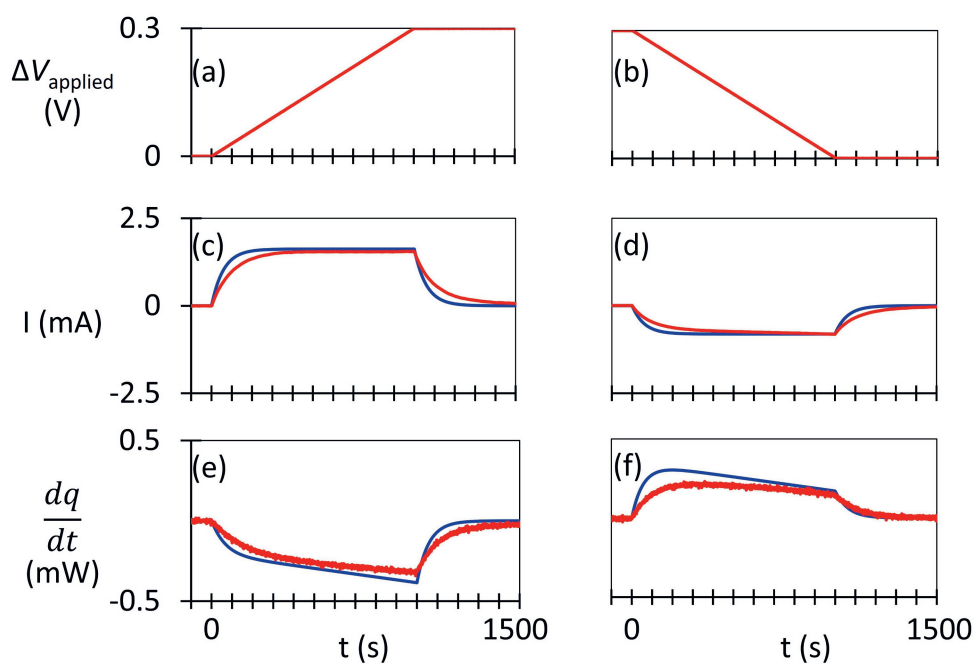


Figure 4.10: As in Fig. 4.8, but now for gradual change of the applied potential, with $\tau = 1000$ s. In (e) and (f), an instrumental offset of 0.74 mW was subtracted.

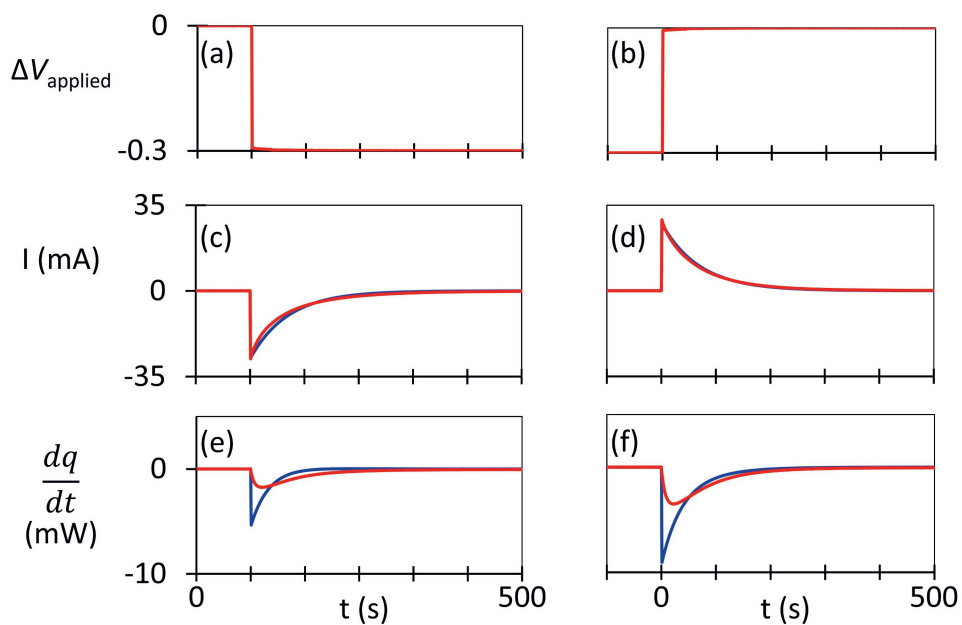


Figure 4.11: As in Fig. 4.8, but now for an applied potential of $\Delta V = -0.3$ V. In (e) and (f), an instrumental offset of 0.81 mW was subtracted.

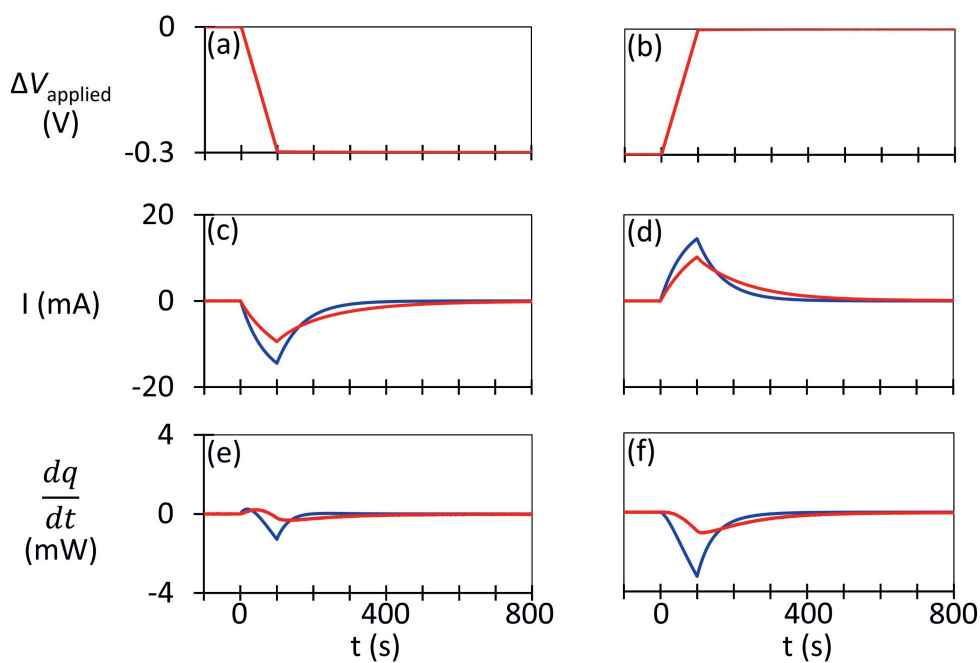


Figure 4.12: As in Fig. 4.11, but now for gradual change of the applied potential, with $\tau = 100$ s. In (e) and (f), an instrumental offset of 0.75 mW was subtracted.

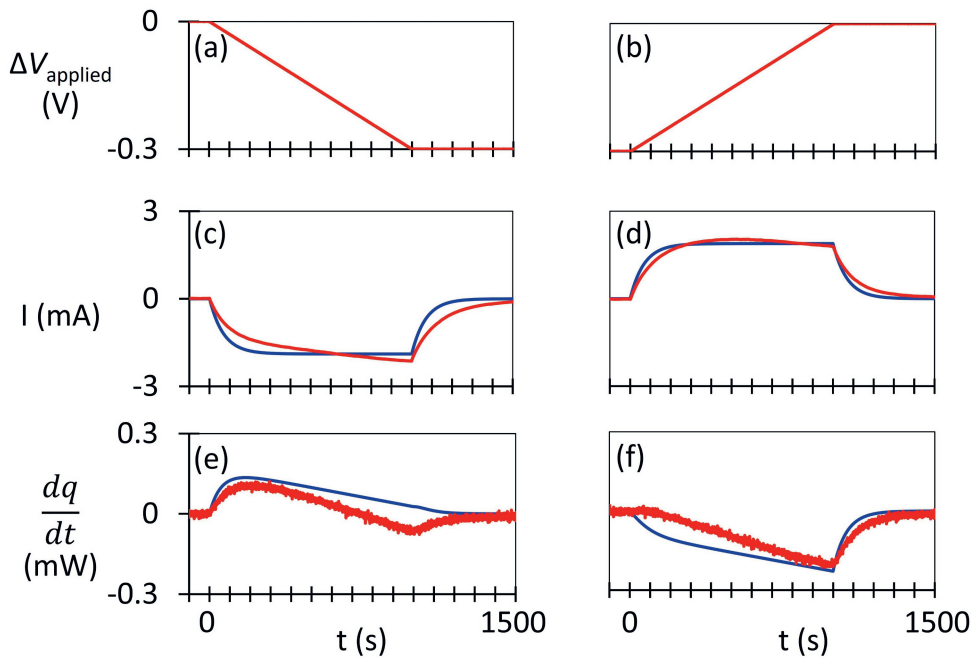


Figure 4.13: As in Fig. 4.11, but now for gradual change of the applied potential, with $\tau = 1000$ s. In (e) and (f), an instrumental offset of 0.74 mW was subtracted.

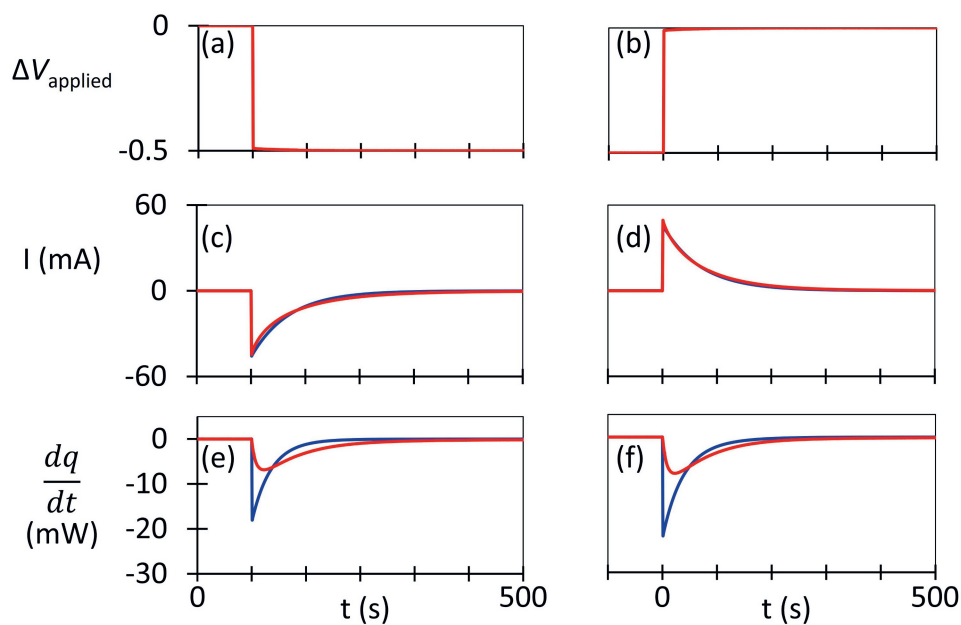


Figure 4.14: As in Fig. 4.8, but now for an applied potential of $\Delta V = -0.5$ V. In (e) and (f), an instrumental offset of 0.82 mW was subtracted.

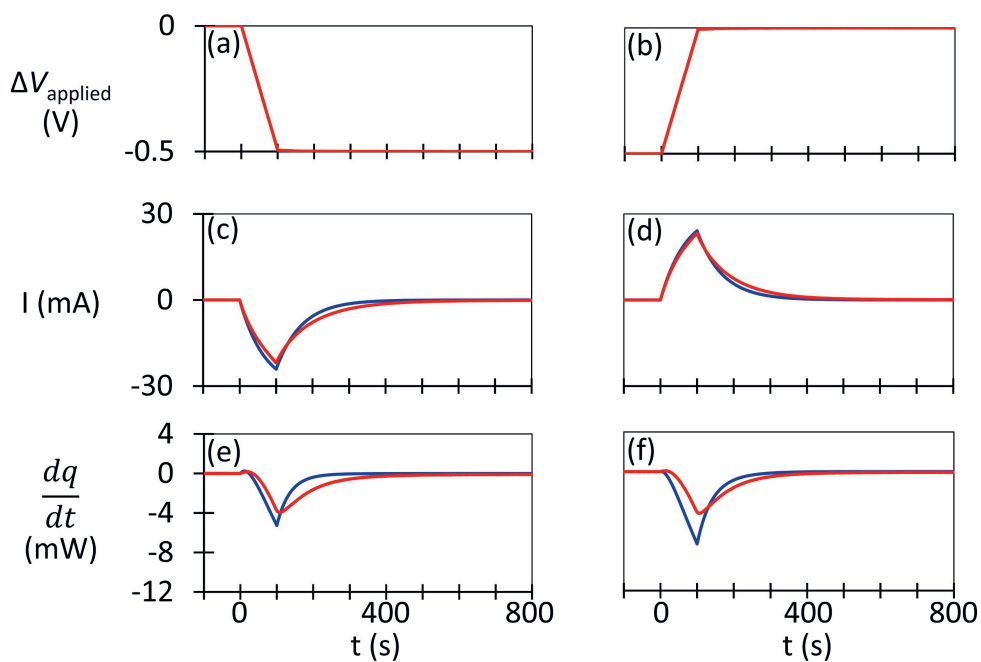


Figure 4.15: As in Fig. 4.14, but now for gradual change of the applied potential, with $\tau = 100$ s. In (e) and (f), an instrumental offset of 0.74 mW was subtracted.

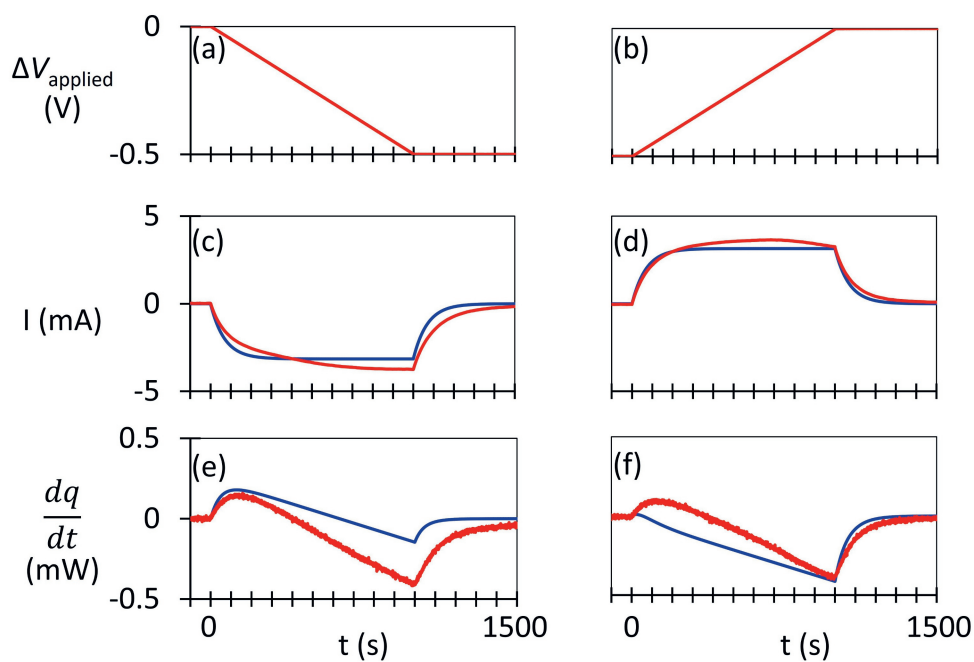


Figure 4.16: As in Fig. 4.14, but now for gradual change of the applied potential, with $\tau = 1000$ s. In (e) and (f), an instrumental offset of 0.72 mW was subtracted.

Chapter 5

Cathodic versus Anodic Charging Dynamics of Capacitive Porous Carbon Electrodes in Aqueous Salt Solutions

Abstract

Porous electrodes are used to store electrical energy, in supercapacitors, and to desalinate water, in capacitive deionization. In such electrodes, the charging of the electrical double layer is much slower than for nonporous electrodes, because of rate-determining ionic transport through the porous network. For individual pores, it has been shown that it is ultimately the transport of the counterions that is limiting, rather than that of the coions, and it has been argued that this is also the case for macroscopic porous electrodes. To test this prediction, we measured (dis)charging current transients of capacitive porous carbon electrodes in aqueous solutions of NaCl, KCl, MgCl₂, and LaCl₃, both at cathodic and anodic applied potentials. In solutions of the first three salts, the late-time current decay was slower in the cathodic than in the anodic range, even in KCl solution, despite the nearly equal limiting diffusion coefficients of potassium and chloride ions. A possible explanation involves the higher capacitance that was measured in the cathodic than in the anodic range, ascribed to different specific adsorptions of cations and anions. Consequently, the local RC times could be higher in the cathodic than in the anodic range, for the smallest pores whose electrical double layers are not yet fully charged near the end of the current transients.

5.1 Introduction

The electrical double layer is key in the commercial applications of porous carbon electrodes. This is where the electrical energy is stored in supercapacitors [35, 37, 60] and where ions are adsorbed during capacitive deionization of water [9, 13, 61]. The double layer is found at the surface of the pores, where it consists of electronic charge within the carbon and opposite ionic charge inside the pores. Most of the solid-liquid interface is at the walls of micropores, <2 nm in width, and the micropores are interconnected mostly via mesopores, 2-50 nm in width [10, 11, 110]. A drawback of these small dimensions is that charging and discharging are relatively slow, limited by the rate of ionic transport through the porous network. The time required to add or to remove most of the electric charge is on the order of RC , where R is the resistance of the electrolyte solution and C is the capacitance of the electrical double layer. The capacitance is huge, thanks to a specific surface area of typically more than 1000 m^2 per gram of carbon [13]. Consequently, the (dis)charging of the electrical double layer is much slower than for a nonporous electrode, by several orders of magnitude [30, 111].

In theory, the charging rate of porous capacitive electrodes is initially determined by the migration of ions, characterized by the RC time, and later, the diffusion of ions takes over as the dominating transport process. Ionic diffusion occurs toward or away from the bulk electrolyte solution outside the porous network, and it is driven by concentration gradients that result from the adsorption or desorption ions at the pore walls. Diffusion becomes rate-limiting once the charging process is nearly complete and electric fields have become negligible in the propagation directions of the ions. This separation of an RC time regime and a diffusion regime is thought to occur not only in porous electrodes [30, 87, 111, 110, 112] but also at nonporous electrodes [113, 114, 115]. Theoretical descriptions of the charging dynamics of porous electrodes often involve an equivalent electrical circuit that consists of a transmission line, with local RC elements that represent individual pores and values of R that depend on the local ionic concentrations [30, 106, 111, 116, 117, 118]. Moreover, the long-range transport of ions mainly occurs through relatively wide pores, where the initial electric fields are sufficiently strong, as opposed to the micropores, where the electric potential is approximately constant [10, 11, 14, 15, 111].

In theory, at constant externally applied potential, the initial migration and the later diffusion of ions lead to bi-exponential decay of the electric current.

In experiment, it has indeed been found that the charging dynamics are not fully described by just one time constant. Bi-exponential decay was observed by Lian et al. [30], who analyzed potentiostatic current transients measured for a cell with two microporous carbon electrodes in aqueous NaCl solution [1]. The fitted time constants were lower than expected from theory, which was ascribed to decreased diffusivity of the ions in the pores. Helseth [106, 109] measured the time-dependent voltage of commercial supercapacitors during self-discharge, and the results were fitted using a stretched exponential function, once introduced by Kohlrausch to describe the charge decay of Leyden jars [119]. The physical origin of stretched exponential decay has been ascribed to diffusion limitation [107] or to a continuous distribution of relaxation times [106, 109], due to polydispersity of pore widths and lengths, as in fractal electrodes [108, 120]. To study the dynamics inside micropores, Forse et al. [121] used pulsed field NMR spectroscopy, finding that the self-diffusion coefficients of the ions can be orders of magnitude slower than in bulk solution. To study the dynamics inside larger pores, Tivony et al. [122] performed surface force measurements on individual pores of 30 to 375 nm in width, showing that the charging time increased as the pores became more narrow. In general, the sizes, geometries, and accessibilities of the pores matter not only for the charging rate, but also for the capacitance [10, 11, 19, 123, 124, 125, 126, 127, 128, 129]. A trade-off exists between high capacitance—obtained with pores barely wider than the size of the ions—and high charging rate—obtained with wider pores.

A fundamental question regarding the charging mechanism of electrical double layer capacitors is to what extent the ionic current is carried by the counterions or the coions. When both contributions are equal, coions are effectively exchanged for counterions [37]. Biesheuvel and Bazant noted that “coion outflow is always less than counterion adsorption” [110], which agrees with the much shorter distance that counterions have to travel from the solution inside a pore to the nearest pore wall, compared to the paths that coions must follow before they reach the edge of the porous network. This asymmetry implies that the charging dynamics can be different in the cathodic and anodic

ranges, in cases where cations and anions have different diffusion coefficients. This expectation is supported by results of Tivony et al. [122] who found that the charging of individual pores was slower cathodically than anodically, in cases where the cations had a smaller diffusion coefficient than the anions. To our knowledge, however, such a difference between cathodic and anodic charging has not yet been observed in the charging dynamics of macroscopic porous electrodes.

In this chapter, we present potentiostatic current transients measured during the (dis)charging of porous carbon electrodes, as a function of the applied potential during charging. We use an electrode material that was developed for capacitive deionization, containing both micropores and mesopores, and results are compared for aqueous solutions of NaCl, KCl, MgCl₂, and LaCl₃. The experimental methods are described in section 5.2, in particular the approach to measure in a 3-electrode configuration, in order to focus on the charging of the working electrode at its own applied potential. The data analysis is explained in section 5.3, including bi-exponential fitting, stretched exponential fitting, and a recently introduced method that does not require any fitting but nevertheless provides a time-dependent instantaneous time constant. Before the results of salt- and potential-dependent measurements are presented, the influence of faradaic effects is examined (section 5.4.1) and practical aspects of the different data analysis methods are discussed (sections 5.4.2 and 5.4.3). Finally, the cathodic and anodic capacitive charging dynamics are compared for the different salts (section 5.4.4).

5.2 Experimental

The same electrochemical cell was used as in Chapter 2. The working and counter electrodes were disks of 22 mm in diameter and 0.25 mm in thickness, consisting of porous carbon material developed for capacitive deionization [10, 11, 14, 15]. From nitrogen physisorption measurements, our porous carbon electrodes each had a surface area of 88 m², with 48 % of pore volume consisting of (presumably slit-shaped) micropores (<2 nm) and 9 % of pore volume consisting of mesopores (2-50 nm), the remaining pores being wider (see section 3.9).

An AMETEK PARSTAT MC-1000 multichannel potentiostat was used to apply potentials to the working electrode with respect to a reference electrode (RE), a Radiometer REF201 Ag/AgCl electrode with a saturated KCl salt bridge. Applied potentials V_{applied} are reported with respect to V_{OCP} , the potential of a discharged porous carbon electrode after prolonged equilibration under open circuit conditions. This is done by reporting values of $\Delta V = V_{\text{applied}} - V_{\text{OCP}}$.

Salt solutions were prepared from high purity salts: NaCl and KCl from Merck Emsure[®] (for analysis), MgCl_2 from Roth ($\geq 99\%$, p.a., ACS), and LaCl_3 from Sigma-Aldrich (ACS reagent). Water was obtained from a Millipore apparatus (Milli-Q, pH 7), and the solutions were degassed for half an hour in an ultrasonic bath before use.

Each measurement series started with a discharged electrode and half a day of equilibration under open circuit conditions, at a constant temperature of 22.0°C , maintained using a Julabo F25 refrigerated/heating circulator. Each charge-discharge cycle started by applying $\Delta V = 0\text{ V}$ for at least one hour, followed by applying another potential in the range from $\Delta V = -0.5\text{ V}$ to $\Delta V = +0.5\text{ V}$ for at least one hour, followed by discharging at an applied potential $\Delta V = 0\text{ V}$, also for an hour. For each salt, three series with charging potentials from -0.5 V to $+0.5\text{ V}$ were measured.

5.3 Data analysis

5.3.1 Bi-exponential fitting

To characterize the charging dynamics at short times t ($t < 100\text{ s}$) and at late times ($t > 2000\text{ s}$), the measured potentiostatic current transients were fitted to the following bi-exponential function:

$$I(t) = I_1 \exp\left(-\frac{t}{\tau_1}\right) + I_2 \exp\left(-\frac{t}{\tau_2}\right). \quad (5.1)$$

Here, $I(t)$ is the measured current (in A), and processes 1 and 2 are characterized by currents I_1 and I_2 and time constants τ_1 and τ_2 , respectively. Both for charging and discharging, the starting time was defined as $t = 0\text{ s}$ when the applied potential was abruptly changed. Process 1 was defined as the initial

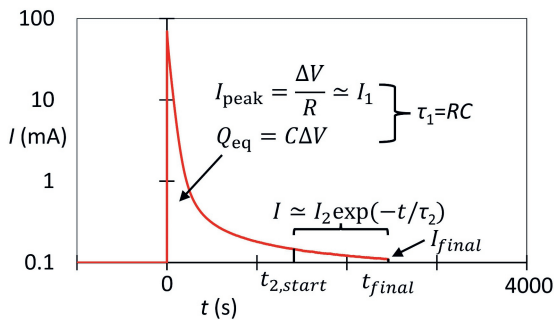


Figure 5.1: Schematic illustration of the bi-exponential fitting method of potentiostatic charging current transients, using Eq. (5.1). The measured current I decayed exponentially as a function of time t . The initial current I_{peak} was approximately equal to I_1 and it indicated the value of the resistance R . The integral of the current transient, until the final time t_{final} of the measurements, gave the equilibrium charge Q_{eq} and the capacitance C . Process 1 was assumed to have time constant $\tau_1 = RC$, and the values of I_2 and τ_2 were obtained from a mono-exponential fit going from $t_{2,\text{start}}$ until t_{final} . Although the finally measured current I_{final} was not zero, the current was assumed to decay asymptotically toward zero.

($I_1 \gg I_2$) and most rapid of the two processes ($\tau_1 \ll \tau_2$), which also accounted for most of the total charge ($I_1\tau_1 \gg I_2\tau_2$). Moreover, it was assumed *a priori* that $\tau_1 = RC$, where R is the total measured resistance and C is the total capacitance of the electrode. The value of R was obtained from ΔV and the initial peak current I_{peak} during charging, see Fig. 5.1:

$$R = \Delta V / I_{\text{peak}}. \quad (5.2)$$

The capacitance was calculated from the total equilibrium charge Q_{eq} :

$$C = Q_{\text{eq}} / \Delta V. \quad (5.3)$$

The charge Q_{eq} was found by integrating the current starting at $t=0$ s and ending at t_{final} , the time at which the measurement of a transient was stopped:

$$Q_{\text{eq}} = \int_0^{t_{\text{final}}} I(t) dt. \quad (5.4)$$

At times $t \gg RC$, it was assumed that the second process dominated, so that $I(t) \approx I_2 \exp[-t/\tau_2]$. On this basis, I_2 and τ_2 were determined from a least-squares fit of $\ln[I(t)]$ against t . This fit started at a time $t_{2,\text{start}}$ and continued until t_{final} , at which time the current was I_{final} , see Fig. 5.1. The exponential decay of the current was then not yet complete, but measurements could not be continued indefinitely, for lack of time and because the signal-to-noise ratio deteriorated. It was assumed that further prolongation of the measurements would have led to further decrease of the current toward zero. In other words, Eq. (5.1) assumes that the current was purely capacitive, without faradaic component. The reliability of this assumption will be discussed later.

It is remarked that Eq. (5.1) gives an empirical description. It implies that the contribution of process 2 to the current, $I_2 \exp(-t/\tau_2)$, is maximal at $t=0$ s, which is probably not physical. In reality, process 2—corresponding to eventual diffusion-limited charging—probably can occur only once process 1—corresponding to the initial migration of ions—has proceeded sufficiently long to generate ionic concentration gradients. Nevertheless, since process 1 dominates initially and process 2 dominates in the end, Eq. (5.1) does allow for a characterization of both processes.

5.3.2 Stretched exponential fitting

As an alternative to Eq. (5.1), it was also attempted to fit the current transients to a stretched exponential decay function [106, 107, 108, 109, 119, 120]. As will be shown later, the following single stretched exponential function could not describe the data:

$$I(t) = I_1 \exp\left(-\left[\frac{t}{\tau_s}\right]^\beta\right), \quad (5.5)$$

where τ_s is a time constant and β is a dimensionless constant between 0 and 1. It will be shown that better fits were obtained by describing process 1 as in Eqs. (5.1)-(5.3), with $\tau_1 = RC$, and by using a stretched exponential function only to fit process 2:

$$I(t) = I_1 \exp\left(-\frac{t}{\tau_1}\right) + I_s \exp\left(-\left[\frac{t}{\tau_s}\right]^\beta\right), \quad (5.6)$$

where I_s is a current (constant).

5.3.3 Instantaneous time constant analysis

For a final analysis of the data, we adapted a formula that Ma et al. [114] recently proposed to analyze their theoretically calculated bi-exponential current transients for nonporous electrodes. They introduced an “instantaneous relaxation time”, given by

$$\tau_i(t) = - \left[\frac{d \ln (1 - Q(t)/Q_{\text{eq}})}{dt} \right]^{-1}, \quad (5.7)$$

where $Q(t)$ is the amount of charge that has been measured at time t . For the analysis of experiments, we used $I(t) = dQ(t)/dt$ to simplify Eq. (5.7) into the following form:

$$\tau_i(t) = \frac{Q_{\text{eq}} - Q(t)}{I(t)}. \quad (5.8)$$

A practical advantage of this approach in the analysis of experimental data is that it requires no numerical fitting to an assumed model or equation. Only the time-dependent current $I(t)$ needs to be known, and Q_{eq} and $Q(t)$ need to be calculated by integration of $I(t)$.

In Fig. 5.2, this analysis approach is illustrated for simulated bi-exponential transients calculated via Eq. (5.1). At $t = 0$ s, the charge is zero, so that $Q_{\text{eq}} - Q(t) = I_1\tau_1 + I_2\tau_2$ (assuming that $t_{\text{final}} \rightarrow \infty$) and $I = I_1 + I_2$. Consequently, Eq. (5.8) leads to

$$\tau_i(0) = \frac{I_1\tau_1 + I_2\tau_2}{I_1 + I_2}. \quad (5.9)$$

This implies that $\tau_i(t = 0\text{s}) > \tau_1$, whereas the analysis of experimental data using Eq. (5.8) should result in $\tau_i(t = 0\text{s}) = RC$, because at $t = 0$ s, $Q_{\text{eq}} - Q(t) = C\Delta V$, and $I(t) = \Delta V/R$. This illustrates that when it is assumed that $I(t)$ is described by Eq. (5.1), the further assumption that $\tau_1 = RC$ is an approximation.

In the high- t limit, process 2 dominates, so that

$$I(t) \approx I_2 \exp \left[-\frac{t}{\tau_2} \right], t \gg RC. \quad (5.10)$$

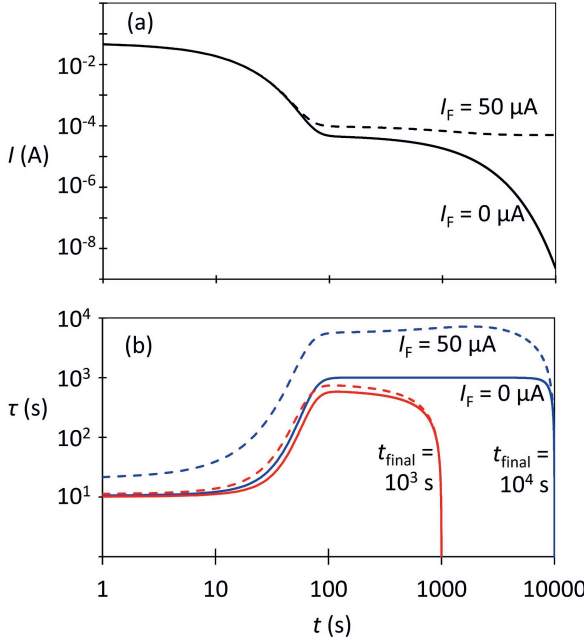


Figure 5.2: Illustration of the analysis of a bi-exponential transient via the “instantaneous relaxation time” approach proposed by Ma et al. [114], adapted here in the form of Eq. (5.8). (a) Current transient calculated using Eq. (5.1) for $I_1 = 50$ mA, $\tau_1 = 10$ s, $I_2 = 50$ μ A, and $\tau_2 = 1000$ s. (b) Time-dependence of the instantaneous relaxation time calculated via Eq. (5.8). At $t = 0$ s, $\tau_i(t)$ equals the RC time, whereas in the limit of high t , $\tau_i(t)$ approximates the diffusion time τ_2 . The curves were calculated for short and long durations of the simulated measurements, $t_{\text{final}} = 10^3$ s and $t_{\text{final}} = 10^4$ s, respectively. The dashed lines in (a) and (b) correspond to the case that there is not only capacitive current but also a constant faradaic current equal to $I_F = 50$ μ A.

Consequently,

$$Q_{\text{eq}} - Q(t) \approx \int_t^\infty I_2 \exp\left[-\frac{t'}{\tau_2}\right] dt' = I_2 \tau_2 \exp\left[-\frac{t}{\tau_2}\right], t \gg RC. \quad (5.11)$$

According to Eqs. (5.8), (5.10), and (5.11), the high- t limit of the instantaneous time constant is therefore given by

$$\tau_i(\infty) = \tau_2. \quad (5.12)$$

Figure 5.2 also illustrates the effect of the finite length of a measured current transient on the plot of the time dependence of the instantaneous time constant. A plateau is reached near the final time t_{final} of the transient, when $\tau_i \sim \tau_2$, but this plateau is better defined when $t_{\text{final}} \gg \tau_2$ than when this is not the case. Moreover, near the end of the transient, the instantaneous time constant rapidly drops to zero. This is because in Eq. (5.8), the current $I(t)$ has not yet decayed to zero at t_{final} , whereas the measured charge $Q(t)$ does decrease toward the incomplete value of the equilibrium charge Q_{eq} given by $Q(t)$ at time t_{final} , see Eq. (5.4).

Figure 5.2 finally also shows how a small constant faradaic current I_F affects the $\tau_i(t)$ results. The time-dependent current flattens off, which would lead to an increased time constant τ_2 when fitted to Eq. 5.1. Moreover, for the longest simulated transient ($t_{\text{final}} = 10^4$ s), the integral faradaic current has the largest contribution to the determination of Q_{eq} via Eq. (5.4), resulting in a higher plateau value of $\tau_i(t)$ at long times t . For the shortest transient ($t_{\text{final}} = 10^3$ s), the faradaic current has an almost negligible effect on the $\tau_i(t)$ curve.

5.4 Results and Discussion

5.4.1 Faradaic effects

The analysis methods presented in Section 5.3 focus on the charging dynamics of electrodes that are mostly capacitive. Before those methods are applied, evidence for the presence of faradaic currents is examined.

Figure 5.3 shows an overview of potentials relevant in the measurements.

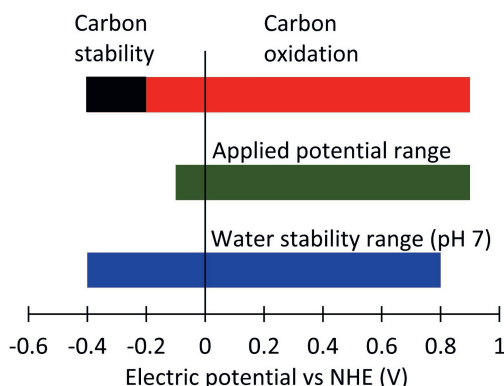


Figure 5.3: Comparison of the range of applied potentials with the stability ranges of graphitic carbon and water [130].

The experimental ΔV range from -0.5 to $+0.5$ V corresponded to applied potentials from -0.3 to $+0.7$ V vs Ag/AgCl/saturated KCl and -0.1 to $+0.9$ V versus NHE. This largely remained within the stability range of water at pH 7 (-0.4 to $+0.8$ V). At the most positive applied potential, however ($\Delta V = +0.5$ V), oxidation of water was thermodynamically possible. Moreover, bulk graphitic carbon is inert only within a range from about -0.4 to -0.2 V versus NHE at pH 7 [130]. Consequently, the carbon surface was likely to be in an oxidized state at most applied potentials. This includes the potential at which the electrode was discharged after cathodic or anodic charging, that is, the potential V_{OCP} obtained after prolonged equilibration at open circuit ($+0.2$ V vs Ag/AgCl/saturated KCl, $+0.4$ V vs NHE). However, at the most negative applied potentials, in particular at $\Delta V = -0.5$ V, reduction of the oxidized surface may have started to occur. In summary, faradaic currents were expected especially at the extremes of the experimental potential range, at $\Delta V = -0.5$ V and $\Delta V = +0.5$ V.

The measured capacitances confirmed that faradaic processes mainly took place at -0.5 V and $+0.5$ V. At those potentials, more charge was measured during charging than just afterwards, during discharging, see Fig. 5.4. For the other charging potentials, practically the same capacitances were calculated from the charges measured during charging and during discharging. In units of $\mu\text{F cm}^{-2}$, the capacitances in Fig. 4 are similar to those reported by Finney et al. [131] for highly oriented pyrolytic graphite (HOPG) in 1 M NaCl;

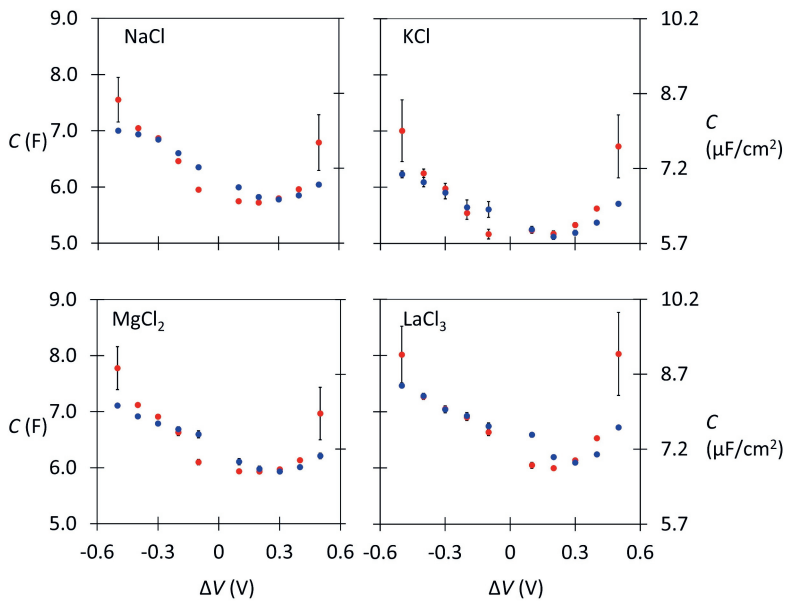


Figure 5.4: Average capacitance C [Eq. (5.3)], as a function of applied potential, for measurements in 1 M NaCl, KCl, MgCl_2 , and LaCl_3 . The red symbols indicate values calculated from transients measured upon charging and the blue symbols indicate the values upon discharging.

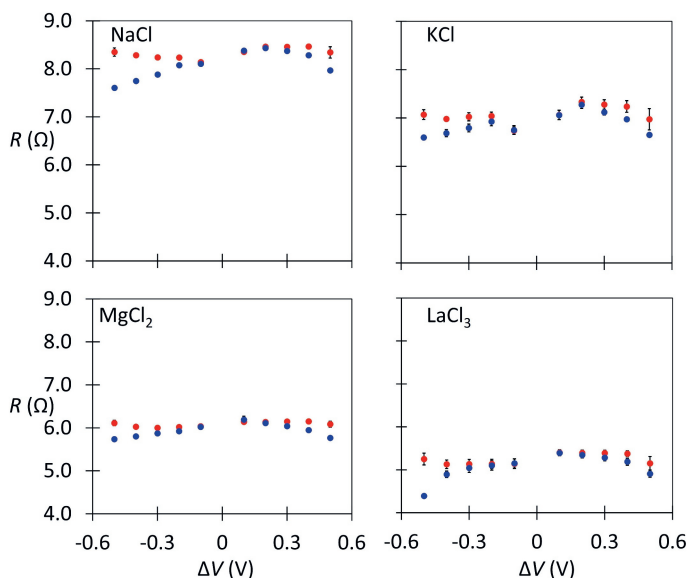


Figure 5.5: (a) Average resistance R [Eq. (5.2)] as a function of applied potential, for measurements in 1 M NaCl, KCl, MgCl_2 , and LaCl_3 . The red symbols indicate values calculated from transients measured upon charging and the blue symbols indicate the values upon discharging.

their molecular dynamics simulations also revealed a higher capacitance in the cathodic range ($7 \mu\text{F cm}^{-2}$) than in the anodic range ($5 \mu\text{F cm}^{-2}$), which they explained in terms of Na^+ adsorption in the cathodic range. It is noted that in our experiments, the electrical double layer has less space to develop than at a single flat electrode and that the 88 m^2 that we determined as the surface area of our electrodes depends on the analysis of nitrogen physisorption experiments (see section 3.9) and an assumption about the active part of our electrode, delimited by a rubber O-ring that presses against it (see Chapter 2).

Figure 5.5 reveals that the measured resistance [Eq. (5.2)] appears to be constant during charging, with slightly different values in the cathodic and anodic ranges, whereas the resistance is slightly lower during discharging after charging at increasingly negative or positive potentials. Our tentative explanation is that adsorbed ions or the electronic charges accumulated at the carbon surface contribute to a surface conductivity. At the start of discharging, the amount of ions in the pores is not only given by the ions in the initially neutral salt solution inside the pores, but also many ions are adsorbed to the carbon

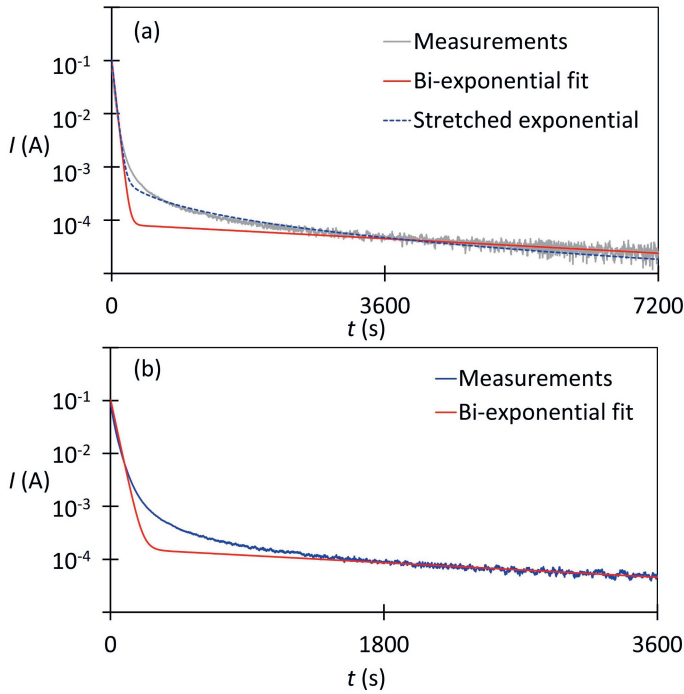


Figure 5.6: Current transient measured upon charging a porous carbon electrode at $\Delta V = 0.5$ V in a 1 M solution of LaCl_3 . (a) Measurement until $t_{\text{final}} = 7200$ s. Bi-exponential fit [Eq. (5.1)] yielded $I_1 = 103$ mA and $\tau_1 = 34$ s and (in the range from 5100 to 6700 s) $I_2 = 95 \pm 5$ μA and $\tau_2 = 5000 \pm 200$ s ($I_{\text{final}} = 24$ μA). For comparison, the second part of the transient was also fitted using a stretched exponential function, see Eq. (5.6) ($I_s = 2.7$ mA, $\tau_s = 34$ s, $\beta = 0.3$). (b) First half of the transient in (a). Fitting in the range from 2100 to 3100 s now yielded $I_2 = 163 \pm 4$ μA and $\tau_2 = 2780 \pm 60$ s ($I_{\text{final}} = 49$ μA).

surface, the more so the higher the negative or positive value of ΔV that was applied during charging. If the adsorbed ions are mobile, or if the surface conductivity is affected by the electronic surface charges in the carbon, this may explain the lowered resistance measured during discharging.

5.4.2 Bi-exponential versus stretched exponential fitting

Typical bi-exponential fits of a measured transient to Eq. (5.1) are shown in Figs. 5.6a and 5.6b. Reasonably good fits are obtained of the initial and final parts of the transient, although at intermediate times, the fits underestimate the measurements. Figures 5.6a and 5.6b show the analysis of the same data,

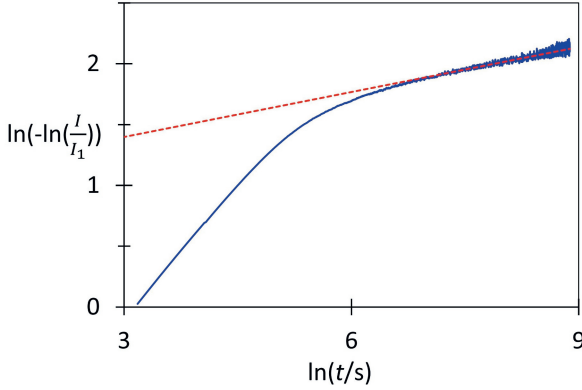


Figure 5.7: Plot of the data from Fig. 5.6a as $\ln[-\ln(I/I_1)]$ versus $\ln(t/s)$, which should give a straight line with slope β in the case of decay described by a single stretched exponential function, see Eq. (5.5).

but whereas the transient in Fig. 5.6a ends at $t_{\text{final}} = 7200$ s, only the first 3600 s are examined in Fig. 5.6b. The fit results for the initial part of the curve are the same in both cases, since they depend on the peak value of the current ($I_{\text{peak}} \approx I_1$) and the integral charge, which is nearly the same in both cases ($\tau = RC \approx Q_{\text{eq}}/I_{\text{peak}}$). The values of I_2 and τ_2 , however, depend on the time range where these parameters are determined from the fitting of $\ln(I)$ versus t . The fit in Fig. 5.6b gives a value of I_2 that is about twice that in Fig. 5.6a, whereas the fitted value of τ_2 is about half of that in Fig. 5.6a. In both Figs. 5.6a and 5.6b, it appears like the semi-logarithmic plot of I versus t reaches a limiting slope in the final part of the transient, but this is clearly an illusion, since different final slopes are attained in the two figures. This indicates that the current decay is not precisely bi-exponential, but that the determined time constant τ_2 increased as time progressed.

The measured transients did not correspond to a single stretched exponential decay function as described by Eq. (5.5). Plots of $\ln[-\ln(I/I_1)]$ versus $\ln(t/s)$ gave a straight line only at $t > 1000$ s, see Fig. 5.7, indicating that only this part of the transients could be described by a stretched exponential function. Fits to Eq. (5.6), describing process 1 as in Eq. (5.1) and process 2 with a stretched exponential function, did give a much better description of the whole transient than Eq. (5.1), see Fig. 5.6a. Nevertheless, fitting to Eq.(5.1) had the advantage of giving one time constant for the charging process at

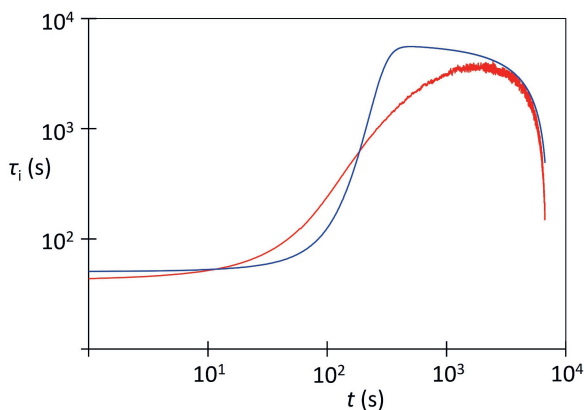


Figure 5.8: Red curve: instantaneous time constant analysis via Eq. (5.8) of the measured current transient in Fig. 5.6a. Blue curve: analysis of the bi-exponential fit to the data.

short times (τ_1) and a second time constant (τ_2) that describes the dynamics in the time range where τ_2 is determined, for instance around $t = 2500$ s for measurements of an hour as in Fig. 5.6b. This was used to compare between measurements at different applied potentials and with different salts.

5.4.3 Instantaneous time constant analysis

In addition to bi-exponential fitting, instantaneous time constant analysis was performed [Eq. (5.8)], see Fig. 5.8. The general shape of the curve was as expected from Fig. 5.2b. The value of $\tau_i(t)$ started out at a low value corresponding to RC' , then gradually rose to a maximum value, after which it rapidly decreased toward zero near the end of the measurement. For comparison, the $\tau_i(t)$ curves corresponding to the bi-exponential fits to Eq. (5.1) showed a steeper increase and better defined plateau. This suggests that the measured current transients correspond to a distribution of time constants, as can be described using a stretched exponential term [Eq. (5.6)], rather than bi-exponential decay. The obtained maximum values of $\tau_i(t)$ were of similar magnitude as obtained by fitting to Eq. (5.1).

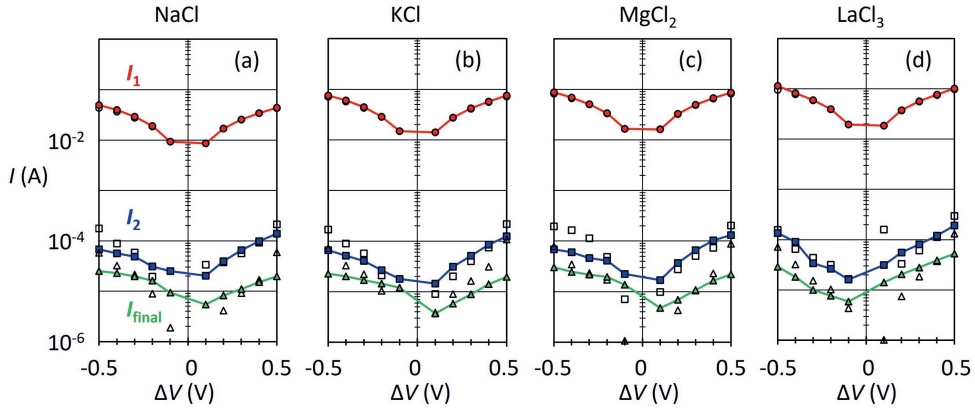


Figure 5.9: Results of bi-exponential fitting [Eq. (5.1)] of the absolute current transients measured during charging (open uncolored symbols) and discharging (closed colored symbols) of microporous carbon electrodes in aqueous solutions of (a-d) 1 M NaCl, 1 M KCl, 1 M MgCl_2 , and 1 M LaCl_3 . The characteristic currents I_1 and I_2 [Eq. (5.1)] and I_{final} (Fig. 5.1) are shown.

5.4.4 Comparison of results for different salt solutions

The characteristic currents I_1 , I_2 , and I_{final} (see Fig. 5.1) are shown as a function of applied potential in Fig. 5.9 for 1 M solutions of NaCl, KCl, MgCl_2 , and LaCl_3 . In general, the values of I_1 reflect the fact that the resistance of each system was approximately constant, so that the peak current increased linearly with applied potential [Eq. (5.2)]. The values of I_1 were the lowest for 1 M NaCl and the highest for 1 M LaCl_3 , in line with Eq. (5.2) and the electrical conductivities of the solutions. The relative values of I_2 had more or less the same potential dependence as I_1 but were lower by three orders of magnitude. The final measured currents I_{final} were even lower, by another order of magnitude.

Figure 5.10 presents the potential dependence of three time constants extracted from the same current transients as analyzed in Fig. 5.9. In all cases, the RC time constant, τ_1 , was approximately independent of the applied potential. This agrees with $RC \approx Q_{\text{eq}}/I_{\text{peak}}$ and the fact that the current decay was largely exponential, so that the integral value Q_{eq} scaled with peak value I_{peak} . Considered in another way, the potential independence of τ_1 agrees with a constant conductivity of the initially neutral electrolyte solution in the pores and an approximately constant C , neglecting the difference between cathodic

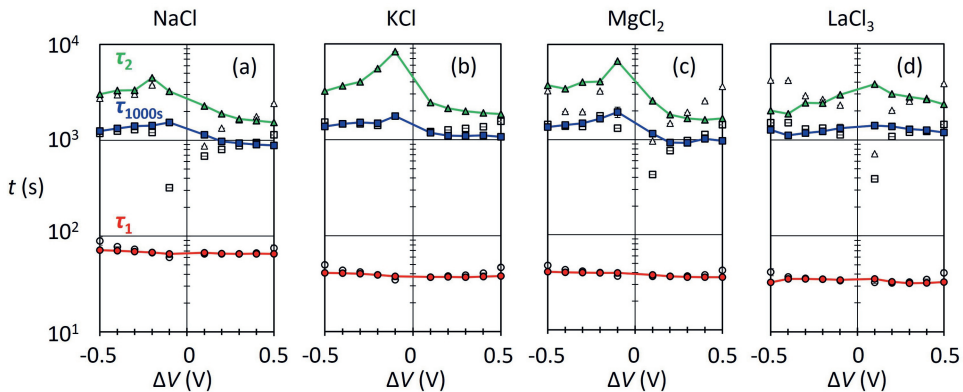


Figure 5.10: Results of analysis of the characteristic time constants τ_1 and τ_2 [Eq. (5.1)] and the instantaneous time constant at $t = 1000$ s [Eq. (5.8)] during charging (open uncolored symbols) and discharging (closed colored symbols) of (a-d) 1 M NaCl, 1 M KCl, 1 M MgCl_2 , and 1 M LaCl_3 . In all cases, only the first 3600 s of measurements were analyzed.

and anodic capacitance found earlier (Fig. 5.4). In Chapter 3, we calculated that the capacitance C of our electrodes is of the same order of magnitude as a parallel plate capacitor with the internal surface area of the electrodes, a plate-to-plate distance equal to the size of a water molecule, and the experimental dielectric constant of water when it was measured between two conductive plates 1 nm apart [75]. In Chapter 2, we calculated that in our measurements, the concentration-dependent part of the measured resistance R is dominated by the resistance of the electrolyte solution between the working electrode and the Luggin tube containing the reference electrode, as was also found in Ref. [111]. The RC time for 1 M NaCl was relatively high, in line with the lower conductivity of 1 M NaCl solution, compared to that of the other salt solutions.

The late-time decay constants $\tau_i(t = 1000 \text{ s})$ and τ_2 shown in Fig. 5.10 are higher than τ_1 by about two orders of magnitude, on the order of at least 1000 s. These characteristic times are much longer than the time that the ions would take to diffuse across 0.25 mm of bulk electrolyte solution, where 0.25 mm is the thickness of the electrode and $(0.25 \text{ mm})^2 / (2D) \sim 20 \text{ s}$, assuming $D \sim 2 \times 10^{-9} \text{ m}^2 \text{ s}^{-1}$ [78]. The slowdown is probably due in part to the slowdown of ionic diffusion under confinement [122] and in part to the tortuosity [132] of

the porous network. Moreover, the experimental molar conductivity of LaCl_3 solutions is lower by about a factor of 3 at 1 M concentration than at high dilution [133], and the molar conductivity of NaCl solutions is about 30% lower at 1 M than at high dilution [57], implying lower diffusion coefficients of the ions.

The characteristic time of the late-time process appears longer in the cathodic range than in the anodic range, at least in the cases of 1 M NaCl , 1 M KCl , and 1 M MgCl_2 , whereas it appears potential-independent for 1 M LaCl_3 . In the cases of NaCl and MgCl_2 , the limiting diffusion coefficients of the cations (Na^+ : $1.33 \times 10^{-9} \text{ m}^2\text{s}^{-1}$; Mg^{2+} : $1.41 \times 10^{-9} \text{ m}^2\text{s}^{-1}$) are lower than those of the anions (Cl^- : $1.97 \times 10^{-9} \text{ m}^2\text{s}^{-1}$), whereas both in KCl and in LaCl_3 , the limiting diffusion coefficients of the cations (K^+ : $1.89 \times 10^{-9} \text{ m}^2\text{s}^{-1}$; La^{3+} : $1.86 \times 10^{-9} \text{ m}^2\text{s}^{-1}$) are similar to those of the anions. In other words, the diffusion coefficients of the counterions do not seem to account for the difference between late-time cathodic and anodic charging dynamics. At small applied potentials ($\pm 0.1 \text{ V}$ or $\pm 0.2 \text{ V}$) a weak faradaic current may cause the current transients to flatten off (see Fig. 5.2a), which may explain part of the rise in τ_1 (1000 s) and (τ_2) at ΔV close to 0 V. But this does not suffice to explain the differences between the late-time charging and discharging rates (see Sec. 5.6 for examples of current transients for the four salts) and the cathodic and anodic discharging rates at higher applied potentials.

Our tentative explanation is as follows. Initially, the applied potential falls across the electrolyte solution, and the (dis)charging rate is determined by the total RC time, depending on the conductivity of the neutral electrolyte solution and the initial capacitance of the electrode. As charging progresses, the electrical double layer at the widest pores charges up the most rapidly, leading to a relatively rapid drop in electric field in the electrolyte solution in the widest pores. In the smaller pores, however, double layer charging lags behind. Their charging rate depends on the local RC time, which is relatively high for three reasons: confinement [122], a decrease in local ionic concentration because of counterion ion adsorption, and an increase in local capacitance, because of specific ion adsorption [131]. Since the measured capacitance is higher in the cathodic than in the anodic range, also the local RC time at any time in the transient is higher, and the local electric fields and

currents do not decay as rapidly as in the anodic range. Moreover, a difference in dynamics between charging and discharging could then originate from a difference in the time-dependent local capacitance of the surface, corresponding to a counterion-covered surface near the end of charging and to a bare carbon surface near the end of discharging.

5.5 Conclusion

Current transients were measured during the potentiostatic charging of porous carbon electrodes in NaCl, KCl, MgCl₂, and LaCl₃ solutions. To characterize the dynamics, characteristic time constants were extracted from the data, both at cathodic and anodic potentials. At early times in the transients, the dynamics were set by the RC time. Later in the transients, the time constant that characterized the exponential decay of the current was time-dependent, presumably because the (dis)charging rate was due to a distribution of time constants, related to the polydispersity of the pores. Although the late-time (dis)charging dynamics were observed to be slower in the cathodic than in the anodic range, this is difficult to explain in terms of differences in the diffusion coefficients of the ions, considering the fact that the limiting diffusion coefficients of K⁺ and Cl⁻ are nearly equal. We proposed a tentative explanation that takes into account the polydispersity of the pores, the effect of pore size on ionic transport rate, and the effect of specific ion adsorption on the capacitance. The measured capacitance was higher in the cathodic than in the anodic range, which was ascribed to specific ion adsorption. In the transmission line of local RC elements representing individual pores, changes in ion coverage could imply different local RC times, resulting in different rates of late-time charging in the cathodic and anodic ranges as well as upon charging and discharging. In the future, theoretical work might be performed to support or to invalidate this explanation.

5.6 Appendix 1: Figures with current transients during charging and discharging

The following figures show typical current transients upon charging and discharging.

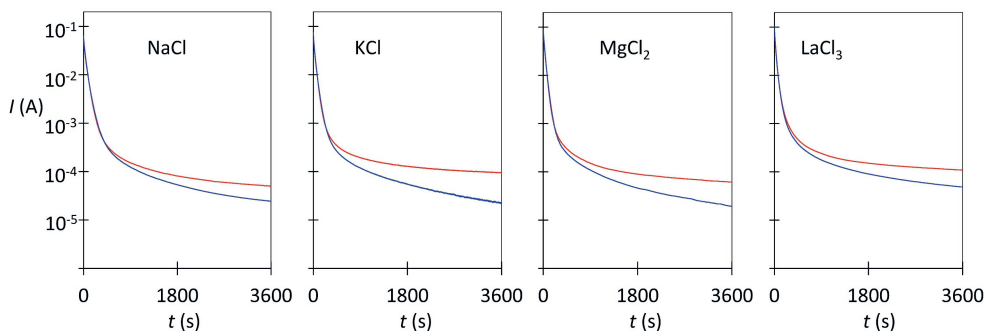


Figure 5.11: Current transients upon charging (red, top curves) at $\Delta V = +0.5$ V and discharging (blue, bottom curves) at $\Delta V = 0$ V, for a porous carbon electrode in 1 M concentrations of NaCl, KCl, MgCl_2 , and LaCl_3 .

Chapter 6

Summary / Samenvatting

6.1 Summary

Porous carbon electrodes are used in applications such as supercapacitors and capacitive deionization (CDI). When the electrodes are submerged in an aqueous electrolyte solution and charged, an electrical double layer (EDL) forms. Much of the experimental information about the EDL comes from electrical measurements of the amount of electronic charge. However, the heat released during (dis)charging the electrode also contains valuable information, about the thermodynamics of the EDL. For this thesis, we built a calorimetry setup to measure the heat as a function of the applied potential. We aimed to gain insight into the EDL by finding an explanation for the origin of the heat.

Chapter 1 contains an overview of the background of this thesis. Porous carbon electrodes and their applications are introduced, followed by a discussion of the EDL in porous carbon electrodes. Then, experimental work on the thermodynamics of the EDL in porous electrodes is presented. This Chapter ends with a brief description of the electrochemical calorimetry setup.

In Chapter 2, the electrochemical calorimetry setup is examined in more detail. The cell contained an aqueous electrolyte solution and three electrodes. The potential of the working electrode (WE) was applied with respect to the reference electrode (RE), and the current was measured between WE and counter electrode (CE). Behind the WE, a heat flux sensor (HFS) measured the heat flow coming from the WE during the (dis)charging of the EDL. The heat was calibrated on the Joule heat produced in a full charge-discharge cycle. Having built this setup, we were ready to measure the heat of (dis)charging the WE as a function of the potential applied to the electrode, allowing separation between anodic and cathodic heat effects.

Chapter 3 describes how the setup was used to determine the potential-dependent internal energy of porous carbon electrodes in aqueous solutions of different salts. Changes in the energy were calculated from the (electrical) work performed on the system and the heat released or absorbed by the system. The energy changes were found to consist of two contributions, which respectively scaled linearly and quadratically with applied potential. The linear contribution was ascribed to the attraction of ions to the surface of the pores, given by the number of adsorbed ions times a fixed attraction energy per ion. The quadratic contribution was slightly smaller than expected for a

parallel plate capacitor of the same capacitance, which we interpreted in terms of the average electric potential experienced by ions inside the pores.

Chapter 4 demonstrated that the same formula for the internal energy as found in Chapter 3 can also explain the time-dependent heat production. The charging rate was varied by changing the amount of time taken to build up the applied potential linearly until the final potential ΔV was reached. Using four constant parameters, capacitance C , resistance R , and f and ΔV_{att} as determined in Chapter 3, both the reversible and irreversible heat production rates could be explained. We verified that the reversible heat was the same regardless of the charging rate. Agreement between model and experiment was only semi-quantitative, which we attributed to a time dependence of the electric current that is more complicated than mono-exponential decay in the case of abrupt application of the cell potential.

In Chapter 5 we analyzed the time dependence of the current for the (dis)charging of porous carbon electrodes in 1 M NaCl, KCl, MgCl₂, and LaCl₃. The rate of exponential decay of the current was initially determined by the RC time and later by a distribution of time constants, which we attributed to polydispersity of the pores. The late-time current decay was slower at cathodic than at anodic potentials, but we argued that this was not because of the different diffusion coefficients of the cations and anions, which were nearly identical for KCl. Instead, the potential-dependent dynamics were discussed in terms of the different capacitance of the electrode in the cathodic and anodic ranges, resulting from specific ion adsorption.

In conclusion, this thesis describes new measurements of the potential-dependent heat production of porous carbon electrodes in aqueous salt solutions and provides an explanation for the reversible and the irreversible heats on the basis of the internal energy change of the electrical double layer inside the pores. Our description of the energy as an explicit function of the electric potential drop across the double layer also enables an explanation of the complicated time dependence of heat production as a function of applied potential and charging rate. In other words, the objective of giving new insight into the electrical double layer of porous capacitive electrodes on the basis of calorimetric measurements was achieved.

6.2 Samenvatting

Poreuze koolstofelektroden hebben verschillende toepassingen, bijvoorbeeld in supercondensatoren en capacitieve deïonisatie (CDI). Als de elektroden in een waterige elektrolietoplossing worden geplaatst en opgeladen, ontstaat er een elektrische dubbellaag (EDL). Veel van de experimentele informatie over deze EDL komt van elektrische metingen van de elektronische lading in het systeem. Echter, de warmte die vrijkomt tijdens het op- en ontladen bevat ook waardevolle informatie, over de thermodynamische eigenschappen van de EDL. Voor deze thesis hebben we een calorimetrische opstelling gebouwd die gebruikt kan worden om deze warmte als een functie van de aangelegde elektrische potentiaal te meten. Het doel was om nieuw inzicht te krijgen in de EDL door een verklaring te vinden voor de oorsprong van de warmte.

Hoofdstuk 1 geeft een overzicht van de achtergrond van dit proefschrift. Poreuze koolstofelektroden en hun toepassingen worden geïntroduceerd, waarna de rol van de EDL in poreuze koolstofelektroden wordt besproken. Vervolgens wordt het experimentele werk met betrekking tot de thermodynamische eigenschappen gepresenteerd. Dit hoofdstuk eindigt met een korte beschrijving van de gebruikte elektrochemische calorimetrische opstelling.

In hoofdstuk 2 wordt de elektrochemische calorimetrische opstelling in detail besproken. De cel bevatte een waterige elektrolietoplossing en drie elektroden. De elektrische potentiaal van de werkelektrode (WE) werd aangelegd ten opzichte van een referentie-elektrode (RE), en de stroom werd gemeten tussen de WE en de tegenelektrode (CE). Achter de WE was een warmtestroomsensor (HFS) geplaatst, die de warmtestroom tijdens het op- en ontladen van de WE mat. De warmte werd gekalibreerd aan de hand van de Joulewarmte die geproduceerd werd tijdens een volledige cyclus van op- en ontladen. Met deze opstelling konden we de warmte tijdens op- en ontladen van de WE als een functie van de aangelegde potentiaal meten, wat het scheiden van anodische en kathodische warmte mogelijk maakte.

Hoofdstuk 3 beschrijft hoe de opstelling gebruikt werd om de elektrische potentiaal-onafhankelijke inwendige energie, van poreuze koolstofelektroden in verschillende waterige zoutoplossingen, te bepalen. Veranderingen in de inwendige energie werden berekend uit de uitgevoerde (elektrische) arbeid op het systeem en de warmte vrijgekomen van, of opgenomen door het sys-

teem. De veranderingen bleken uit twee bijdragen te bestaan, welke respectievelijk lineair, danwel kwadratisch schaalden met de verandering in de aangelegde elektrische potentiaal. De lineaire bijdrage werd toegeschreven aan de aantrekkingskracht van ionen naar het oppervlak van de poriën, gegeven door het aantal geadsorbeerde ionen maal een bepaalde aantrekkingsenergie per ion. De kwadratische bijdrage was kleiner dan verwacht voor een klassieke vlakke plaat condensator, wat we verklaarden in termen van de gemiddelde elektrische potentiaal die 'gevoeld' werd door ionen in de poriën.

Hoofdstuk 4 liet zien dat de formule voor de inwendige energie, zoals beschreven in hoofdstuk 3, ook gebruikt kan worden om de tijdsafhankelijke warmteproductie te verklaren. De oplaadsnelheid werd gevarieerd door te veranderen hoeveel tijd werd genomen om de aangelegde spanning lineair op te bouwen naar een eindwaarde. Door vier constante parameters te gebruiken, te weten de elektrische capaciteit C , de weerstand R , en f en ΔV_{att} zoals bepaald in Hoofdstuk 3, konden we zowel de reversibele als de irreversibele warmteproductie beschrijven. We lieten zien dat de reversibele warmte constant was, onafhankelijk van de oplaadsnelheid. De overeenstemming tussen theorie en experiment was slechts semikwantitatief, wat we toewezen aan een tijdsafhankelijkheid van de elektrische stroom die ingewikkelder is dan een mono-exponentieel verval in het geval van het abrupt aanleggen van de elektrische celpotentiaal.

In hoofdstuk 5 analyseerden we de tijdsafhankelijkheid van de stroom voor het op- en ontladen van poreuze koolstofelektroden in 1 M NaCl, KCl, MgCl_2 en LaCl_3 . De snelheid van het exponentiële verval werd in eerste instantie gekarakteriseerd door de RC tijd. Later werd deze gekarakteriseerd door een verdeling van tijdsconstanten, wat we toeschreven aan de polydispersiteit van de poriën. Het verval van de stroom tegen het einde was langzamer bij kathodische elektrische potentialen dan bij anodische, maar we beargumenteren dat dit niet werd veroorzaakt door verschillende diffusiecoëfficiënten van de kationen en anionen, aangezien deze vrijwel gelijk zijn in het geval van KCl, althans bij hoge verdunning. In plaats daarvan bediscussieerden we de elektrische potentiaalafhankelijke dynamiek op basis van de verschillende elektrische capaciteiten in kathodisch en anodisch gebied, wat een gevolg is van specifieke ionadsorptie.

Ter conclusie, deze thesis beschrijft nieuwe metingen van de elektrische potentiaalafhankelijke warmteproductie van poreuze koolstofelektroden en geeft een verklaring voor de reversibele en irreversibele warmte, op basis van de inwendige energieverandering van de elektrische dubbellaag in de poriën. Onze beschrijving van de energie als een functie van het elektrische potentiaalverval over de dubbellaag verklaart de ingewikkelde tijdsafhankelijkheid van de warmteproductie, als een functie van de aangelegde elektrische potentiaal en oplaadsnelheid. In andere woorden, het doel om nieuwe inzichten te geven in de elektrische dubbellaag in poreuze koolstofelektroden, aan de hand van calorimetrische metingen, is behaald.

Bibliography

- [1] M. Janssen, E. Griffioen, P. M. Biesheuvel, R. Van Roij, and B. Ern , “Coulometry and calorimetry of electric double layer formation in porous electrodes,” *Phys. Rev. Lett.*, vol. 119, no. 16, 2017, Art. no. 166002.
- [2] S. Manocha, “Porous carbons,” *Sadhana*, vol. 28, no. 1, pp. 335–348, 2003.
- [3] Z. Zhai, L. Zhang, T. Du, B. Ren, Y. Xu, S. Wang, J. Miao, and Z. Liu, “A review of carbon materials for supercapacitors,” *Mater. Des.*, vol. 221, 2022, Art. no. 111017.
- [4] Q. Zhu, D. Zhao, M. Cheng, J. Zhou, K. A. Owusu, L. Mai, and Y. Yu, “A new view of supercapacitors: Integrated supercapacitors,” *Adv. Energy Mater.*, vol. 9, no. 36, p. 1901081, 2019.
- [5] M. Salanne, B. Rotenberg, K. Naoi, K. Kaneko, P.-L. Taberna, C. P. Grey, B. Dunn, and P. Simon, “Efficient storage mechanisms for building better supercapacitors,” *Nat. Energy*, vol. 1, no. 6, 2016, Art. no. 16070.
- [6] M. R. Lukatskaya, B. Dunn, and Y. Gogotsi, “Multidimensional materials and device architectures for future hybrid energy storage,” *Nat. Comm.*, vol. 7, 2016, Art. no. 12647.
- [7] Q. Xun and Y. Liu, “Evaluation of fluctuating voltage topology with fuel cells and supercapacitors for automotive applications,” *Int. J. Energy Res.*, vol. 43, no. 9, pp. 4807–4819, 2019.
- [8] J. Libich, J. M ca, J. Vondr k, O.  ech, and M. Sedla rkov , “Supercapacitors: Properties and applications,” *J. Energy Storage*, vol. 17, pp. 224–227, 2018.
- [9] L. Wang, Y. Zhang, K. Moh, and V. Presser, “From capacitive deionization to desalination batteries and desalination fuel cells,” *Curr. Opin. Electrochem.*, vol. 29, 2021, Art. no. 100758.

- [10] S. Porada, L. Weinstein, R. Dash, A. Van Der Wal, M. Bryjak, Y. Gogotsi, and P. M. Biesheuvel, “Water desalination using capacitive deionization with microporous carbon electrodes,” *ACS Appl. Mater. Interf.*, vol. 4, no. 3, pp. 1194–1199, 2012.
- [11] S. Porada, L. Borchardt, M. Oschatz, M. Bryjak, J. S. Atchison, K. J. Keesman, S. Kaskel, P. M. Biesheuvel, and V. Presser, “Direct prediction of the desalination performance of porous carbon electrodes for capacitive deionization,” *Energy Environ. Sci.*, vol. 6, no. 12, pp. 3700–3712, 2013.
- [12] M. Salehi, “Global water shortage and potable water safety; Today’s concern and tomorrow’s crisis,” *Environ. Int.*, vol. 158, 2022, Art. no. 106936.
- [13] S. Porada, R. Zhao, A. Van Der Wal, V. Presser, and P. M. Biesheuvel, “Review on the science and technology of water desalination by capacitive deionization,” *Prog. Mater. Sci.*, vol. 58, no. 8, pp. 1388–1442, 2013.
- [14] P. M. Biesheuvel, S. Porada, M. Levi, and M. Z. Bazant, “Attractive forces in microporous carbon electrodes for capacitive deionization,” *J. Solid State Electr.*, vol. 18, no. 5, pp. 1365–1376, 2014.
- [15] L. Wang, P. M. Biesheuvel, and S. Lin, “Reversible thermodynamic cycle analysis for capacitive deionization with modified Donnan model,” *J. Colloid Interface Sci.*, vol. 512, pp. 522–528, 2018.
- [16] J. Paredes, A. Martínez-Alonso, P.-X. Hou, T. Kyotani, and J. Tascón, “Imaging the structure and porosity of active carbons by scanning tunneling microscopy,” *Carbon*, vol. 44, no. 12, pp. 2469–2478, 2006.
- [17] D. Brogioli, R. Zhao, and P. M. Biesheuvel, “A prototype cell for extracting energy from a water salinity difference by means of double layer expansion in nanoporous carbon electrodes,” *Energy Environ. Sci.*, vol. 4, pp. 772–777, 2011.
- [18] R. Zhao, P. M. Biesheuvel, H. Miedema, H. Bruning, and A. van der Wal, “Charge efficiency: A functional tool to probe the double-layer

- structure inside of porous electrodes and application in the modeling of capacitive deionization,” *J. Phys. Chem. Lett.*, vol. 1, no. 1, pp. 205–210, 2009.
- [19] J. Chmiola, G. Yushin, Y. Gogotsi, C. Portet, P. Simon, and P. L. Taberna, “Anomalous increase in carbon at pore sizes less than 1 nanometer,” *Science*, vol. 313, no. 5794, pp. 1760–1763, 2006.
- [20] J. Chmiola, C. Largeot, P.-L. Taberna, P. Simon, and Y. Gogotsi, “Desolvation of ions in subnanometer pores and its effect on capacitance and double-layer theory,” *Angew. Chem. Int. Ed.*, vol. 47, no. 18, pp. 3392–3395, 2008.
- [21] Z.-X. Luo, Y.-Z. Xing, S. Liu, Y. C. Ling, A. Kleinhammes, and Y. Wu, “Dehydration of ions in voltage-gated carbon nanopores observed by in situ NMR,” *J. Phys. Chem. Lett.*, vol. 6, no. 24, pp. 5022–5026, 2015.
- [22] C. Prehal, C. Koczwar, N. Jäckel, A. Schreiber, M. Burian, H. Amenitsch, M. A. Hartmann, V. Presser, and O. Paris, “Quantification of ion confinement and desolvation in nanoporous carbon supercapacitors with modelling and *in situ* X-ray scattering,” *Nat. Energy*, vol. 2, no. 3, p. 16215, 2017.
- [23] R. Schuster, “Electrochemical microcalorimetry at single electrodes,” *Curr. Opin. Electrochem.*, vol. 1, no. 1, pp. 88–94, 2017.
- [24] Y. Dandeville, P. Guillemet, Y. Scudeller, O. Crosnier, L. Athouel, and T. Brousse, “Measuring time-dependent heat profiles of aqueous electrochemical capacitors under cycling,” *Thermochim. Acta*, vol. 526, no. 1-2, pp. 1–8, 2011.
- [25] X. Zhang, W. Wang, J. Lu, L. Hua, and J. Heng, “Reversible heat of electric double-layer capacitors during galvanostatic charging and discharging cycles,” *Thermochim. Acta*, vol. 636, pp. 1–10, 2016.
- [26] A. Likitchatchawankun, G. Whang, J. Lau, O. Munteshari, B. Dunn, and L. Pilon, “Effect of temperature on irreversible and reversible heat generation rates in ionic liquid-based electric double layer capacitors,” *Electrochim. Acta*, vol. 338, p. 135802, 2020.

- [27] A. Kundu, L. Pilon, and T. S. Fisher, “A continuum model of heat transfer in electrical double-layer capacitors with porous electrodes under constant-current cycling,” *J. Power Sources*, vol. 511, 2021, Art. no. 230404.
- [28] J. Schiffer, D. Linzen, and D. U. Sauer, “Heat generation in double layer capacitors,” *J. Power Sources*, vol. 160, no. 1, pp. 765–772, 2006.
- [29] O. Munteshari, J. Lau, A. Krishnan, B. Dunn, and L. Pilon, “Isothermal calorimeter for measurements of time-dependent heat generation rate in individual supercapacitor electrodes,” *J. Power Sources*, vol. 374, pp. 257–268, 2018.
- [30] C. Lian, M. Janssen, H. Liu, and R. Van Roij, “Blessing and curse: How a supercapacitor’s large capacitance causes its slow charging,” *Phys. Rev. Lett.*, vol. 124, no. 7, 2020, Art. no. 076001.
- [31] M. Janssen and R. van Roij, “Reversible heating in electric double layer capacitors,” *Phys. Rev. Lett.*, vol. 118, 2017, Art. no. 096001.
- [32] F. Glatzel, M. Janssen, and A. Härtel, “Reversible heat production during electric double layer buildup depends sensitively on the electrolyte and its reservoir,” *J. Chem. Phys.*, vol. 154, 2021, Art. no. 064901.
- [33] A. D’Entremont and L. Pilon, “First-principles thermal modeling of electric double layer capacitors under constant-current cycling,” *J. Power Sources*, vol. 246, pp. 887–898, 2014.
- [34] A. L. D’Entremont and L. Pilon, “Thermal effects of asymmetric electrolytes in electric double layer capacitors,” *J. Power Sources*, vol. 273, pp. 196–209, 2015.
- [35] P. Simon and Y. Gogotsi, “Perspectives for electrochemical capacitors and related devices,” *Nat. Mater.*, vol. 19, no. 11, pp. 1151–1163, 2020.
- [36] T. Kim, J. E. Dykstra, S. Porada, A. van der Wal, J. Yoon, and P. M. Biesheuvel, “Enhanced charge efficiency and reduced energy use in capacitive deionization by increasing the discharge voltage,” *J. Coll. Interf. Sci.*, vol. 446, pp. 317–326, 2015.

-
- [37] A. C. Forse, C. Merlet, J. M. Griffin, and C. P. Grey, “New perspectives on the charging mechanisms of supercapacitors,” *J. Am. Chem. Soc.*, vol. 138, no. 18, pp. 5731–5744, 2016.
- [38] J. M. Griffin, A. C. Forse, W.-Y. Tsai, P.-L. Taberna, P. Simon, and C. P. Grey, “*In situ* NMR and electrochemical quartz crystal microbalance techniques reveal the structure of the electrical double layer in supercapacitors,” *Nat. Mater.*, vol. 14, no. 8, pp. 812–819, 2015.
- [39] A. C. Forse, J. M. Griffin, C. Merlet, P. M. Bayley, H. Wang, P. Simon, and C. P. Grey, “NMR Study of Ion Dynamics and Charge Storage in Ionic Liquid Supercapacitors,” *J. Am. Chem. Soc.*, vol. 137, no. 22, pp. 7231–7242, 2015.
- [40] H. Wang, A. C. Forse, J. M. Griffin, N. M. Trease, L. Trognko, P.-L. Taberna, P. Simon, and C. P. Grey, “In situ NMR spectroscopy of supercapacitors: Insight into the charge storage mechanism,” *J. Am. Chem. Soc.*, vol. 135, no. 50, pp. 18 968–18 980, 2013.
- [41] F. W. Richey, B. Dyatkin, Y. Gogotsi, and Y. A. Elabd, “Ion dynamics in porous carbon electrodes in supercapacitors using in situ infrared spectroelectrochemistry,” *J. Am. Chem. Soc.*, vol. 135, pp. 12 818–12 826, 2013.
- [42] F. W. Richey, C. Tran, V. Kalra, and Y. A. Elabd, “Ionic liquid dynamics in nanoporous carbon nanofibers in supercapacitors measured with in operando infrared spectroelectrochemistry,” *J. Phys. Chem. C.*, vol. 118, no. 38, pp. 21 846–21 855, 2014.
- [43] S. Boukhalfa, L. He, Y. B. Melnichenko, and G. Yushin, “Small-angle neutron scattering for in situ probing of ion adsorption inside micropores,” *Angew. Chem. Int. Ed.*, vol. 52, no. 17, pp. 4618–4622, 2013.
- [44] S. Boukhalfa, D. Gordon, L. He, Y. B. Melnichenko, N. Nitta, A. Magasinski, and G. Yushin, “*In Situ* small angle neutron scattering revealing ion sorption in microporous carbon electrical double layer capacitors,” *ACS nano*, vol. 8, no. 3, p. 2495–2503, 2014.

- [45] U. Narger, M. E. Hayden, J. L. Booth, W. N. Hardy, L. A. Whitehead, J. F. Carolan, D. A. Balzarini, E. H. Wishnow, and C. C. Blake, “High precision calorimetric apparatus for studying electrolysis reactions,” *Rev. Sci. Instrum.*, vol. 61, no. 5, 1990, Art. no. 1504.
- [46] L. D. Hansen, R. H. Hart, D. M. Chen, and H. F. Gibbard, “High-temperature battery calorimeter,” *Rev. Sci. Instrum.*, vol. 53, no. 4, 1982, Art. no. 503.
- [47] B. C. Chen, C. Y. Ho, Y. H. Tsai, Y. C. Lee, and M. Y. Wen, “Analysis of electrical heating in hollow carbon nanoparticles as supercapacitor electrodes for lithium batteries,” *J. Nanosci. Nanotechnol.*, vol. 16, no. 9, pp. 9278–9283, 2016.
- [48] M. Al Sakka, H. Gualous, J. Van Mierlo, and H. Culcu, “Thermal modeling and heat management of supercapacitor modules for vehicle applications,” *J. Power Sources*, vol. 194, no. 2, pp. 581–587, 2009.
- [49] P. J. Turner and H. O. Pritchard, “Calorimetric study of an electrochemical reduction,” *Can. J. Chem.*, vol. 56, no. 10, pp. 1415–1418, 1978.
- [50] J. M. Sherfey and A. Brenner, “Electrochemical calorimetry,” *J. Electrochem. Soc.*, vol. 105, no. 11, pp. 665–672, 1958.
- [51] Z. Cheng, X. Ji, and D. G. Cahill, “Battery absorbs heat during charging uncovered by ultra-sensitive thermometry,” *J. Power Sources*, vol. 518, 2022, Art. no. 230762.
- [52] K. D. Etzel, K. R. Bickel, and R. Schuster, “A microcalorimeter for measuring heat effects of electrochemical reactions with submonolayer conversions,” *Rev. Sci. Instrum.*, vol. 81, no. 3, 2010, Art. no. 034101.
- [53] S. Frittmann, V. Halka, C. Jaramillo, and R. Schuster, “An improved sensor for electrochemical microcalorimetry, based on lithiumtantalate,” *Rev. Sci. Instrum.*, vol. 86, no. 6, 2015, Art. no. 064102.
- [54] B. Sakintuna and Y. Yurum, “Templated porous carbons: A review article,” *Ind. Eng. Chem. Res.*, vol. 44, no. 9, pp. 2893–2902, 2005.

-
- [55] A. J. Bard and L. R. Faulkner, *Electrochemical methods: Fundamentals and applications*. New York: John Wiley & Sons, 2001.
- [56] M. L. Huber, R. A. Perkins, D. G. Friend, J. V. Sengers, M. J. Assael, I. N. Metaxa, K. Miyagawa, R. Hellmann, and E. Vogel, “New international formulation for the thermal conductivity of H₂O,” *J. Phys. Chem. Ref. Data*, vol. 41, no. 3, 2012, Art. no. 033102.
- [57] J. C. Wadsworth, “The statistical description of precision conductivity data for aqueous sodium chloride,” *J. Solution Chem.*, vol. 41, pp. 715–729, 2012.
- [58] L. de Souza Vieira, “A review on the use of glassy carbon in advanced technological applications,” *Carbon*, vol. 186, pp. 282–302, 2022.
- [59] L. G. Rubin and Y. Golahny, “An improved ac bridge circuit for use in four-terminal resistance thermometry,” *Rev. Sci. Instrum.*, vol. 43, no. 12, 1972, Art. no. 1758.
- [60] Y. Wang, Y. Song, and Y. Xia, “Electrochemical capacitors: Mechanism, materials, systems, characterization and applications,” *Chem. Soc. Rev.*, vol. 45, no. 21, pp. 5925–5950, 2016.
- [61] M. E. Suss, S. Porada, X. Sun, P. M. Biesheuvel, J. Yoon, and V. Presser, “Water desalination *via* capacitive deionization: What is it and what can we expect from it?” *Energ. Environ. Sci.*, vol. 8, no. 8, pp. 2296–2319, 2015.
- [62] D. Brogioli, “Extracting renewable energy from a salinity difference using a capacitor,” *Phys. Rev. Lett.*, vol. 103, no. 5, 2009, Art. no. 058501.
- [63] M. L. Jiménez, M. M. Fernández, S. Ahualli, G. Iglesias, and A. V. Delgado, “Predictions of the maximum energy extracted from salinity exchange inside porous electrodes,” *J. Coll. Interf. Sci.*, vol. 402, pp. 340–349, 2013.
- [64] C. Largeot, C. Portet, J. Chmiola, P.-L. Taberna, Y. Gogotsi, and P. Simon, “Relation between the ion size and pore size for an electric double-layer capacitor,” *J. Am. Chem. Soc.*, vol. 130, no. 9, pp. 2730–2731, 2008.

- [65] R. Burt, G. Birkett, and X. S. Zhao, “A review of molecular modelling of electric double layer capacitors,” *Phys. Chem. Chem. Phys.*, vol. 16, no. 14, pp. 6519–6538, 2014.
- [66] T. Colla, M. Girotto, A. P. dos Santos, and Y. Levin, “Charge neutrality breakdown in confined aqueous electrolytes: Theory and simulation,” *J. Chem. Phys.*, vol. 145, no. 9, 2016, Art. no. 094704.
- [67] H. Tao, C. Lian, and H. Liu, “Multiscale modeling of electrolytes in porous electrode: From equilibrium structure to non-equilibrium transport,” *Green Energy Environ.*, vol. 5, no. 3, pp. 303–321, 2020.
- [68] G. Feng, R. Qiao, J. Huang, B. G. Sumpter, and V. Meunier, “Ion distribution in electrified micropores and its role in the anomalous enhancement of capacitance,” *ACS Nano*, vol. 4, no. 4, pp. 2382–2390, 2010.
- [69] G. Feng and P. T. Cummings, “Supercapacitor capacitance exhibits oscillatory behavior as a function of nanopore size,” *J. Phys. Chem. Lett.*, vol. 2, no. 22, pp. 2859–2864, 2011.
- [70] E. E. Fileti, “Electric double layer formation and storing energy processes on graphene-based supercapacitors from electrical and thermodynamic perspectives,” *J. Mol. Mod.*, vol. 26, no. 6, 2020, Art. no. 159.
- [71] Z. Wang, D. L. Olmsted, M. Asta, and B. B. Laird, “Electric potential calculation in molecular simulation of electric double layer capacitors,” *J. Condens. Matter Phys.*, vol. 28, no. 46, 2016, Art. no. 464006.
- [72] Y. Marcus, “A simple empirical model describing the thermodynamics of hydration of ions of widely varying charges, sizes, and shapes,” *Biophysic. Chem.*, vol. 51, no. 2-3, pp. 111–127, 1994.
- [73] M. D. Levi, S. Sigalov, G. Salitra, R. Elazari, and D. Aurbach, “Assessing the solvation numbers of electrolytic ions confined in carbon nanopores under dynamic charging conditions,” *J. Phys. Chem. Lett.*, vol. 2, no. 2, pp. 120–124, 2011.

-
- [74] J. T. G. Overbeek, “The role of energy and entropy in the electrical double layer,” *Colloids Surf.*, vol. 51, pp. 61–75, 1990.
- [75] L. Fumagalli, A. Esfandiar, R. Fabregas, S. Hu, P. Ares, A. Janardanan, Q. Yang, B. Radha, T. Taniguchi, K. Watanabe, G. Gomila, K. S. Novoselov, and A. K. Geim, “Anomalously low dielectric constant of confined water,” *Science*, vol. 360, no. 6395, pp. 1339–1342, 2018.
- [76] A. Härtel, M. Janssen, S. Samin, and R. Van Roij, “Fundamental measure theory for the electric double layer: Implications for blue-energy harvesting and water desalination,” *J. Phys. Condens. Matter*, vol. 27, no. 19, 2015, Art. no. 194129.
- [77] A. Härtel, S. Samin, and R. Van Roij, “Dense ionic fluids confined in planar capacitors: In- and out-of-plane structure from classical density functional theory,” *J. Phys. Condens. Matter*, vol. 28, no. 24, 2016, Art. no. 244007.
- [78] M. J. Kadhim and M. I. Gamaj, “Estimation of the diffusion coefficient and hydrodynamic radius (Stokes radius) for inorganic ions in solution depending on molar conductivity as electro-analytical technique-a review,” *J. Chem. Rev.*, vol. 2, no. 3, pp. 182–188, 2020.
- [79] P. C. F. Pau, J. O. Berg, and W. G. McMillan, “Application of Stokes’ law to ions in aqueous solution,” *J. Phys. Chem.*, vol. 94, no. 6, pp. 2671–2679, 1990.
- [80] Y. Marcus, “Are ionic Stokes radii of any use?” *J. Solution Chem.*, vol. 41, no. 11, pp. 2082–2090, 2012.
- [81] P. Harris, “Fullerene-like models for microporous carbon,” *J. Mater. Sci.*, vol. 48, pp. 565–577, 2013.
- [82] S. Kondrat and A. Kornyshev, “Superionic state in double-layer capacitors with nanoporous electrodes,” *J. Phys. Condens. Matter*, vol. 23, no. 2, 2011, Art. no. 022201.
- [83] S. Kondrat, N. Georgi, M. V. Fedorov, and A. A. Kornyshev, “A superionic state in nano-porous double-layer capacitors: insights from Monte

- Carlo simulations,” *Phys. Chem. Chem. Phys.*, vol. 13, pp. 11 359–11 366, 2011.
- [84] B. Skinner, M. S. Loth, and B. I. Shklovskii, “Capacitance of the double layer formed at the metal/ionic-conductor interface: How large can it be?” *Phys. Rev. Lett.*, vol. 104, p. 128302, 2010.
- [85] Z.-X. Luo, Y.-Z. Xing, Y.-C. Ling, A. Kleinhammes, and Y. Wu, “Electroneutrality breakdown and specific ion effects in nanoconfined aqueous electrolytes observed by NMR,” *Nat. Commun.*, vol. 6, 2015, Art. no. 6358.
- [86] S. Porada, H. V. M. Hamelers, and P. M. Biesheuvel, “Electrostatic cooling at electrolyte-electrolyte junctions,” *Phys. Rev. Res.*, vol. 1, no. 3, 2019, Art. no. 033195.
- [87] P. M. Biesheuvel, R. Zhao, S. Porada, and A. van der Wal, “Theory of membrane capacitive deionization including the effect of the electrode pore space,” *J. Coll. Interf. Sci.*, vol. 360, no. 1, pp. 239–248, 2011.
- [88] R. Zhao, M. Soestbergen, H. H. M. Rijnaarts, A. van der Wal, M. Z. Bazant, and P. M. Biesheuvel, “Time-dependent ion selectivity in capacitive charging of porous electrodes,” *J. Coll. Interf. Sci.*, vol. 384, no. 1, pp. 38–44, 2012.
- [89] R. Zhao, P. M. Biesheuvel, and A. van der Wal, “Energy consumption and constant current operation in membrane capacitive deionization,” *Energy Environ. Sci.*, vol. 5, no. 11, pp. 9520–9527, 2012.
- [90] R. Zhao, O. Satpradit, H. H. M. Rijnaarts, P. M. Biesheuvel, and A. Wal, “Optimization of salt adsorption rate in membrane capacitive deionization,” *Wat. Res.*, vol. 47, no. 5, pp. 1941–1952, 2013.
- [91] R. Zhao, S. Porada, P. M. Biesheuvel, and A. van der Wal, “Energy consumption in membrane capacitive deionization for different water recoveries and flow rates, and comparison with reverse osmosis,” *Desalination*, vol. 330, pp. 35–41, 2013.

-
- [92] M. H. Polley, W. D. Schaeffer, and W. R. Smith, "Physical adsorption studies in carbon black," *J. Can. Chem.*, vol. 33, no. 2, pp. 314–319, 1955.
- [93] R. S. Mikhail, S. Brunauer, and E. E. Bodor, "Investigations of a complete pore structure analysis: I. analysis of micropores," *J. Coll. Interf. Sci.*, vol. 26, no. 1, pp. 45–53, 1968.
- [94] E. P. Barrett, L. G. Joyner, and P. P. Halenda, "The determination of pore volume and area distributions in porous substances. I. Computations from nitrogen isotherms," *J. Am. Chem. Soc.*, vol. 73, no. 1, pp. 373–380, 1951.
- [95] J. Lyklema, *Fundamentals of Interface and Colloid Science: Fundamentals*, ser. Fundamentals of Interface & Co. London: Elsevier Science, 1991.
- [96] M. Guo, G. Sikha, and R. E. White, "Single-particle model for a lithium-ion cell: Thermal behavior," *J. Electrochem. Soc.*, vol. 158, pp. A122–A132, 2011.
- [97] L. Song, Z. Xiao, and Y. Zhou, "Thermo-electrochemical study on LiMn_2O_4 lithium-ion cells during charge–discharge process," *Electrochim. Acta*, vol. 114, pp. 611–616, 2013.
- [98] Q. Wang, B. Jiang, Q. F. Xue, H. L. Sun, B. Li, H. M. Zou, and Y. Y. Yan, "Experimental investigation on EV battery cooling and heating by heat pipes," *Appl. Therm. Eng.*, vol. 88, pp. 54–60, 2015.
- [99] Z. G. Qu, Z. Y. Jiang, and Q. Wang, "Experimental study on pulse self-heating of lithium-ion battery at low temperature," *Int. J. Heat Mass Transf.*, vol. 135, pp. 696–705, 2019.
- [100] L. H. J. Raijmakers, D. L. Danilov, R.-A. Eichel, and P. H. L. Notten, "A review on various temperature-indication methods for Li-ion batteries," *Appl. Energy*, vol. 240, pp. 918–945, 2019.
- [101] M. Chen, D. Ouyang, S. Cao, J. Liu, Z. Wang, and J. Wang, "Effects of heat treatment and SOC on fire behaviors of lithium-ion batteries pack," *J. Therm. Anal. Calorim.*, vol. 136, no. 2, p. 2429–2437, 11 2018.

- [102] J. Marcicki and X. G. Yang, “Model-based estimation of reversible heat generation in lithium-ion cells,” *J. Electrochem. Soc.*, vol. 161, no. 12, pp. A1794–A1800, 08 2014.
- [103] K. E. Thomas and J. Newman, “Heats of mixing and of entropy in porous insertion electrodes,” *J. Power Sources*, vol. 119-121, pp. 844–849, 2003.
- [104] R. J. Noll and J. M. Hughes, “Heat evolution and electrical work of batteries as a function of discharge rate: Spontaneous and reversible processes and maximum work,” *J. Chem. Educ.*, vol. 95, no. 5, pp. 852–857, 2018.
- [105] A. F. Gunnarshaug, P. J. S. Vie, and S. Kjelstrup, “Review—reversible heat effects in cells relevant for lithium-ion batteries,” *J. Electrochem. Soc.*, vol. 168, no. 5, p. 050522, 05 2021.
- [106] L. E. Helseth, “Modelling supercapacitors using a dynamic equivalent circuit with a distribution of relaxation times,” *J. Energy Storage*, vol. 25, 2019, Art. no. 100912.
- [107] V. Sedlakova, J. Sikula, J. Majzner, P. Sedlak, T. Kuparowitz, B. Buerger, and P. Vasina, “Supercapacitor equivalent electrical circuit model based on charges redistribution by diffusion,” *J. Power Sources*, vol. 286, pp. 58–65, 2015.
- [108] G.-J. Lee and S. I. Pyun, “Theoretical approach to ion penetration into pores with pore fractal characteristics during double-layer charging/discharging on a porous carbon electrode,” *Langmuir*, vol. 22, no. 25, pp. 10 659–10 665, 2006.
- [109] L. E. Helseth, “The self-discharging of supercapacitors interpreted in terms of a distribution of rate constants,” *J. Energy Storage*, vol. 34, 2021, Art. no. 102199.
- [110] P. M. Biesheuvel and M. Z. Bazant, “Nonlinear dynamics of capacitive charging and desalination by porous electrodes,” *Phys. Rev. E*, vol. 81, 2010, Art. no. 031502.

-
- [111] C. Costentin and J.-M. Savéant, “Electrochemical capacitive charging in porous materials. discriminating between ohmic potential drop and counterion diffusion,” *ACS Appl. Energy Mater.*, vol. 2, no. 7, pp. 4981–4986, 2019.
- [112] K. Breitsprecher, C. Holm, and S. Kondrat, “Charge me slowly, I am in a hurry: Optimizing charge–discharge cycles in nanoporous supercapacitors,” *ACS Nano*, vol. 12, no. 10, pp. 9733–9741, 2018.
- [113] M. Z. Bazant, K. Thornton, and A. Ajdari, “Diffuse-charge dynamics in electrochemical systems,” *Phys. Rev. E*, vol. 70, 2004, Art. no. 021506.
- [114] K. Ma, M. Janssen, C. Lian, and R. van Roij, “Dynamic density functional theory for the charging of electric double layer capacitors,” *J. Chem. Phys.*, vol. 156, no. 8, 2022, Art. no. 084101.
- [115] B. Balu and A. S. Khair, “Role of Stefan–Maxwell fluxes in the dynamics of concentrated electrolytes,” *Soft Matter*, vol. 14, no. 41, pp. 8267–8275, 2018.
- [116] R. de Levie, “On porous electrodes in electrolyte solutions: I. capacitance effects,” *Electrochim. Acta*, vol. 8, no. 10, pp. 751–780, 1963.
- [117] M. Mirzadeh, F. Gibou, and T. M. Squires, “Enhanced charging kinetics of porous electrodes: Surface conduction as a short-circuit mechanism,” *Phys. Rev. Lett.*, vol. 113, no. 9, 2014, Art. no. 097701.
- [118] S. Bi, H. Banda, M. Chen, N. Liang, M. Chen, T. Wu, J. Wang, R. Wang, J. Feng, T. Chen, M. Dincă, A. A. Kornyshev, and G. Feng, “Molecular understanding of charge storage and charging dynamics in supercapacitors with MOF electrodes and ionic liquid electrolytes,” *Nat. Mater.*, vol. 19, pp. 552–558, 2020.
- [119] R. Kohlrausch, “(theorie des elektrischen rückstandes in der leidener flasche.”
- [120] H. Sakaguchi and R. Baba, “Electric double layer on fractal electrodes,” *Phys. Rev. E*, vol. 75, no. 5, 2007, Art. no. 051502.

- [121] A. C. Forse, J. M. Griffin, C. Merlet, J. Carretero-Gonzalez, A.-R. O. Raji, N. M. Trease, and C. P. Grey, “Direct observation of ion dynamics in supercapacitor electrodes using *in-situ* diffusion NMR spectroscopy,” *Nat. Energy*, vol. 2, 2017, Art. no. 16216.
- [122] R. Tivony, S. Safran, P. Pincus, G. Silbert, and J. Klein, “Charging dynamics of an individual nanopore,” *Nat. Comm.*, vol. 9, no. 1, 2018, Art. no. 4203.
- [123] B. Dyatkin, O. Gogotsi, B. Malinovskiy, Y. Zozulya, P. Simon, and Y. Gogotsi, “High capacitance of coarse-grained carbide derived carbon electrodes,” *J. Power Sources*, vol. 306, pp. 32–41, 2016.
- [124] Y. He, R. Qiao, J. Vatamanu, O. Borodin, D. Bedrov, J. Huang, and B. G. Sumpter, “Importance of ion packing on the dynamics of ionic liquids during micropore charging,” *J. Phys. Chem. Lett.*, vol. 7, no. 1, pp. 36–42, 2016.
- [125] Z. Bo, C. Li, H. Yang, K. Ostrikov, J. Yan, and K. Cen, “Design of supercapacitor electrodes using molecular dynamics simulations,” *Nanomicro Lett.*, vol. 10, no. 2, 2018, Art. no. 33.
- [126] M. Rose, Y. Korenblit, E. Kockrick, L. Borchardt, M. Oschatz, S. Kaskel, and G. Yushin, “Hierarchical micro- and mesoporous carbide-derived carbon as a high-performance electrode material in supercapacitor,” *Small*, vol. 7, no. 8, pp. 1108–1117, 2011.
- [127] Y. Korenblit, M. Rose, E. Kockrick, L. Borchardt, A. Kvit, S. Kaskel, and G. Yushin, “High-rate electrochemical capacitors based on ordered mesoporous silicon carbide-derived carbon,” *ACS Nano*, vol. 4, no. 3, pp. 1337–1344, 2010.
- [128] E. Redondo, J. Carretero-González, E. Goikolea, J. Ségolini, and R. Mysyk, “Effect of pore texture on performance of activated carbon supercapacitor electrodes derived from olive pits,” *Electrochim. Acta*, vol. 160, pp. 178–184, 2015.

-
- [129] J. Chmiola, G. Yushin, R. Dash, and Y. Gogotsi, “Effect of pore size and surface area of carbide derived carbons on specific capacitance,” *J. Power Sources*, vol. 158, no. 1, pp. 765–772, 2006.
- [130] M. Pourbaix, *Atlas of Electrochemical Equilibria in Aqueous*. National Association of Corrosion Engineers, Houston, 1974.
- [131] A. R. Finney, I. J. McPherson, P. R. Unwin, and M. Salvalaglio, “Electrochemistry, ion adsorption and dynamics in the double layer: a study of NaCl(aq) on graphite,” *Chem. Sci.*, vol. 12, no. 33, pp. 11 166–11 180, 2021.
- [132] B. Ghanbarian, A. G. Hunt, R. P. Ewing, and M. Sahimi, “Tortuosity in porous media: A critical review,” *Soil. Sci. Soc. Am. J.*, vol. 77, pp. 1461–1477, 09 2013.
- [133] G. Jones and C. F. Bickford, “The conductance of aqueous solutions as a function of the concentration. I. Potassium bromide and lanthanum chloride,” *J. Am. Chem. Soc.*, vol. 56, no. 3, pp. 602–611, 1934.

List of Publications

The content of this thesis is based on the following publications:

Chapter 2:

Joren E. Vos, Hendrik P. Rodenburg, Danny Inder Maur, Ties J. W. Bakker, Henkjan Siekman, and Ben H. Ern , “Three-Electrode Cell Calorimeter for Electrical Double Layer Capacitors”, *Review of Scientific Instruments* vol. 93, 2022, Art. no. 124102.

Chapter 3:

Joren E. Vos, Danny Inder Maur, Hendrik P. Rodenburg, Lennart van den Hoven, Suzan E. Schoemaker, Petra E. de Jongh, and Ben H. Ern , “Electric Potential of Ions in Electrode Micropores Deduced from Calorimetry”, *Physical Review Letters*, vol. 129, 2022, Art. no. 186001.

Chapter 4:

Joren E. Vos and Ben H. Ern , “Capacitive Charging Rate Dependence of Heat from Porous Carbon in Aqueous Salt Solution”, *Electrochimica Acta*, vol. 443, 2023, Art. no. 141957.

Chapter 5:

Joren E. Vos and Ben H. Ern , “Cathodic versus Anodic Charging Dynamics of Capacitive Porous Carbon Electrodes in Aqueous Salt Solutions”, in preparation

Acknowledgments

It would not have been possible to do the work described in this thesis without the help and support of many people. I will not be able to thank everyone individually, so if you are not specifically mentioned: thank you for your support!

I want to thank my promotor and copromotor. Albert, thank you for giving me the opportunity to do a research project at the Van 't Hoff Laboratory of the Utrecht University and for useful discussions. Ben, thank you for your support and guidance, and for the input on my project, which was always very useful. You were always available to answer my questions.

During this project, I worked with several people on the publications. Thank you for your cooperation! Furthermore, I'd like to thank Maarten Biesheuvel for useful discussions and input. Also thank you to the user committee for reading my thesis.

While doing my PhD project, I supervised and guided some student projects. Henrik, Danny, Ties, Isabell, Lennart, Wouter, Rogier and Iwan, thank you for your work on this project! I hope you learned something during your project, just as much as I learned something from you!

The research I did would not be half as much fun without a good working environment. Therefore, I want to thank everyone at Physical and Colloid Chemistry (FCC). Dominique, Marina and Alex, thank you for allowing me to join your early morning coffee break. It was always fun to discuss some non-work related stuff with a cup of (actual!) coffee. Alessio, Frans and Geert, thank you for being my roommates (even though it might have been a very short time) and for the small talk. I will miss the avocado plant(s). Neshat, you started around the same time as me, so thank you for always being around and finding out the technical details of doing a PhD at the same time. I felt honored taking the picture for your booklet! All the other PhD candidates, technical staff and students thank you for making FCC such a nice working environment as well, also outside of working hours! Johan van der Zwan and Marc Baldus, thank you for allowing and helping me doing NMR spectroscopy on the in-situ concentration of ^1H , ^{19}F , and ^{23}Na ions inside the pores during

the (dis)charging of porous carbon. I hope the project will soon be picked up where I left it.

Graag wil ik ook mijn familie bedanken; in eerste instantie Monique en Armand. Bedankt voor alle ondersteuning die jullie mij gegeven hebben, zeker in de momenten dat ik twijfelde aan mezelf. Marthe, bedankt dat je altijd een luisterend oor wilde zijn. Jullie hebben mij altijd een fijne en veilige omgeving gegeven om op te groeien. Truus, bedankt voor onze interessante discussies over wat het inhoudt om wetenschappelijk onderzoek te doen.

Vervolgens wil ik graag mijn vrienden bedanken en in het bijzonder Joris, Arthur, Riande, Thomas, Bas, Maaïke en Veerle. Het is altijd gezellig om met jullie af te spreken en te bespreken hoe het gaat, zowel persoonlijk als zakelijk!

Leon, bedankt voor alle ondersteuning en voor het altijd klaar staan. Ik vind het erg prettig dat jij naast me wilt staan tijdens mijn verdediging. Max, jou ken ik al sinds mijn kleutertijd en we zijn al die tijd goede vrienden gebleven. Bedankt dat je mijn paranimf wilt zijn.

Laura, bedankt voor alle steun, vertrouwen en opbeurende woorden in de afgelopen tijd. Jij zorgt ervoor dat het leven leuk is, met jou wil ik oud worden. Ik houd van jou.

About the Author

Joren Ezra Vos was born on March 18, 1992 in Nijmegen, the Netherlands. He grew up in Arnhem, attending the Heijenoordschool from 1996 to 2004. From 2004 to 2010, the author attended the Stedelijk Gymnasium Arnhem, where he received a gymnasium degree.

From 2010 to 2015, the author studied Chemistry at the Utrecht University. He finished this study with a Bachelor Thesis on Energy transfer from Gd^{3+} to Yb^{3+} in co-doped NaYF_4 , supervised by Prof. Dr. A. Meijerink. During the school year 2013-2014, the author was a board member at the chemistry study association U.S.S. Proton, as secretary.

After receiving a bachelor's degree, the author obtained a master's degree in Nanomaterials: Chemistry and Physics at the Utrecht University in 2017. His master's thesis (Synthesis and TEM investigation of nanocrystals and nanocrystal superlattices) was under supervision of Prof. Dr. D. A. M. Vanmaekelbergh.

In 2018, the author started at the Van 't Hoff laboratory at the Utrecht University, under the supervision of dr. B. H. Ern  and prof. dr. A. P. Philipse, to do the PhD work presented in this thesis.

